Pacific Northwest
NATIONAL LABORATORY

PNNL- 30841

FY 2020 Report of the Atmosphere to Electrons Land-Based Mesoscale-to-Microscale Coupling Project

December 2020

SE Haupt
R Arthur
L Berg
M Churchfield
A DeCastro
S Dettling
C Draxl
DJ Gagne
P Hawbecker
P Jimenez
A Jonko
T Juliano
C Kaul
B Kosović
W Lassman
M Kumar
TC McCandless
J Mirocha
E Quon
R Rai
W Shaw
R Thedin

U.S. DEPARTMENT OF ENERGY

Prepared for the U.S. Department of Energy
under Contract DE-AC05-76RL01830

PACIFIC NORTHWEST NATIONAL LABORATORY
operated by
BATTELLE
for the
UNITED STATES DEPARTMENT OF ENERGY
under Contract DE-AC05-76RL01830

Printed in the United States of America

Available to DOE and DOE contractors from the
Office of Scientific and Technical Information,
P.O. Box 62, Oak Ridge, TN 37831-0062;
ph: (865) 576-8401
fax: (865) 576-5728
email: reports@adonis.osti.gov

Available to the public from the National Technical Information Service
5301 Shawnee Rd., Alexandria, VA 22312
ph: (800) 553-NTIS (6847)
email: orders@ntis.gov <https://www.ntis.gov/about>
Online ordering: http://www.ntis.gov

PNNL- 30841

FY 2020 Report of the Atmosphere to Electrons Land-Based Mesoscale-to-Microscale Coupling Project

December 2020

SE Haupt[1]

R Arthur[2]	L Berg[3]	M Churchfield[4]
A DeCastro[1]	S Dettling[1]	C Draxl[4]
DJ Gagne[1]	P Hawbecker[1]	P Jimenez[1]
A Jonko[5]	T Juliano[1]	C Kaul[3]
B Kosović[1]	W Lassman[2]	TC McCandless[1]
M Kumar[5]	J Mirocha[2]	E Quon[4]
R Rai[3]	W Shaw[3]	R Thedin[4]

Prepared for
the U.S. Department of Energy
under Contract DE-AC05-76RL01830

Pacific Northwest National Laboratory
Richland, Washington 99354

---

[1] National Center for Atmospheric Research (NCAR)
[2] Lawrence Livermore National Laboratory (LLNL)
[3] Pacific Northwest National Laboratory (PNNL)
[4] National Renewable Energy Laboratory (NREL)
[5] Los Alamos National Laboratory (LANL)

Executive Summary

The overall goal of the Mesoscale-to-Microscale Coupling (MMC) project is to improve coupling between mesoscale and microscale simulations via improved guidance and new strategies for setting up simulations and for the development of new tools that can be used across the community. Including the mesoscale forcing is critical to modeling the full energy transfer across scales in the atmosphere. The project-specific objectives include the following:

- Apply rigorous verification and validation (V&V) techniques to the new modeling tools that are developed as part of the project to ensure the accuracy of our codes and results and to develop estimates of the relative uncertainty.
- Improve computational performance of the coupled MMC models through the development of methods that can be used to reduce turbulence spin-up time and, hence, the size of computational domains.
- Improve representation of the surface layer in microscale models to enhance simulations of hub-height wind speed.
- Develop guidance for the community describing the best ways to couple mesoscale and microscale models, including specific spatial scales at which the handoff to the microscale model should occur.
- Prepare documentation and a suite of software tools that can be used across the community.
- Transition MMC research to the offshore environment.

Major progress was made in each of these areas during fiscal year (FY) 2020. The land-based portion of the project is reported herein, while the offshore portion will be reported separately. The team continued to advance the MMC tools and methodologies, as well as to document their performance in journal papers and conference presentations, although several planned conferences were canceled due to the COVID-19 pandemic.

The team continued the approach of selecting case studies from field programs or observational data to identify challenging atmospheric conditions and test methods to simulate them, allowing for a V&V approach that is grounded in data. Uncertainty quantification emphasized determining parametric uncertainty in microscale simulations—large-eddy simulations (LES) within the Weather Research and Forecasting (WRF) model—through examining sensitivities within 128 members of an ensemble of perturbed simulations. Both a direct method and using feature and permutation importance maps within a random forest framework indicate that the eddy viscosity coefficient displays the largest sensitivity.

Continued study of microscale turbulence initiation slowed in FY 2020 as research was redirected to an offshore case. Work completed this year involved improving the common code bases used to simulate and assess the flows, which are now available on the public MMC GitHub, as well as to execute and analyze simulations of several perturbation techniques during a case study representing canonical convective conditions.

Models and parameterizations were advanced during FY 2020. The three-dimensional (3D) planetary boundary-layer (PBL) scheme was extended to a 2.5-level model and tested in the *terra incognita*, or gray zone, for complex terrain. The 3D PBL scheme appears to alleviate spurious convectively induced secondary circulations visible in simulations that use traditional

one-dimensional PBL parameterization. Another parameterization advancement is a machine learning model of the surface layer that was trained on datasets from Cabauw, the Netherlands, and from Idaho. Both random forest and artificial neural network models agreed better with observed data than did the traditional Monin-Obukhov similarity theory (MOST). In fact, in nearly all cases, the model trained on one site performed better at the other site than did MOST, suggesting transferability. Initial trials of this parameterization in WRF are promising.

A method was constructed to characterize turbulence scales from scanning lidar data collected during the Wind Forecast Improvement Project 2 experiment in the Columbia Gorge. This method allows post-processing with both spectral and principal orthogonal decomposition techniques. The turbulence shapes become more streaky and slender for negative heat flux conditions compared to cases with positive heat flux. These variations of flow structures can significantly impact the energy distribution throughout the boundary layer.

During FY 2019, the team discovered gravity waves reflected from boundaries in the microscale domains of offline-coupled models. Although the gravity waves are physical phenomena, their reflection is not. Damping methods were explored to alleviate this problem. Study of an idealized hill case indicates that Rayleigh damping methods can be effective, but one must carefully tune the size, strength, and placement of the damping layer.

Team members also modeled a diurnal case from the Wake Dynamics project field campaign at Peetz Table Wind Energy Center. By assimilating temperature and wind data, the changes in temperature were effectively simulated at the site, including producing realistic turbulence intensity. This demonstrated the effectiveness of MMC methods for a complex case, which included large-scale temperature advection.

To ensure that the MMC efforts remain relevant to the wind industry, the team formed an industry advisory panel, with active members representing wind plant developers, turbine manufacturers, and wind power forecasters. This panel helped to plan an industry workshop, Atmospheric Challenges for the Wind Energy Industry, which was held on October 19 and 20, 2020, and is more fully described in a separate report.

Finally, during FY 2020, the team began the pivot toward studying MMC processes for the offshore environment. An initial challenge case off northern Europe was begun, which we expect to complete during FY 2021 under the Offshore Wind Atmospheric Coupling project, which has branched off from this MMC project.

The MMC team continues to work collaboratively and has determined strategies to work through the remaining issues required to optimally provide coupled model simulations. These simulations and advances in technologies will provide the wind industry with new tools that can be used in the planning, design, layout, and optimization of wind plants, thus facilitating greater wind power penetration.

Acronyms and Abbreviations

1D	one-dimensional
2D	two-dimensional
3D	three-dimensional
A2e	Atmosphere to Electrons
ABL	atmospheric boundary layer
AGL	above ground level
ANN	artificial neural network
CPM	cell perturbation method
DAP	Data Archive and Portal
DOE	Department of Energy
FI	feature importance
FINO	Forschungsplattformen in Nord- und Ostsee (translation: Research platforms in the North and Baltic Seas)
FY	fiscal year
GHI	global horizontal irradiance
h	hours
K	kelvin
km	kilometers
LANL	Los Alamos National Laboratory
LES	large-eddy simulation
LLNL	Lawrence Livermore National Laboratory
m	meter
MAE	mean absolute error
ML	machine learning
MMC	Mesoscale-to-Microscale Coupling
MOST	Monin-Obukhov similarity theory
MSE	mean square error
NCAR	National Center for Atmospheric Research
NOAA	National Oceanic and Atmospheric Administration
NREL	National Renewable Energy Laboratory
PBL	planetary boundary-layer
PI	permutation importance
PNNL	Pacific Northwest National Laboratory
POD	proper orthogonal decomposition
PPE	perturbed parameter ensemble
PPI	plan position indicator

R^2	square of the Pearson correlation coefficient
RF	random forest
SGS	subgrid-scale
SOWFA	Simulator fOr Wind Farm Applications
SWiFT	Scaled Wind Farm Technology
TKE	turbulence kinetic energy
V&V	verification and validation
U.S.	United States
WFIP 2	Wind Forecast Improvement Project 2
WRF	Weather Research and Forecasting

Contents

Figures

Tables

1.0 Introduction

1.1 Purpose of the Mesoscale-to-Microscale Coupling Project

The overall goal of the Mesoscale-to-Microscale Coupling (MMC) project is to improve coupling between mesoscale and microscale simulations via improved guidance and new strategies for setting up simulations, as well as the development of new tools that can be used across the community. Accomplishing this goal will enable substantive improvements in wind plant design, operation, and performance projections. While significant progress was made during Phase 1, there remain a number of open science questions that are being addressed during Phase 2. This second phase will culminate in producing well-validated tools with the uncertainty quantified, as well as validation cases that will be useful to industry. The project-specific objectives include:

- Apply rigorous verification and validation (V&V) techniques to the new modeling tools that are developed as part of the project to ensure the accuracy of our codes and results and to develop estimates of the relative uncertainty.
- Improve computational performance of the coupled MMC models through the development of methods that can be used to reduce turbulence spin-up time and, hence, the size of computational domains.
- Improve representation of the surface layer in microscale models to enhance simulations of hub-height wind speed.
- Develop guidance for the community describing the best ways to couple mesoscale and microscale models, including specific spatial scales at which the handoff to the microscale model should occur.
- Prepare documentation and a suite of software tools that can be used across the community.
- Transition MMC research to the offshore environment.

This second phase of the MMC project has been designed to address these six objectives.

Realizing these objectives will enable simulation of the full suite of mesoscale and microscale flow characteristics affecting turbine and wind plant performance and uncertainties, thereby allowing for substantive improvements in wind plant design, operation, and performance projections. Figure 1.1 diagrams the MMC approach to the project and demonstrates the integration among the objectives. The work is grounded in data from field sites and experiments and culminates in guidelines for best-practice modeling, software tools, datasets for testing, and full documentation.

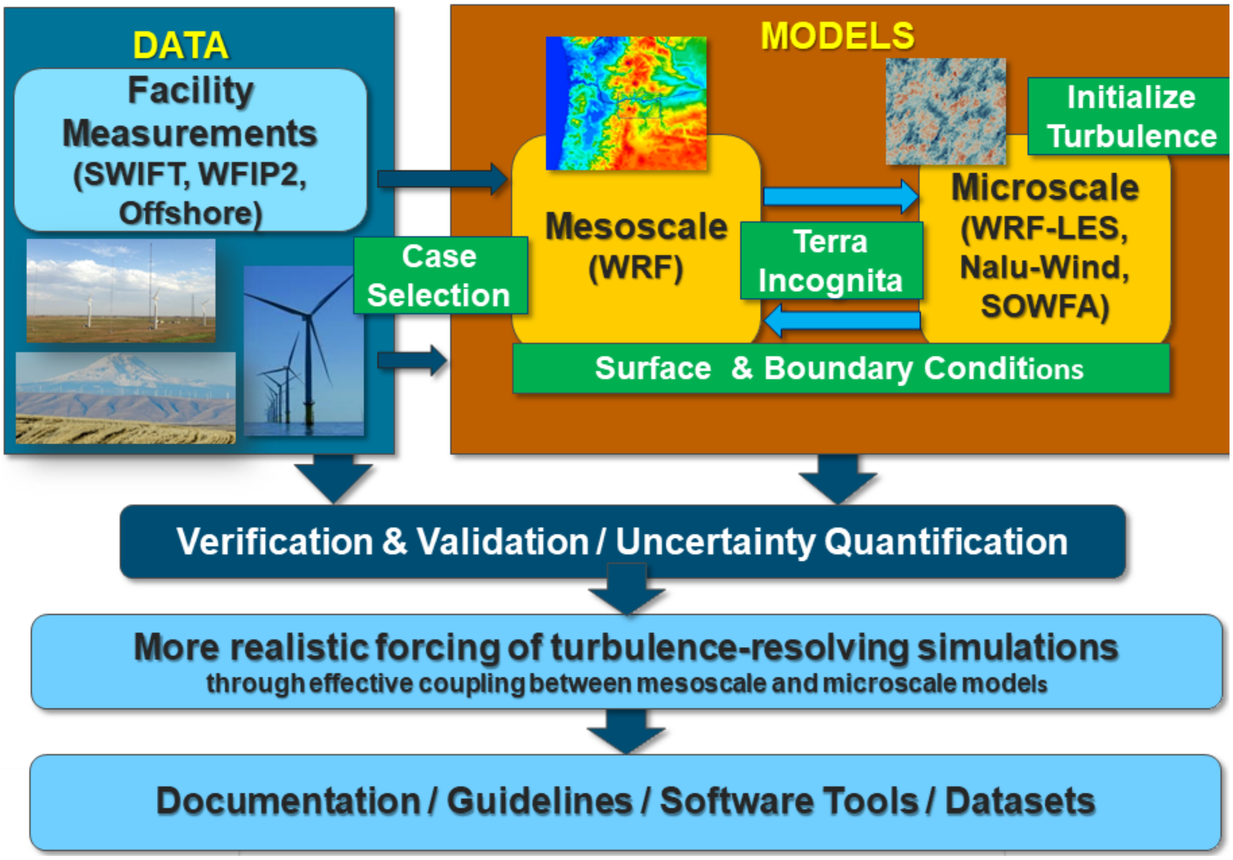

Figure 1.1. Diagram of the MMC project approach of using case studies to address the challenges of mesoscale-to-microscale wind plant simulation challenges.

In addition, to facilitate the transition to the offshore environment, in FY 2021, the project is transitioning to two separate but related research projects: 1) a continuation and closeout of the land-based MMC research, and 2) the Offshore Wind Atmospheric Coupling project. This report details the FY 2020 efforts for the land-based portion of the research. A separate report will be prepared to report on an offshore case using data from the FINO (Forschungsplattformen in Nord- und Ostsee [translation: Research Platforms in the North and Baltic Seas]) towers off the European coast that began in FY 2020 and is expected to be completed during FY 2021. An additional report being prepared in parallel with this one details the MMC team-led Atmospheric Challenges for the Wind Energy Industry Workshop that was held in October 2020.

1.2 Motivation for Coupled Modeling

Coupling mesoscale (horizontal grid spacing on the order of kilometers) and microscale (horizontal grid spacing on the order of meters to tens of meters) models is an important step forward for the wind power industry. Appropriate techniques and tools are needed to better understand the turbulent wind flow into and within the wind plant, which impacts energy transfer between scales—and ultimately the amount of energy available to harvest. The ability to couple these scales is particularly important for nonstationary meteorological conditions (such as frontal passages, thunderstorm outflows, and low-level jets) or when considering changes in atmospheric stability associated with the diurnal cycle. Improved estimates of the driving flow are needed to optimize wind plant and turbine siting, design, and operation. During the first phase of the Atmosphere to Electrons (A2e) MMC project, important progress was made by our team in a number of key areas that are highlighted later in this section.

Even with these advances, however, some significant challenges remain, which include 1) providing appropriate and consistent boundary and initial conditions; 2) bridging the so-called *terra incognita* (Wyngaard 2004), the range of spatial scales between about 100 meters (m) and the depth of the boundary layer that is problematic for boundary-layer parameterizations applied in mesoscale models; 3) initializing turbulence at the correct spatial and temporal scales in the microscale models; 4) testing appropriate coupling methodologies; 5) quantifying the uncertainty of the methods; and 6) exploring the applicability of the techniques for the offshore environment. The MMC team's integrated approach to addressing these challenges has been, and will continue to be, grounded in data. The team seeks to leverage United States (U.S.) Department of Energy (DOE)-supported field studies—including at the Scaled Wind Farm Technology (SWiFT) facility site in Texas and the Wind Forecast Improvement Project 2 (WFIP 2) (Shaw et al. 2019) in the complex terrain of the Pacific Northwest—to select case studies that facilitate addressing the challenges. Through these case studies, the different approaches can be systematically tested and assessed using metrics specific to wind plant operations. Figure 1.2 illustrates key elements of the project approach.

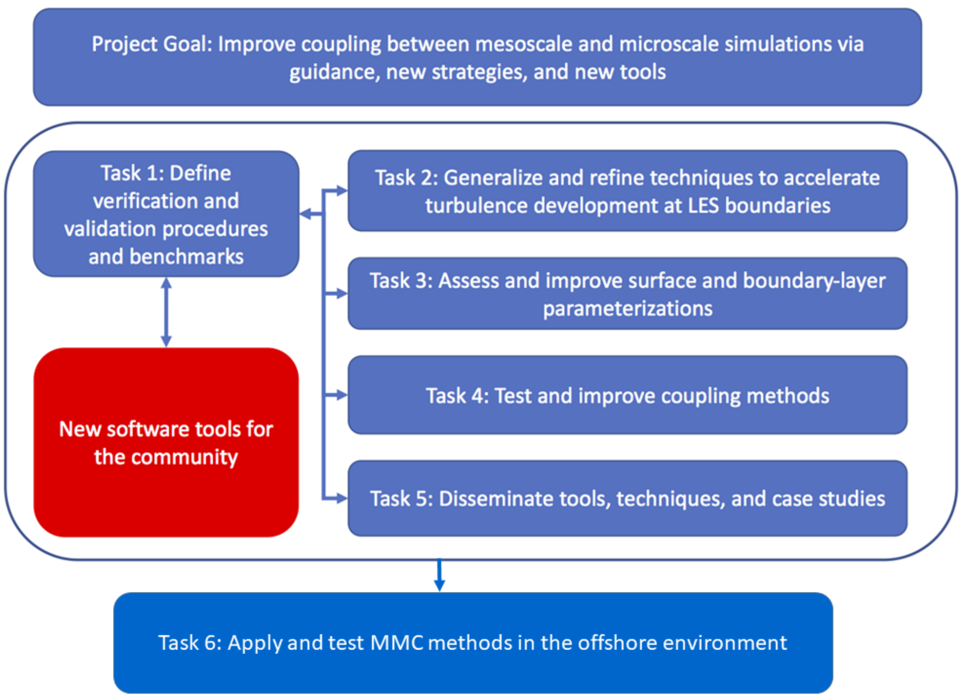

Figure 1.2. Depiction of overarching project goal, tasks, and planned outcome.

1.3 MMC Project Context within DOE Research

DOE stood up a major A2e initiative within the DOE Office of Energy Efficiency and Renewable Energy Wind Energy Technologies Office, whose goal is to optimize power production from wind plants. To that end, the initiative explicitly integrates advances in atmospheric sciences, wind plant aerodynamics, and wind plant control technologies, taking advantage of current and emerging capabilities for high-performance computing. Because atmospheric inflow is the fuel that powers wind plants, containing both the energy available for conversion into electricity, as well as characteristics that modulate that conversion, the development and validation of first-principles-based, high-fidelity physics models in an open-source simulation environment has been identified as a crucial part of DOE A2e science goals and objectives. Furthermore, there has been an overwhelming consensus in the research community that these models must be developed and systematically validated using a formal V&V process that includes uncertainty quantification. The MMC project includes an initial demonstration of the V&V-guided approach to model development specifically applied to the mesoscale-microscale coupling problem. This is a joint collaborative project among DOE national laboratories, with the National Center for Atmospheric Research (NCAR) leadership as a subcontractor, and it incorporates external feedback from members of other DOE research teams, a merit review panel, industry, DOE leadership, and other stakeholders. The A2e program and the MMC project are now working toward completion. During FY 2020, the MMC project began to explore applying the project's techniques in the offshore environment.

The MMC project is grounded in data provided by other DOE facilities and projects. For the first two years, the data emphasized measurements taken at the DOE/Sandia National Laboratories SWiFT facility in West Texas. The MMC modeling helped characterize and inform the wake dynamics experiments being accomplished at that site, and its results are expected to contribute to modeling wake dynamics. In years three and four, the MMC project focused on coupled modeling in complex terrain, using data derived from observations taken in the Pacific Northwest as part of WFIP 2.

Including mesoscale forcing in microscale models is critical to the success of the A2e project that focuses on wind plant controls. Most prominently, the very specific coupling and modeling philosophies and technologies being developed by the MMC project are necessary for building the high-fidelity modeling tools that are needed by researchers and industry. The results of the MMC modeling and case studies are being archived in DOE's Data Archive and Portal (DAP), and code is being provided via a GitHub repository. Each of the models and techniques we used are validated against a range of metrics to determine their accuracy for a mix of wind-energy-related applications. *A key outcome of this project is concrete guidance to both industry and research communities regarding the potential strengths and weaknesses of various MMC approaches*. Additionally, the best performing of the approaches assessed will be incorporated into the High-Fidelity Modeling project's Exawind environment for future design and testing, as well as the mesoscale-focused Energy Research and Forecasting model being developed.

1.4 Progression of the MMC Project

During the first phase of the MMC project, our team made a number of significant accomplishments:

- Down-selected the mesoscale model to be the Weather Research and Forecasting (WRF) model and initiated plans to transition changes to the A2e Energy Research and Forecasting model (via a separately funded project).
- Compared various microscale models and found that they performed similarly.
- Established metrics for V&V of these models relevant to wind plant simulations and the coupling mechanism, including evaluating turbulence.
- Developed, tested, and evaluated various methods to couple mesoscale-to-microscale simulations, determining that online coupling is needed within WRF to the large-eddy simulation (LES) scales and that applying tendency mesoscale forcing in the National

Renewable Energy Laboratory's Simulator fOr Wind Farm Applications (SOWFA) allows the LES model to follow the nonstationary behavior of WRF for diurnal cycle cases in flat terrain.

- Developed, tested, and evaluated various methods of initializing turbulence in the microscale models that is subgrid to the mesoscale models, finding that perturbations that are a combination of temperature and momentum induce turbulence at the correct scales.
- Developed, tested, and evaluated methods to deal with spurious rolls resulting from models with grid spacing in the *terra incognita*. Showed that the upper end of the *terra incognita* is roughly equal to the convective boundary-layer depth. Found that in most cases it is possible to configure WRF to skip grid spacings in the *terra incognita*.
- Demonstrated and evaluated running coupled simulations for complex terrain associated with WFIP 2.
- Explored methods to better represent the surface layer in both mesoscale and microscale simulations.
- Advanced a fully three-dimensional (3D) planetary boundary-layer (PBL) scheme that allows horizontal heterogeneity.

Over the life of the project, these results have been presented to the community through a series of articles in the peer-reviewed literature (Rai et al. 2016, 2017, 2019; Mirocha et al. 2018; Haupt et al. 2019b; Rodrigo et al. 2016; Muñoz-Esparza and Kosović 2018; Muñoz-Esparza et al. 2017, 2018; Quon et al. 2018; Mazzaro et al. 2017, 2019; Allaerts et al. 2020; Draxl et al. 2020); through presentations at conferences, including those of the American Meteorological Society, WindTech, Torque, Wind Energy Science, and International Conference on Energy and Meteorology; in Pacific Northwest National Laboratory technical reports (Haupt et al. 2015, 2017, 2019c,d); and in a series of industry webinars.

During FY 2020, MMC team members have also been actively engaged in organizing and presenting papers at major wind industry conferences that were used as forums for bringing the research community together with industry during FY 2020. This was successfully accomplished at the North American Wind Energy Academy/WindTech in Amherst, Massachusetts, in October 2019, and at the Eleventh Conference on Weather, Climate, and the New Energy Economy held as part of the American Meteorological Society Annual Meeting in Boston, Massachusetts, in January 2020. These meetings included presentations about the MMC project and afforded ample opportunity for industry representatives and team members to discuss the team's progress and plans. Due to the COVID-19 pandemic, in-person participation at several other conferences was canceled or delayed until travel is again allowed, although research continued, and presentations were delivered in a virtual environment.

1.5 Expected Impacts on Industry

The expected impact of the MMC project is to advance the science and engineering of coupled mesoscale-microscale modeling in order to provide industry with more advanced wind plant optimization capabilities. Industry stakeholders have made it clear what must be done in terms of better modeling of power output. This issue is complex and involves many factors beyond applying a simple power curve to a simulated mean wind speed and making small adjustments for turbulence. Uncertainties come from many different aspects of the coupling, including interannual variability due to longer-term climatic variability, variability in the outer scales that are resolved by the mesoscale models, variability due to wake effects, inner variability due to the heterogeneity within the wind plant, variability due to coherent structures, inherent uncertainty due to the chaotic nature of turbulent flow, and finally, impacts through the surface-layer treatment and its interactions with characteristics of the underlying surface. The MMC project addresses these issues directly and will culminate in specific guidance to industry.

Both the improved computational methodologies and the knowledge gained through their assessment and validation will enable substantive improvements in wind plant design, operation, and performance projections, all of which are required to attract continued investment in wind power as a viable means of meeting national goals of mitigating climate change and establishing energy independence.

The successful outcome of the MMC project will result in improved computer simulation capability that accurately incorporates the impact of mesoscale weather on wind power plant performance. Meeting this goal will require microscale simulations driven by realistic mesoscale forcing, knowledge of when the additional complexity of mesoscale coupling is beneficial, and recommendations for best practices for modeling across spatial and temporal scales. Over the course of this project, the tools and knowledge developed during each phase, outlined above, will continue to be made available to industry and the broader research community.

The MMC team has engaged with industry by holding a first-year workshop in September 2015 at NCAR, at which industry representatives were invited to comment on the approach and the results, as well as to suggest changes. In FY 2016, the MMC team conducted an industry survey. During FY 2017, the team conducted a first webinar with industry to inform them of our progress and solicit input. During FY 2019, three more webinars with industry (September 20, 2018, and February 14 and April 18, 2019) demonstrated industry's interest in the team's research results. The team also formed an industry advisory panel, which currently consists of:

- Mark Ahlstrom, NextEra Energy, Inc., Energy Systems Integration Group president
- Greg Oxley, Siemens/Gamesa
- Philippe Beaucage, UL/AWS Truepower.

During FY 2020, the advisory committee and the project team worked to plan an industry workshop to share results with the community and as an opportunity to receive feedback. The workshop was originally planned to be a face-to-face meeting in June 2020, but COVID-19 travel restrictions forced us to move to an online format for the workshop, which was conducted early in FY 2021. That workshop was quite successful and is reported on separately.

1.6 Report Contents and Organization

The remainder of this report documents the results of the MMC project's FY 2020 land-based effort. Section 2 describes advances made in 3D PBL that began under the WFIP 2 and continues under the MMC framework. A simulator to compare LES with lidar measurements is described in Section 3. Section 4 discusses a machine learning (ML) approach to modeling the surface layer. Section 5 compares turbulence generation methods at the microscale for neutral conditions. The microscale modeling team discovered challenges with spurious gravity waves in their simulations during FY 2019 that have now been studied, and recommendations were made to alleviate this issue, as described in Section 6. The team has also emphasized that the coupled atmospheric modeling directly impacts the power produced at wind plants. Section 7 provides an example case study at Peetz Table in Colorado. A key issue addressed in the MMC modeling efforts is quantifying the uncertainty in our techniques. To that end, Section 8 discusses applying ensemble methods to provide such uncertainty quantification. The final chapter, Section 9, synthesizes the results of the team's land-based research and its expected impact. Appendix A lists the team's ongoing contributions to the peer-reviewed literature and the conference papers which they have presented. Appendix B details each laboratory's contributions to the FY 2020 efforts.

2.0 Advancing the Three-Dimensional Planetary Boundary-layer Parameterization

2.1 Introduction and Motivation

Representing PBL processes in numerical weather prediction models remains an outstanding challenge. In mesoscale models, subgrid-scale (SGS) PBL turbulence must be parameterized; however, a problem arises when the turbulence has an integral length scale (l) similar to that of the grid cell spacing (Δx) of the model. In these scenarios, the most energetic turbulent eddies are neither fully parameterized nor fully resolved, and thus, the model is performing in a regime known as the "gray zone," or *terra incognita* (Wyngaard 2004).

As computing advancements allow for an increase in model resolution, more numerical weather prediction models are being run with resolutions in the gray zone; however, current PBL parameterizations are typically one-dimensional (1D); that is, they handle only the vertical mixing, and they leave the horizontal diffusion to be treated by a Smagorinsky-type approach (Smagorinsky 1963). While this approach is convenient and appropriate for relatively large grid cell spacings ($\Delta x >> z_i$, where z_i is the PBL depth), it is not valid when Δx lies in the gray zone, because the relative contribution of horizontal gradients in turbulent quantities becomes important; therefore, a more unified method that considers 3D turbulence is required in order to improve simulations of the PBL wind field. To address this issue—which becomes even more apparent in regions of complex terrain and heterogeneous land surfaces—we developed a new 3D PBL scheme for the WRF model (Skamarock et al. 2019).

During FY 2020, we published a manuscript detailing the new parameterization and its use in the context of wind energy forecasting (Kosović et al. 2019). Moreover, the research group currently has two manuscripts in preparation that examine the surface boundary condition developments (Eghdami et al., in press) and the application of the new scheme to various heterogeneous PBL regimes simulated at gray zone resolutions (Juliano et al., in press). In the remainder of this report, we provide details of the PBL parameterization development and recent results from simulations conducted with the WRF model in FY 2020.

2.2 Development of the New Parameterization

The new 3D PBL scheme, which is based on the algebraic model developed by Mellor (1973) and Mellor and Yamada (1974, 1982), accounts for the 3D effects of turbulence by calculating explicitly the momentum, heat, and moisture flux divergence, in addition to the turbulence kinetic energy (TKE). The parameterization involves solving a system of 13 linear algebraic equations at each model grid cell to extract the turbulent stresses and scalar fluxes. Once all six components of the turbulent stresses and three components of turbulent scalar fluxes are calculated, the 3D divergences of the stresses and fluxes are computed and added to the right-hand side of the prognostic equations for momentum, potential temperature, and specific humidity.

Using the model of Mellor (1973), higher moment velocity and temperature terms can be written. After determining these higher moment terms, closure assumptions (i.e., scaling and eliminating higher order terms) of various levels of complexity may be applied to the mean and turbulent momentum equations, eventually leading to the level 2.5 model (Mellor and Yamada 1982). To arrive at the level 2.5 model, material derivative and diffusion terms are neglected in the prognostic equation for potential temperature variance in the level 3 model. This assumption leads to diagnostic equations for potential temperature variance and any other scalar quantities (e.g., water vapor and hydrometeor mixing ratios) that may be included in the model. The level 2.5 model is the most commonly used closure assumption for TKE-based schemes due to its reasonable trade-off between accuracy and complexity. Moreover, prognostic TKE allows for a relatively smooth evolution of the turbulence field compared to the level 2 model (diagnostic TKE). For these reasons, we chose to base our 3D PBL parameterization developments on the level 2.5 model, as described in Mellor and Yamada (1982).

2.3 Three-Dimensional Level 2.5 Model

As of the FY 2019 report, we had implemented the level 2.5 model with the PBL approximation, which neglects horizontal gradients and is, therefore, not appropriate for gray zone simulations nor consistent with our implementation of a full 3D turbulence closure. During FY 2020, under the MMC project, we implemented the full 3D prognostic equation for TKE in the level 2.5 model:

$$\underset{[A]}{\frac{\partial q^2}{\partial t}} + \underset{[B]}{U_j \frac{\partial q^2}{\partial x_j}} - \underset{[C]}{\frac{\partial}{\partial x_j}\left[\ell q S_q \frac{\partial q^2}{\partial x_j}\right]} = 2(\underset{[D]}{P_s} + \underset{[E]}{P_b} - \underset{[F]}{\varepsilon}) \tag{1}$$

with:

$$P_s = -\overline{u_i u_j}\frac{\partial U_i}{\partial x_j}, P_b = -\beta g_i \overline{u_i \theta}, \varepsilon = \frac{q^3}{\Lambda_1} \tag{2}$$

where β is the coefficient of thermal expansion, Λ_1 is a length scale, and q^2 is twice TKE. Term [A] is the local tendency of TKE, [B] is the advection of TKE by the mean wind, [C] is the turbulent transport, [D] is the shear production of TKE, [E] is the buoyancy production of TKE, and [F] is the dissipation of TKE.

The remaining equations that define the level 2.5 model with moisture are:

$$\begin{aligned} \langle u_i u_j \rangle = {} & \frac{\delta_{ij}}{3} q^2 - 3\frac{l_1}{q}\left[\left(\langle u_k u_i \rangle - C_1 q^2 \delta_{ki}\right)\frac{\partial U_j}{\partial x_k} + \left(\langle u_k u_j \rangle - C_1 q^2 \delta_{kj}\right)\frac{\partial U_i}{\partial x_k} - \frac{2}{3}\delta_{ij}\langle u_k u_l \rangle \frac{\partial U_l}{\partial x_k}\right] \\ & - 3\frac{l_1}{q}\beta\left[g_j \langle u_i \theta_v \rangle + g_i \langle u_j \theta_v \rangle - \frac{2}{3}\delta_{ij} g_l \langle u_l \theta_v \rangle\right] \end{aligned} \tag{3}$$

$$\langle u_j \theta_v \rangle = -3\frac{l_2}{q}\left[\langle u_j u_k \rangle \frac{\Theta_v}{x_k} + \langle u_k \theta_v \rangle \frac{U_j}{x_k} + \beta g_j \langle \theta_v^2 \rangle\right] \tag{4}$$

$$\langle \theta_v^2 \rangle = -\frac{\Lambda_2}{q}\langle u_k \theta_v \rangle \frac{\Theta_v}{x_k} \tag{5}$$

where ℓ_1, ℓ_2, and Λ_2 are length scales. These three length scales, in addition to Λ_1, are proportional to each other and can be expressed in terms of a master length scale ℓ:

$$(\ell_1, \Lambda_1, \ell_2, \Lambda_2) = (A_1, B_1, A_2, B_2)\ell \tag{6}$$

The master length scale in the Mellor-Yamada model is adopted from Blackadar (1962) and defined as:

$$\ell = \frac{kz}{1 + kz/l_o} \tag{7}$$

with l_o given as:

$$l_o = \alpha \frac{\int_0^h qz\,dz}{\int_0^h q\,dz} \tag{8}$$

where α is an empirical constant set to 0.010. The original values for constants A_1, B_1, A_2, B_2, and C_1 are provided by Mellor and Yamada (1982):

$$(A_1,\ B_1,\ A_2,\ B_2,\ C_1) = (0.92, 16.6, 0.74, 10.1, 0.08). \tag{9}$$

These values are derived from experiments for neutral stability conditions, which occur relatively infrequently in the real-world land-based PBL. Moreover, we find that using this original set of parameters results in a diabatic profile of potential temperature, and in some instances, numerical stability is not maintained; therefore, we use high-resolution LES of a convective boundary layer over homogeneous terrain to arrive at the following values for these model parameters:

$$(A_1,\ B_1,\ A_2,\ B_2,\ C_1) = (0.3, 8.4, 0.33, 6.4, 0.08) \tag{10}$$

which are used in all the simulations presented herein.

2.4 Solving the System of Linear Equations

Once q^2, ℓ, and the 3D derivatives of the mean quantities are calculated, the second-order moments are computed by inverting a system of linear algebraic equations at each grid cell. We use the subroutine *dgesvx* from the Linear Algebra PACKage (Anderson et al. 1999) to compute the solution to the set of linear equations. For a dry WRF simulation that includes only heat as the scalar variable, the full system is defined by 10 simultaneous algebraic equations. Here, we present this system of 10 equations for six turbulent stresses, three turbulent sensible heat fluxes, and the potential temperature variance. Three additional equations, similar in nature to the equations for heat flux, are solved for the turbulent fluxes of each additional scalar variable of interest (water vapor mixing ratio, liquid water mixing ratio, etc.; not shown here). After all six components of turbulent stress and three components of turbulent scalar fluxes are available, the full divergences of stresses and fluxes are computed and added to the right-hand side of the mean prognostic equations for momentum, potential temperature, water vapor mixing ratio, and any other prognostic scalar variables of interest.

$$
\begin{bmatrix}
\frac{q}{2\ell_1}+2\frac{\partial U}{\partial x} & -\frac{\partial V}{\partial y} & -\frac{\partial W}{\partial z} & 2\frac{\partial U}{\partial y}-\frac{\partial V}{\partial x} & 2\frac{\partial U}{\partial z}-\frac{\partial W}{\partial x} & -\frac{\partial V}{\partial z}-\frac{\partial W}{\partial y} & 0 & 0 & \beta g & 0 \\
-\frac{\partial U}{\partial x} & \frac{q}{2\ell_1}+2\frac{\partial V}{\partial y} & -\frac{\partial W}{\partial z} & 2\frac{\partial V}{\partial x}-\frac{\partial U}{\partial y} & -\frac{\partial U}{\partial z}-\frac{\partial W}{\partial x} & 2\frac{\partial V}{\partial z}-\frac{\partial W}{\partial y} & 0 & 0 & \beta g & 0 \\
-\frac{\partial U}{\partial x} & -\frac{\partial V}{\partial y} & \frac{q}{2\ell_1}+2\frac{\partial W}{\partial z} & -\frac{\partial U}{\partial y}-\frac{\partial V}{\partial x} & 2\frac{\partial W}{\partial x}-\frac{\partial U}{\partial z} & 2\frac{\partial W}{\partial x}-\frac{\partial V}{\partial z} & 0 & 0 & -2\beta g & 0 \\
\frac{\partial V}{\partial x} & \frac{\partial U}{\partial y} & 0 & \frac{q}{3\ell_1}+\frac{\partial U}{\partial x}+\frac{\partial V}{\partial y} & \frac{\partial V}{\partial z} & \frac{\partial U}{\partial z} & 0 & 0 & 0 & 0 \\
\frac{\partial W}{\partial x} & 0 & \frac{\partial U}{\partial z} & \frac{\partial W}{\partial y} & \frac{q}{3\ell_1}+\frac{\partial U}{\partial x}+\frac{\partial W}{\partial z} & \frac{\partial U}{\partial y} & -\beta g & 0 & 0 & 0 \\
0 & \frac{\partial W}{\partial y} & \frac{\partial V}{\partial z} & \frac{\partial W}{\partial x} & \frac{\partial V}{\partial x} & \frac{q}{3\ell_1}+\frac{\partial V}{\partial y}+\frac{\partial W}{\partial z} & 0 & -\beta g & 0 & 0 \\
\frac{\partial \Theta}{\partial x} & 0 & 0 & \frac{\partial \Theta}{\partial y} & \frac{\partial \Theta}{\partial z} & 0 & \frac{q}{3\ell_2}+\frac{\partial U}{\partial x} & \frac{\partial U}{\partial y} & \frac{\partial U}{\partial z} & 0 \\
0 & \frac{\partial \Theta}{\partial y} & 0 & \frac{\partial \Theta}{\partial x} & 0 & \frac{\partial \Theta}{\partial z} & \frac{\partial V}{\partial x} & \frac{q}{3\ell_2}+\frac{\partial V}{\partial y} & \frac{\partial V}{\partial z} & 0 \\
0 & 0 & \frac{\partial \Theta}{\partial z} & 0 & \frac{\partial \Theta}{\partial x} & \frac{\partial \Theta}{\partial y} & \frac{\partial W}{\partial x} & \frac{\partial W}{\partial y} & \frac{q}{3\ell_2}+\frac{\partial W}{\partial z} & -\beta g \\
0 & 0 & 0 & 0 & 0 & 0 & \frac{\partial \Theta}{\partial x} & \frac{\partial \Theta}{\partial y} & \frac{\partial \Theta}{\partial z} & \frac{q}{\Lambda_2}
\end{bmatrix}
\begin{bmatrix}
\langle u^2 \rangle \\ \langle v^2 \rangle \\ \langle w^2 \rangle \\ \langle uv \rangle \\ \langle uw \rangle \\ \langle vw \rangle \\ \langle u\theta \rangle \\ \langle v\theta \rangle \\ \langle w\theta \rangle \\ \langle \theta^2 \rangle
\end{bmatrix}
=
\begin{bmatrix}
\frac{q^3}{6\ell_1}+3C_1 q^2\frac{\partial U}{\partial x} \\
\frac{q^3}{6\ell_1}+3C_1 q^2\frac{\partial V}{\partial y} \\
\frac{q^3}{6\ell_1}+3C_1 q^2\frac{\partial W}{\partial z} \\
C_1 q^2\left(\frac{\partial V}{\partial x}+\frac{\partial U}{\partial y}\right) \\
C_1 q^2\left(\frac{\partial W}{\partial x}+\frac{\partial U}{\partial z}\right) \\
C_1 q^2\left(\frac{\partial W}{\partial y}+\frac{\partial V}{\partial z}\right) \\
0 \\ 0 \\ 0 \\ 0
\end{bmatrix}
\quad (11)
$$

2.5 The PBL Approximation

In the situation where the horizontal length scale is much greater than the PBL vertical length scale height (i.e., $\Delta x >> z_i$), the PBL approximation may be invoked (e.g., Mellor 1973). Under this assumption of horizontal homogeneity, horizontal gradients of turbulent stresses and fluxes are identically zero. Additionally, the vertical gradient of $\overline{w^2}$ may be neglected. This means that only the vertical gradients of two components of turbulent stress, $\overline{uw}$ and $\overline{vw}$, and one component of turbulent flux, $\overline{w\theta}$, affect the evolution of the mean fields. This approach is commonly followed in current TKE-based 1D PBL parameterizations.

As an intermediate step to implementing the full 3D PBL parameterization, we develop a hybrid approach where all the six components of the turbulent stress tensor and three components of the sensible heat gradient vector are diagnosed, and the full divergence of both stress tensor and flux vector computed. However, in this case, the PBL approximation (i.e., neglecting horizontal derivatives) is used to develop the diagnostic equations. In the context of the full matrix solution, the PBL approximation assumes that any horizontal gradients, in addition to the vertical gradient of the vertical velocity, appearing in the matrix can be set equal to zero, leading to the below simplified set of linear algebraic equations.

$$\begin{bmatrix} \frac{q}{2\ell_1} & 0 & 0 & 0 & 2\frac{\partial U}{\partial z} & -\frac{\partial V}{\partial z} & 0 & 0 & \beta g & 0 \\ 0 & \frac{q}{2\ell_1} & 0 & 0 & -\frac{\partial U}{\partial z} & 2\frac{\partial V}{\partial z} & 0 & 0 & \beta g & 0 \\ 0 & 0 & \frac{q}{2\ell_1} & 0 & -\frac{\partial U}{\partial z} & -\frac{\partial V}{\partial z} & 0 & 0 & -2\beta g & 0 \\ 0 & 0 & 0 & \frac{q}{3\ell_1} & \frac{\partial V}{\partial z} & \frac{\partial U}{\partial z} & 0 & 0 & 0 & 0 \\ 0 & 0 & \frac{\partial U}{\partial z} & 0 & \frac{q}{3\ell_1} & 0 & -\beta g & 0 & 0 & 0 \\ 0 & 0 & \frac{\partial V}{\partial z} & 0 & 0 & \frac{q}{3\ell_1} & 0 & -\beta g & 0 & 0 \\ 0 & 0 & 0 & 0 & \frac{\partial \Theta}{\partial z} & 0 & \frac{q}{3\ell_2} & 0 & \frac{\partial U}{\partial z} & 0 \\ 0 & 0 & 0 & 0 & 0 & \frac{\partial \Theta}{\partial z} & 0 & \frac{q}{3\ell_2} & \frac{\partial V}{\partial z} & 0 \\ 0 & 0 & \frac{\partial \Theta}{\partial z} & 0 & 0 & 0 & 0 & 0 & \frac{q}{3\ell_2} & -\beta g \\ 0 & 0 & 0 & 0 & 0 & 0 & 0 & 0 & \frac{\partial \Theta}{\partial z} & \frac{q}{\Lambda_2} \end{bmatrix} \begin{bmatrix} \langle u^2 \rangle \\ \langle v^2 \rangle \\ \langle w^2 \rangle \\ \langle uv \rangle \\ \langle uw \rangle \\ \langle vw \rangle \\ \langle u\theta \rangle \\ \langle v\theta \rangle \\ \langle w\theta \rangle \\ \langle \theta^2 \rangle \end{bmatrix} = \begin{bmatrix} \frac{q^3}{6\ell_1} \\ \frac{q^3}{6\ell_1} \\ \frac{q^3}{6\ell_1} \\ 0 \\ C_1 q^2 \frac{\partial U}{\partial z} \\ C_1 q^2 \frac{\partial V}{\partial z} \\ 0 \\ 0 \\ 0 \\ 0 \end{bmatrix} \quad (12)$$

2.6 Idealized Simulations to Test the New Parameterization

In order to test the capabilities of the 3D PBL scheme, we use the WRF model to configure an idealized mountain-valley case of a growing convective boundary layer. We describe the specific model configuration, in addition to the results of this case. Motivation for this particular case study stems from the fact that horizontally varying topography represents one of the main situations under which the PBL approximation is not an appropriate assumption. During periods of solar insolation in mountain-valley terrain, the variation in elevation induces a thermally driven valley circulation and, therefore, horizontally heterogeneous conditions; thus, it is necessary to consider horizontal gradients in such a scenario in order to accurately calculate the turbulent stress divergence.

To examine the impact of the new 3D PBL parameterization in complex terrain, we configured an idealized mountain-valley case based on the studies by Schmidli and Rotunno (2010), Schmidli (2013), and Wagner at al. (2014). The spatial dimensions of our domain are $(x, y, z) = (40, 20, 5)$ kilometers (km), and we assign periodic boundary conditions in both the x and y directions. The choice of topography follows Schmidli and Rotunno (2010; Figure 2.1), and we use the following analytical expression to determine the elevation, z, as follows:

$$z = h(x,\ y) = h_p h_x(x) \quad (13)$$

with

$$h_x(x) = \begin{cases} 0 & |x| \le X_1 \\ \frac{1}{2} - \frac{1}{2}\cos\left(\pi \frac{|x| - X_1}{S_x}\right) & X_1 < |x| < X_2 \\ 1 & X_2 \le |x| \le X_3 \\ \frac{1}{2} + \frac{1}{2}\cos\left(\pi \frac{|x| - X_3}{S_x}\right) & X_3 < |x| < X_4 \\ 0 & |x| \ge X_4 \end{cases} \tag{14}$$

where $h_p = 1.5$ km is the valley depth, and $S_x = 9$ km is the slope width. We maintain consistency with Schmidli and Rotunno (2010) by setting $X_1 = 0.5$ km, $X_2 = 9.5$ km, $X_3 = 10.5$ km, and $X_4 = 19.5$ km to create a valley floor and mountain ridge width of 1 km. The highest resolution topography is generated at $\Delta x = 50$ m before interpolating to the respective coarser resolution domains.

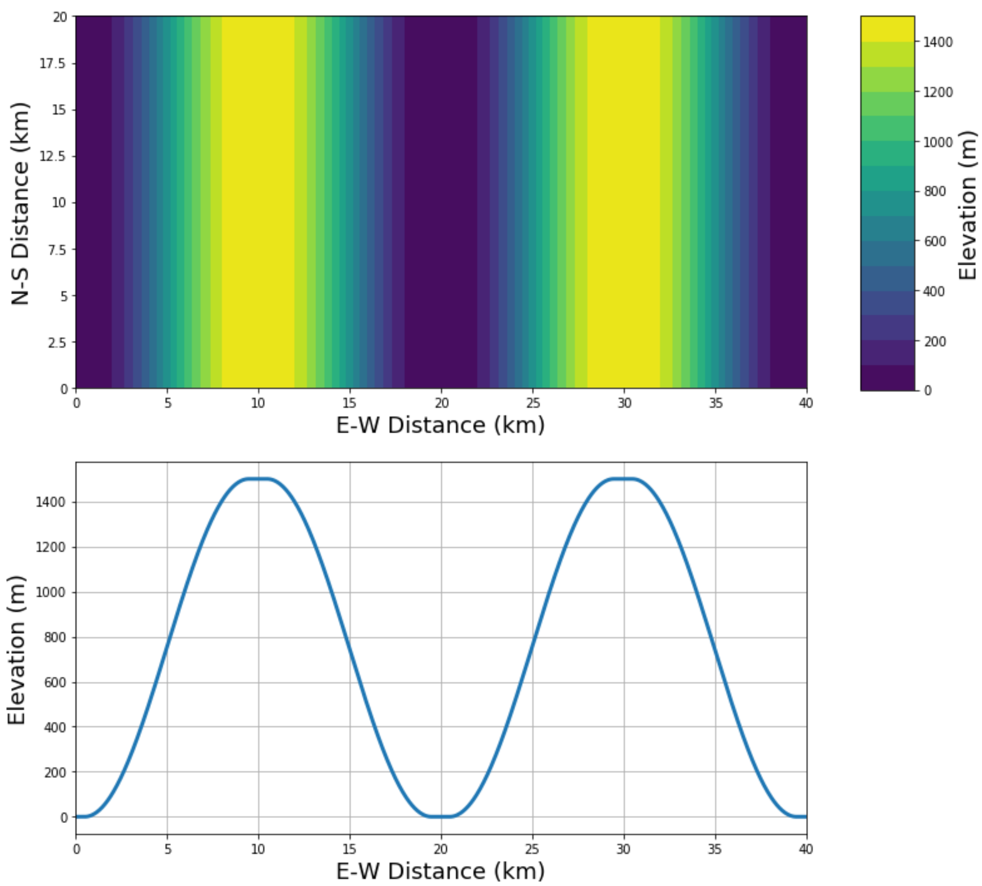

Figure 2.1. Idealized topography used for the simulations. Top and bottom panels show x-y and x-z cross sections of the surface elevation.

We run a suite of sensitivity simulations whereby we alter the horizontal grid cell spacing, as well as the turbulence closure option. The different turbulence closure options are shown in Table 2.1. For each closure option, we run simulations at $\Delta x = (1000, 500, 250)$ m in order to capture differences between simulations in the gray zone. We set the model top to 5,000 m and use 76 specified eta levels in the vertical with grid cell spacing, $\Delta z \approx 10 - 50$ m in the lowest 2 km, stretching up to ~100 m thereafter. We prescribe a horizontally homogeneous surface heat flux, $Q = 145 \text{ W } m^{-2}$. As in Wagner et al. (2014), our simulations are initialized with an atmosphere at rest, a surface potential temperature of 297 kelvin (K), and a constant potential temperature lapse rate of 3 K km^{-1}. We ignore humidity (dry atmosphere) and set the Coriolis parameter to zero. We trigger turbulence at initialization by assigning randomly distributed potential temperature perturbations of 0.5 K to the lowest four model grid cells. The simulations are integrated for five hours (h) to focus on the well-developed mountain-valley thermal circulation.

Table 2.1. Various model configurations using the 3D PBL scheme for the idealized mountain-valley simulation.

Reference Name	Closure Approach
SMAG	3D PBL w/PBL approximation (vertical mixing) and Smagorinsky (horizontal mixing)
3D-APPROX	3D PBL w/PBL approximation (vertical and horizontal mixing)
3D-FULL	3D PBL (vertical and horizontal mixing)

We now present vertical cross sections of the *u*-wind component (i.e., cross-valley) wind speed from the simulations with Δx = 500 m at t = 5 h (Figure 2.2). Each of the three different closure options, which handle the 3D mixing in different ways, are able to reproduce the double thermal circulation cells generated by the combined terrain and surface heating. The first circulation pattern is seen within the valley, where surface heating leads to upslope flow and the development of an inversion at ~1,200 m above ground level (AGL). There is a maximum in upslope wind speed confined to a thin layer near the surface, and this structure will be examined in more detail in Figure 2.4. The thermal circulation leads to return flow directed toward the center of the valley and just below the inversion. The second circulation pattern is seen above the valley, whereby a secondary inversion develops at ~2,400 m AGL and causes westward (eastward) flow on the east (west) side of the valley with return flow below. In general, the 3D-APPROX simulation shows the weakest thermal inversion strengths and related cross-valley wind speeds; this is especially evident within the circulation cell above the mountain peaks. Additionally, the circulation cells are more coherent in the SMAG and 3D-FULL simulations.

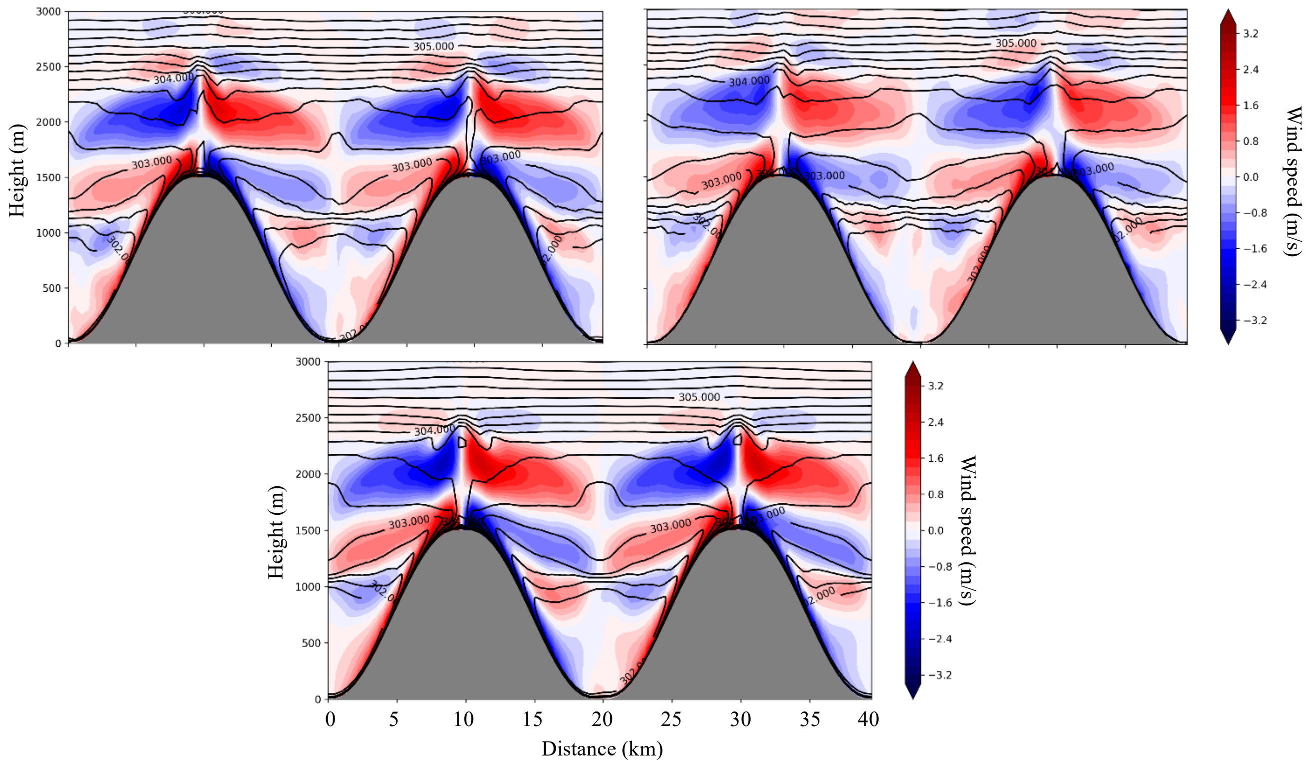

Figure 2.2. Vertical cross sections of the entire east-west mountain-valley domain (Δx = 500 m) showing along-valley averaged contour fill of *u*-wind component (m/s) and contour lines of potential temperature (K) at t = 5h. Top-left, top-right, and bottom panels show output from SMAG, 3D-APPROX, and 3D-FULL, respectively.

Figure 2.3 shows vertical cross sections of the eastern portion of the domain (18 < x < 32 km) to highlight the mountain-valley thermal circulation. Here, we plot color contours of vertical velocity along with potential temperature contours and wind arrows. Two main features are evident in this figure. First, the vertical velocity field at x = 30 km is weakest in the 3D-APPROX configuration and strongest in the 3D-FULL configuration. Also, structures in the lower portion of the valley are more apparent in the SMAG and 3D-APPROX simulations compared to the 3D-FULL simulation. These motions are likely a result of so-called modeled convectively induced secondary circulations (Ching et al. 2014), which arise in gray zone simulations when the 3D turbulent mixing is not handled appropriately. Therefore, it appears as though the more theoretically accurate closure technique (3D-FULL) may result in a better solution; however, additional analysis, including conducting LES, is required in order to examine this hypothesis in more detail.

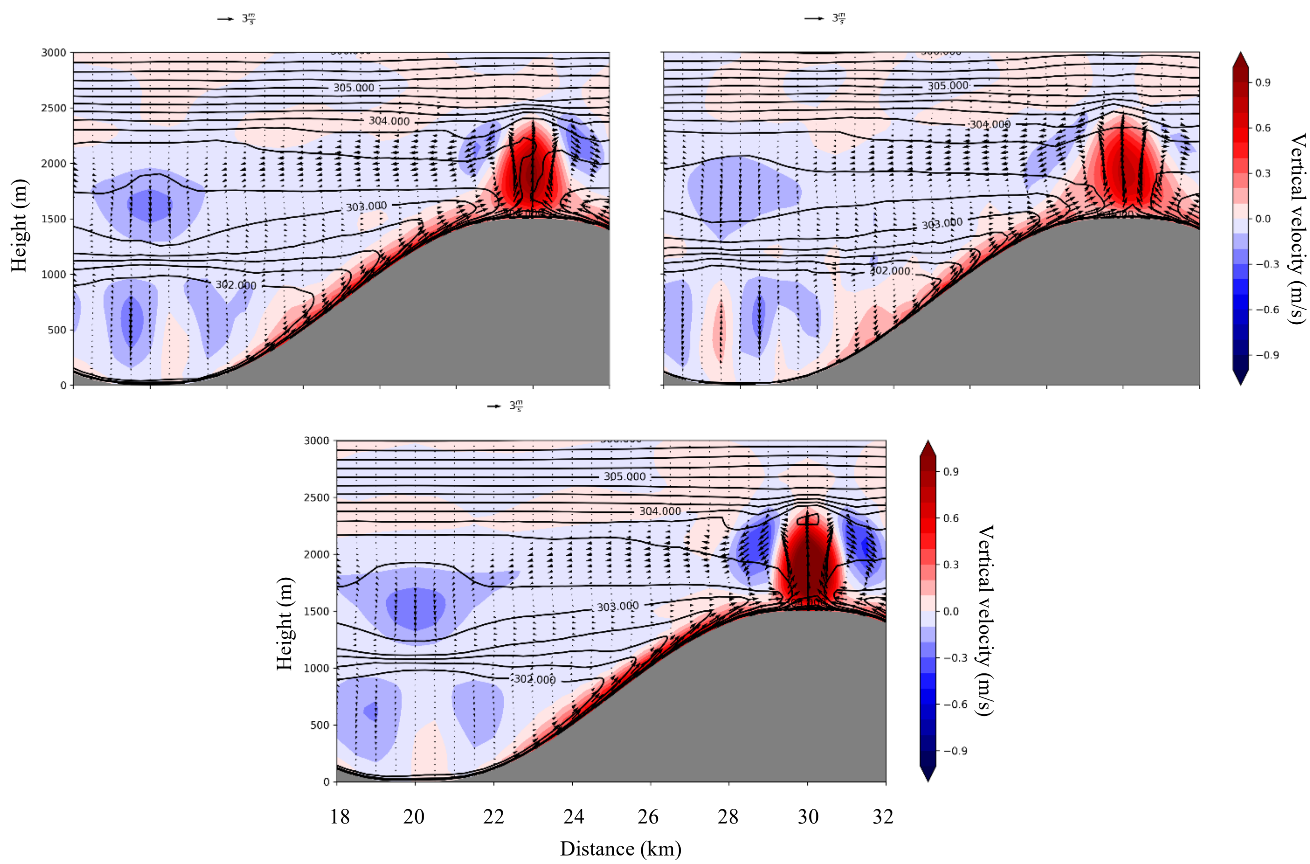

Figure 2.3. Vertical cross sections of the eastern portion of the domain (Δx = 500 m) showing along-valley averaged contour fill of vertical velocity (m/s), contour lines of potential temperature (K), and wind flow in the two-dimensional (2D) x-z plane at t = 5 h. The wind vectors are scaled based on the x:z aspect ratio, and a 3-m/s reference vector is shown above each panel. Top-left, top-right, and bottom panels show output from SMAG, 3D-APPROX, and 3D-FULL, respectively.

In order to better examine the vertical structure of the upslope wind flow along the eastern slope of the valley, in addition to the return flow above the valley inversion, we plot vertical profiles of the along-valley averaged *u*-wind component (Figure 2.4). Here, we show results for all simulations conducted to elucidate any differences between those configurations with different mixing options, as well as horizontal grid spacing. For all simulations at x = 22 km (+2 km from the center of the valley), a peak in upslope (positive *u*) winds is seen near the surface with a return flow (negative *u*) below the valley inversion. For the profiles at both x = 22 and 224 km, both the upslope and return flow wind speeds are strongest for the simulations with Δx = 1,000 m, and there is also a spatial displacement of the peak in return flow wind speed. At x = 28 km, the spatial displacement is not as apparent; however, as the horizontal grid spacing decreases, the *u* wind speed becomes weaker. Large differences in the wind profiles are not as evident when comparing the mixing options, suggesting that these results are more sensitive to the horizontal grid spacing compared to the closure option. We will conduct further analysis to understand the fundamental reasons for these differences.

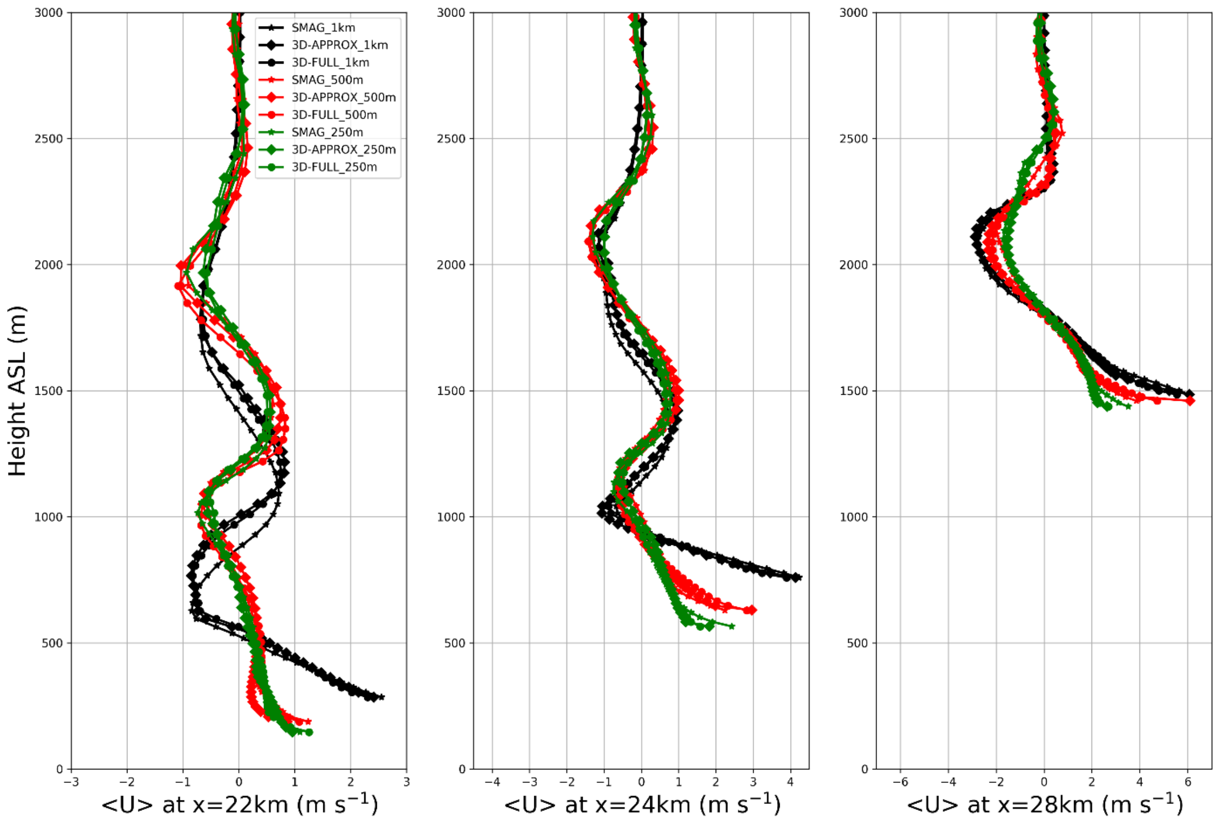

Figure 2.4. Vertical profiles of along-valley averaged *u*-wind component (m/s) at different locations in the cross-valley direction. Left, middle, and right panels show profiles at x = 22, 24, and 28 km (+2, +4, and +8 km from the center of the valley), respectively. Black, red, and green lines represent simulations with Δx = 1,000, 500, and 250 m simulations, respectively. Star, diamond, and circle markers represent simulations using SMAG, 3D-APPROX, and 3D-FULL mixing options, respectively. Note that the x-axis scales are different in all three panels.

While the results presented in this report are preliminary and show only comparisons among various mixing options within the new 3D PBL scheme, they compare well with the results from Schmidli and Rotunno (2010), Schmidli (2013), and Wagner at al. (2014). A more in-depth analysis for this particular case, including conducting high-resolution LES and examining turbulence statistics, is under way. Moreover, a manuscript synthesizing these results, in addition to results from other idealized configurations (i.e., sea breeze case and convective cell/roll convection case), is currently in preparation (Juliano et al., in press).

3.0 Characterization of Turbulence Scale from Scanning Lidar Data

Flow structures of the atmospheric boundary layer (ABL) close to the surface depend on the forcing conditions they receive from the surface, as well as the winds in the ABL. These structures help transfer mass and energy in space and impact the growth of the ABL. Details of flow structures are often studied using resolved flow from numerically simulated flow fields, such as from LES. Instruments, including remote sensing devices (e.g., lidar) can provide only sparse data in space. Because of this, the validation of numerically simulated flow with spatiotemporally resolved observational data is challenging. Similarly, the detailed study of flow structures using observations is a difficult task due to a lack of resolved data. This work employs an ensemble of velocity data collected from Doppler scanning lidar to investigate the turbulent flow structures near the surface. The following paragraphs describe the method of selecting the lidar data, the tools used to analyze the data, and a brief discussion of the results.

3.1 Lidar Data

This study uses lidar data that were collected from 2015 to 2017 during the WFIP2 field experiment (Shaw et. al 2019). The scanning lidar provided the radial velocity data at three scanning modes: plan position indicator (PPI), range height indicator, and vertically staring. Figure 3.1a shows the location of the scanning lidar in Oregon, near the Columbia Gorge, and the surrounding terrain from the lidar. The data from the lidar were considered only from the sector depicted in Figure 3.1b—solid dots on the top of the terrain height contour. In this report, however, we analyzed only the PPI scanned data, which were further down-selected using the following criteria: 1) westerly flow, 2) 2.5° beam elevation angle, 3) 50° sector (due east from the lidar, hereafter called the east-sector), and 4) radial distance of 2.5 km from lidar. The temporal resolution of the lidar is 0.5 second, and the lidar scans azimuthally at 1° resolution, requiring 25 seconds to complete the east-sector shown in Figure 3.1b. The spatial resolution along the radial direction is 100 m. These PPI scans were further categorized based on the magnitude of the surface heat flux and the wind velocity, both obtained from nearby measurement sites. The categories used to bin the velocity data are based on 1) stability: stable, surface heat flux between -50 and -10 Wm^{-2}; near-neutral, surface heat flux between -5 and 10 Wm^{-2}; weakly, moderately, and strongly unstable surface heat flux between 50 and 150, 150 and 250, and 250 and 350 Wm^{-2}, respectively; and 2) the mean horizontal wind velocities, less than 5 ms^{-1}, between 5 and 10 ms^{-1}, and between 10 and 15 ms^{-1}. The combination of surface heat flux and wind velocity provide 15 groups that are used in the analysis. In addition, we considered only categories that have at least 150 cases to ensure stable statistics. The wind data from the lidar from various cases were analyzed using spectral and proper orthogonal decomposition (POD) (Holmes et al. 2012) methods.

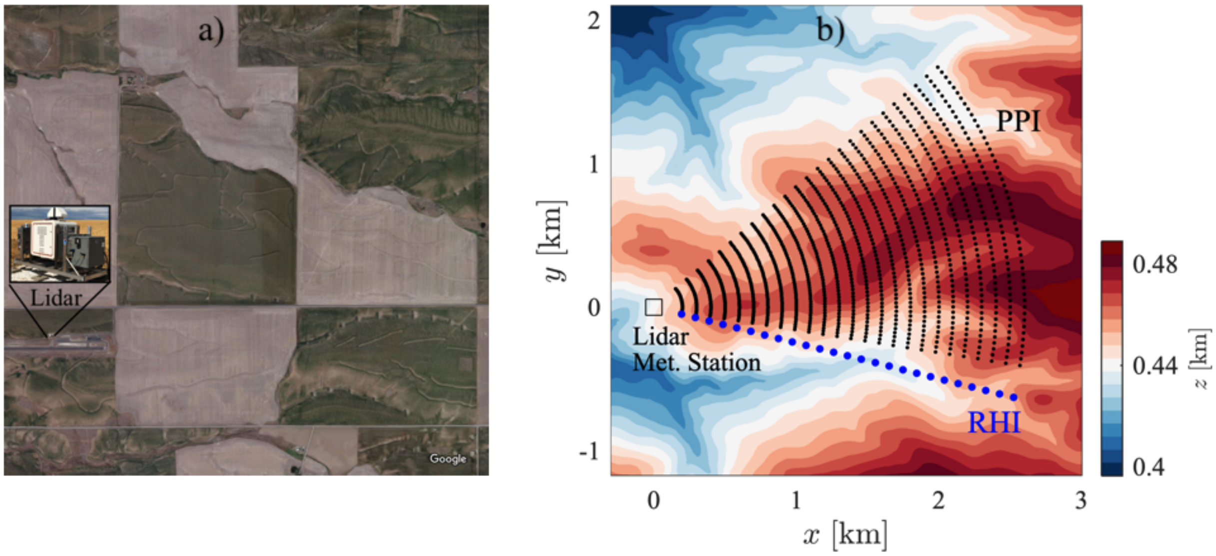

Figure 3.1. a) Location of scanning Doppler lidar in the terrain; b) the sector of scanned data by the lidar on the top of the terrain heigh contour.

3.2 Turbulent Energy in the Flow

Spectral energy was used to evaluate the turbulent energy in the flow of various cases. Figure 3.2 shows the spectra for 14 cases, derived using radial velocity data from 25 radial locations at an azimuthal angle of 100° (relative to north). The mean spectra for each case was obtained by averaging the spectra from at least 150 east-sectors. The results show that the magnitude of spectral energy is dependent on the magnitude of both wind speed and surface heat flux. For cases with wind velocity < 5 ms^{-1}, 5 to 10 ms^{-1}, and 10 to 15 ms^{-1}, the spectral energy—particularly in the higher wave number space—decreases when the magnitude of the heat flux decreases and when the heat flux changes from positive to the negative values. The rate of decrease of spectral energy in the three velocity cases, however, are different: the cases with smaller wind velocity show a large drop in magnitude. Similar behavior of energy decrease can be seen for cases with different heat fluxes (see the inset). The large drop in spectral energy is seen for the cases with negative heat flux. For a higher wave number, the spectra follow a -5/3 slope for most of the cases, showing the inertial subrange in the data. In the case of positive heat flux conditions, the -5/3 slope starts near the wavelength that corresponds to ~1.2 km, a typical characteristic length scale for the unstable atmospheric conditions; however, the inertial subrange in the case with negative heat flux appears to follow the -5/3 slope differently: the slope displays the inertial range characteristics in the larger wave number region (< 500 m). The spectral energy in the lowest wave numbers for the case with negative heat flux is larger than that for the case with positive heat flux. This indicates that the kinetic energy of the flow accumulates more in the lower wave numbers when the heat flux is negative. The spectral energy of the various cases shows that the kinetic energy of the turbulent flow is sensitive to larger wind velocity and heat flux quantities.

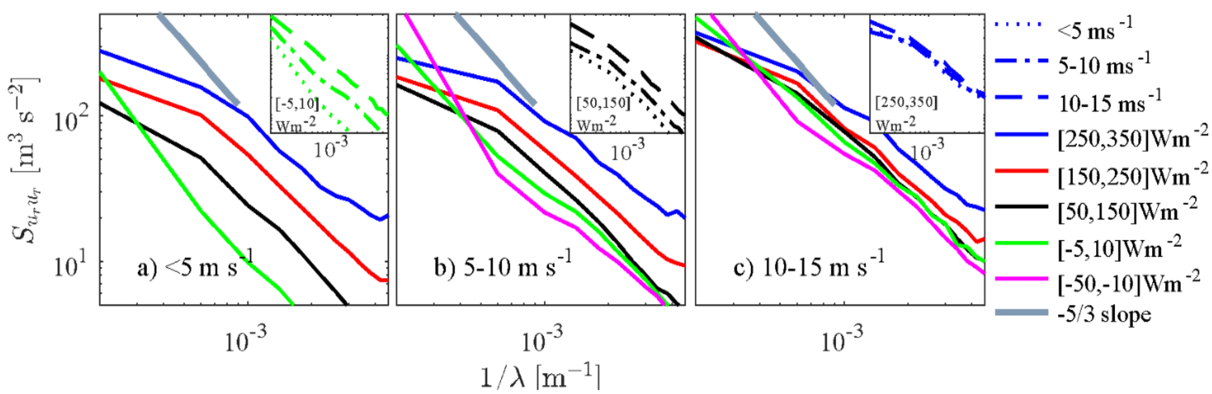

Figure 3.2. Spectral energy for the cases with varying heat flux conditions for radial wind velocity a) < 5 ms^{-1}, b) 5–10 ms^{-1}, and c) 10–15 ms^{-1}. Inset shows the spectral energy for varying wind velocity for the heat fluxes [-5,10] Wm^{-2}, [50,150] Wm^{-2}, and [250,350] Wm^{-2}.

An alternative method to consider the kinetic energy contained in the flow uses coherent energy estimated using PODs. In contrast to the spectral energy approach discussed above, 2D or 3D data have been used to compute the spatial modes and coefficients of PODs. The energy estimated by POD for each mode represents the energy associated with the coherent structure of that mode. Figure 3.3 shows the POD energy of the first 15 spatial POD modes for those cases described above. The POD energy was calculated using an ensemble of radial wind velocity from at least 150 east-sectors. It is noted that the POD energy of mode numbers in each case was normalized by the POD energy of the first mode from the case with heat flux between 250 and 350 Wm^{-2}. Similar to the spectral energy, the results show that the POD energy in the higher mode numbers is sensitive to the magnitude of wind velocity and surface heat flux. For instance, cases with the largest velocities (10 to 15 ms^{-1}) and heat flux (250 to 350 Wm^{-2}; see inset) revealed similar POD energy among the cases in the high mode numbers. The POD energy for the case with heat flux between -5 and 10 Wm^{-2} increased by one order of magnitude as heat flux increased to between 10 and 15 Wm^{-2}, showing a large drop of energy. This shows that POD energy represents the kinetic energy of the turbulent flow similar to the spectral energy but in terms of coherent structures. This variation of spectral and POD energy over wave and mode number near the surface with varying forcing conditions indicates that structures play a significant role in distributing energy within the boundary layer.

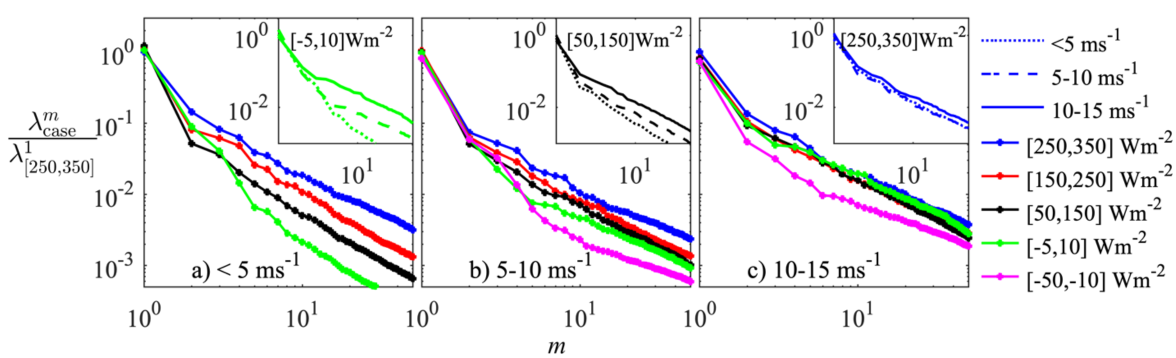

Figure 3.3. POD energy for the cases with varying heat flux conditions for wind velocity a) < 5 ms^{-1}, b) 5–10 ms^{-1}, and c) 10–15 ms^{-1}. Inset shows the POD energy for varying wind velocity for the heat fluxes [-5,10] Wm^{-2}, [50,150] Wm^{-2}, and [250,350] Wm^{-2}.

3.3 Spatial Structures

The magnitudes of the turbulent energy for the given wave number (in spectral energy) and mode number (in POD energy) are associated with the size of the spatial structures corresponding to those wave and mode numbers; therefore, the spatial POD modes herein are used to estimate the size of the coherent structures for the given mode number. Figure 3.4 shows the spatial POD modes for five representative mode numbers (i.e., 1, 4, 8, 12, and 20) for three surface heat flux conditions representing the stable, near-neutral, and unstable conditions. Note that all the spatial POD modes in Figure 3.4 are computed from the case with radial wind velocity between 5 and 10 ms^{-1}. The spatial structures of the first two modes (e.g., 1 and 4) from the three heat flux conditions (first and second column) are similar in regard to their shape and size—occupying the area with large coherent structures. This reveals that most of the energy of the flow is carried by the low mode number, and that is why all cases predicted similar ranges of POD energy in the first few modes (see Figure 3.3). Once the POD mode number increases, the shape and size of the coherent structures change noticeably with the surface heat flux. For the higher mode number, the structures become slenderer and streakier as the magnitude of surface heat flux decreases and becomes negative. The flow structures in stable conditions (negative heat flux) are dictated primarily by the shear that produces a streak-like structure close to the surface. On the other hand, the unstable condition has the effect of buoyancy in addition to the shear generation near the surface, producing different structures compared to the stable conditions. The near-neutral conditions show the shape and size of flow structures in between those two structures. In all three heat flux conditions, the streak-like structures are common, with slight change in slenderness, resulting from the slow- and fast-moving wind. In fact, the POD is able to reveal the shape and size of the coherent structures near the surface using the ensemble of velocity data.

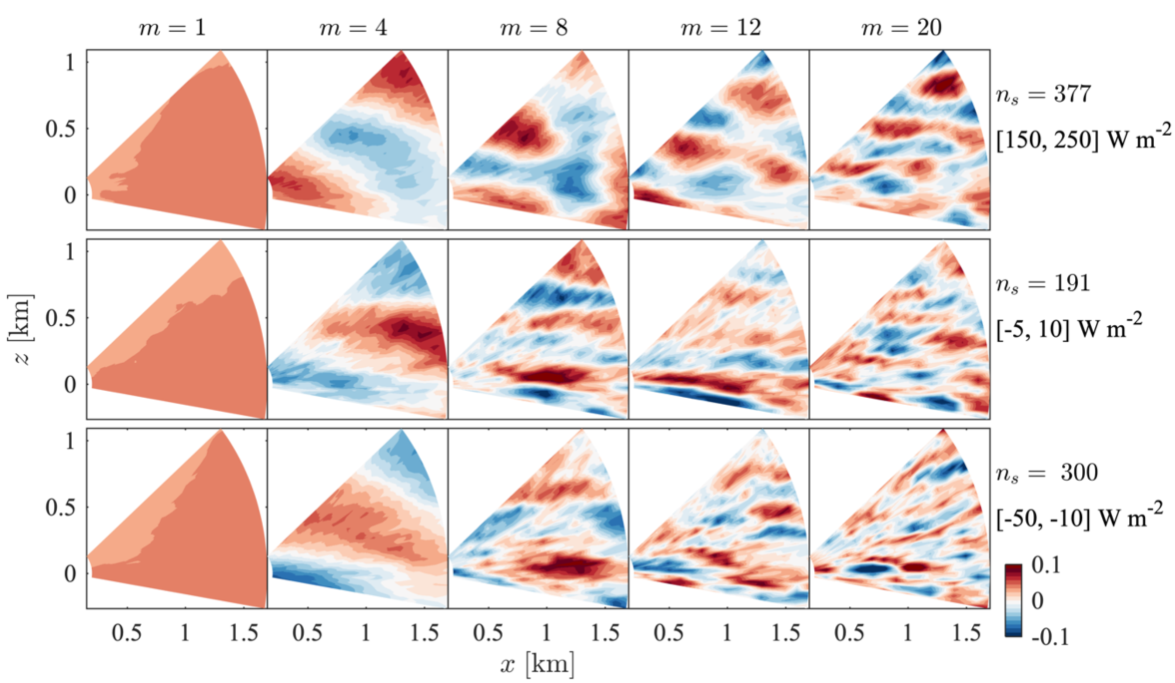

Figure 3.4. Spatial POD modes for various mode numbers, 1 through 20, for three surface heat flux conditions [-50,-10] Wm^{-2}, [-5,10] Wm^{-2}, and [150,250] Wm^{-2} for radial wind velocity 5–10 ms^{-1}.

4.0 A Machine Learning Approach to Modeling the Surface Layer

4.1 Introduction

Flows in the ABL are turbulent, characterized by a large Reynolds number, the existence of a roughness sublayer, and the absence of a viscous layer. Exchanges with the surface are, therefore, dominated by turbulent fluxes. In numerical models of atmospheric flows, turbulent fluxes of momentum, heat, and moisture must be specified at the surface. Because surface fluxes are not known a priori, they must be parameterized. Surface fluxes are currently parameterized using a semiempirical approach.

Theoretical underpinnings of the surface exchanges with the atmosphere were laid out by Monin and Obukhov (1954). They developed a similarity theory linking measurements of wind speed and temperature at a level near the surface to the friction velocity and surface flux of sensible heat. Assuming that two relevant length scales (distance from the surface, z, and Obukhov length, L) account for the effect of a solid boundary and for competing effects of shear and buoyancy, Monin and Obukhov defined a nondimensional stability parameter, z/L. A number of field studies under nearly homogeneous and stationary conditions were carried out to determine universal stability functions that modify velocity and temperature profiles under nonneutral conditions. These stability functions are determined as simple linear and nonlinear regression fits for stably stratified and unstable conditions, respectively; however, different regression parameters are obtained from different field studies (e.g., Businger et al. 1971, Dyer and Hicks 1970). Even when extreme care is taken to control the quality of the data, the scatter is large. Additionally, uncertainty emerges in parameters that are assumed to be constant, the von Karman constant, and surface roughness length. Simple regression cannot capture the relationship between governing parameters and surface layer structure under the wide range of conditions to which Monin-Obukhov similarity theory (MOST) is commonly applied. Nevertheless, in practice, these stability functions are commonly used even when the conditions of homogeneity and stationarity are not satisfied in a range of atmospheric models from global models to turbulence-resolving LES of ABL flows. We, therefore, developed an ML model for an improved surface layer parameterization using long-term surface layer observations.

To estimate surface fluxes of momentum, sensible heat, and moisture based on measurements of wind speed, temperature, humidity, as well as surface temperature and soil moisture, we developed, trained, and tested two ML models. The ML models are based on the artificial neural network (ANN) and random forest (RF) algorithms. To train and test these ML algorithms, we used several years of observations from the Cabauw mast in the Netherlands and from the National Oceanic and Atmospheric Administration's (NOAA's) Field Research Division tower in Idaho.

Even when we train the ML models on one set of data and apply them to the second set, they provide more accurate estimates of all the fluxes than MOST. Estimates of sensible heat and moisture flux are significantly improved. We have now implemented the ML model based on the RF algorithm in the WRF model. Here, we demonstrate its performance in a single column model simulation based on the GABLS 2 model intercomparison study (Svensson et al. 2011).

4.2 Monin-Obukhov Similarity Theory

MOST states that, under nonneutral stratified atmospheric conditions, the logarithmic profile is modified as a function of a stability parameter, z/L, where L is Obukhov length scale, defined as (Obukhov 1948:

$$L = -\frac{{u_*}^3}{\frac{g}{T}\overline{w'\theta_v'}} \tag{1}$$

so that:

$$\frac{\partial U}{\partial z} = \frac{u_*}{\kappa z}\Phi_M\left(\frac{z}{L}\right) \tag{2}$$

where the function, Φ_M, for momentum is determined experimentally. Similarly, the stability function, Φ_H, can be experimentally determined for a temperature profile:

$$\frac{\partial \Theta_v}{\partial z} = \frac{\theta_*}{\kappa z}\Phi_H\left(\frac{z}{L}\right). \tag{3}$$

Here, Θ_v is the mean virtual potential temperature, and θ_* is a temperature scale, defined as:

$$\theta_* = -\frac{\overline{w'\theta_v{}'}}{u_*}. \tag{4}$$

Here, z_0 is the momentum roughness length, and u_* is the surface friction velocity, defined as:

$$u_* = \sqrt[4]{\left(\overline{u'w'}\right)^2 + \left(\overline{v'w'}\right)^2} \tag{5}$$

where $\overline{u'w'}$ and $\overline{v'w'}$ are components of turbulent stress near the surface.

Due to significant differences in the structure of velocity and temperature profiles under convective and stably stratified conditions, the stability functions are estimated separately for two cases.

For a stably stratified boundary layer based on Dyer and Hicks (1970), the stability functions for momentum and heat are equal:

$$\Phi_M\left(\frac{z}{L}\right) = \Phi_H\left(\frac{z}{L}\right) = 1 + 5\frac{z}{L} \tag{6}$$

while for a convective boundary layer they are:

$$\Phi_M\left(\frac{z}{L}\right) = \left(1 - 16\frac{z}{L}\right)^{-\frac{1}{4}} \tag{7}$$

and:

$$\Phi_H\left(\frac{Z}{L}\right) = \left(1 - 16\frac{Z}{L}\right)^{-\frac{1}{2}} \tag{8}$$

Figure 4.1 depicts Dyer and Hicks (1970) and Businger et al. (1971) stability functions, two of the most commonly used sets of empirical stability functions for momentum and sensible heat flux.

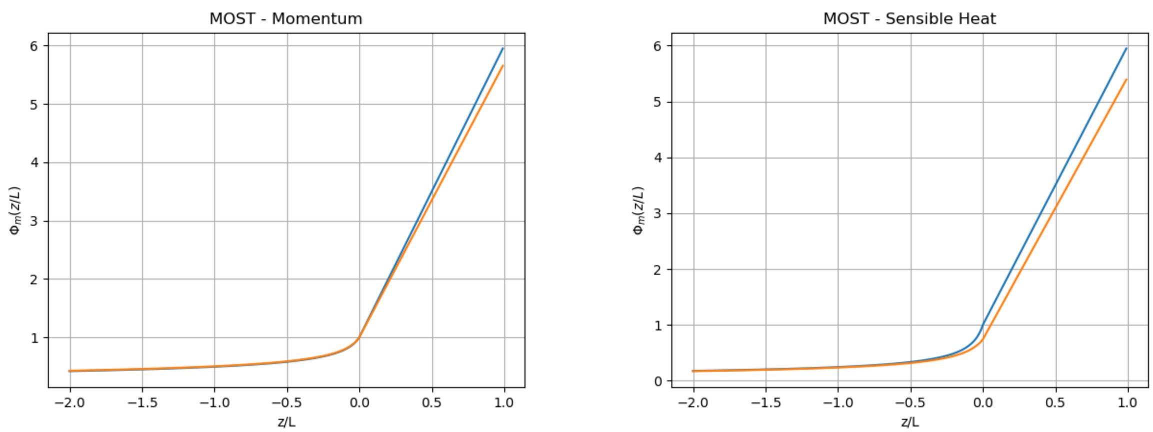

Figure 4.1. MOST momentum (left) and heat (right) universal stability functions as a function of a nondimensional stability parameter z/L. Blue lines represents Dyer-Hicks (1970) stability functions, while red lines represent Businger et al. (1971) stability functions.

The value of the von Karman constant they used was $\kappa = 0.41$. After integrating equation (2) we have:

$$U_1 - U_0 = \frac{u_*}{\kappa}\left[ln\,\frac{z_1}{z_0} + \psi_M\left(\frac{z_1}{L}\right)\right]. \tag{9}$$

For stably stratified boundary layers:

$$\psi_M\left(\frac{Z}{L}\right) = 5\frac{Z_1}{L} \tag{10}$$

so that:

$$U_1 - U_0 = \frac{u_*}{\kappa}\left[ln\,\frac{z_1}{z_0} + 5\frac{z_1}{L}\right]. \tag{11}$$

While for convective boundary layers:

$$\psi_M\left(\frac{Z}{L}\right) = -2ln\left[\frac{(1+x)}{2}\right] - ln\left[\frac{(1+x^2)}{2}\right] + 2\text{atan}(x) - \frac{\pi}{2} \tag{12}$$

where:

$$x = \left[1 - 16\frac{z}{L}\right]^{\frac{1}{4}} \tag{13}$$

so that the difference in wind speeds at two levels is:

$$U_1 - U_0 = \frac{u_*}{\kappa}\left[ln\ \frac{z_1}{z_0} - 2ln\ \left[\frac{(1+x)}{2}\right] - ln\ \left[\frac{(1+x^2)}{2}\right] + 2\text{atan}(x) - \frac{\pi}{2}\right]. \tag{14}$$

For a potential temperature, we can obtain similar relations:

$$\Theta_1 - \Theta_0 = \frac{\theta_*}{\kappa}\left[ln\ \frac{z_1}{z_\tau} + \psi_H\left(\frac{z_1}{L}\right)\right]. \tag{15}$$

Here, for stably stratified conditions:

$$\psi_H\left(\frac{z_1}{L}\right) = 5\frac{z_1}{L} \tag{16}$$

so that:

$$\Theta_1 - \Theta_0 = \frac{\theta_*}{\kappa}\left[ln\ \frac{z_1}{z_\tau} + 5\frac{z_1}{L}\right]. \tag{17}$$

While for unstable conditions:

$$\psi_H\left(\frac{z_1}{L}\right) = -2\ ln\left(\frac{1+x^2}{2}\right) \tag{18}$$

so that the difference in potential temperatures at two levels is:

$$\Theta_1 - \Theta_0 = \frac{\theta_*}{\kappa}\left[ln\ \frac{z_1}{z_\tau} - 2\ ln\left(\frac{1+x^2}{2}\right)\right]. \tag{19}$$

Here, z_τ, is the heat flux roughness length, which is often about an order of magnitude smaller than the momentum roughness length. Finally, the expression for moisture mixing ratio difference has the same form as the one for potential temperature; therefore, for the stably stratified boundary layer, the difference in moisture mixing ratio at two levels in a surface layer can be estimated using the following equation:

$$q_1 - q_0 = \frac{q_*}{\kappa}\left[ln\ \frac{z_1}{z_0} + 5\frac{z_1}{L}\right] \tag{20}$$

while for the convective ABL, the difference is:

$$q_1 - q_0 = \frac{q_*}{\kappa}\left[ln\ \frac{z_1}{z_0} - 2\ ln\left(\frac{1+x^2}{2}\right)\right]. \tag{21}$$

Equations (11), (14), (17), (19), (20), and (21) will be used to compute surface friction velocity, u_*, temperature scale, θ_*, and moisture scale, q_*.

4.3 Machine Learning Methods

We selected two ML algorithms to develop an ML model for surface layer parameterization: an ANN and an RF. These two algorithms represent different approaches to ML in terms of complexity and training requirements. In general, the RF training process is simpler, and it requires less preprocessing. The ANN algorithm includes many hyperparameters that must be tuned and, therefore, requires more experience in ML model development; however, ANNs produce much more compact models than RFs and produce smoother predictions.

4.3.1 Artificial Neural Network

An ANN is an ML method modeled after how neurons in the human brain process and learn information. The specific ANN used for this application is a multilayer perceptron trained with backpropagation (Reed and Marks 1999, Rosenblatt 1958). In a multilayer perceptron, the input data or predictors are mapped to each neuron in a hidden layer that adjusts parameters to output learned values, which in this study are the moisture scale, temperature scale, and friction velocity. The complexity of the nonlinear relationships and predictability that can be modeled are a function of the number of neurons in the hidden layer(s) and the number of hidden layers. Each neuron relies on a nonlinear activation function to modulate its output. Activated neurons show more of an effect on the model’s prediction than on neurons that are not activated. The training process iteratively adjusts the weights and biases until the error is minimized or the specified number of training iterations, or epochs, is reached. This final configuration is used to make predictions, and a minimal difference in error between training and testing datasets indicates a lack of overfitting the data. The model used here is built with the Python TensorFlow Keras framework and contains three hidden layers of 64 neurons each, 25 training epochs, a batch size of 32, ReLU activation functions, an Adam optimizer, and a learning rate of 0.001.

4.3.2 Random Forest

The RF algorithm belongs to the decision tree family of algorithms. It consists of an ensemble of decision trees where each tree in the forest is trained on a subset of the resampled original training data. The trees grown as random subsets of predictors are evaluated at each decision node (Breiman 2001) by iterating over candidate combinations of input variables and splitting thresholds at a given branch. For each input-threshold combination, the training data are split into two subsets, and the mean square error (MSE) is computed between the observed values and the means of the subset labels. The input-threshold combination with the lowest MSE is retained. The iterative process proceeds recursively until, in the final branch—i.e., the leaf—the number of examples in the subset reaches a minimum threshold or has a minimum error. The final prediction is the mean of the training instances in the final leaf node for a given sample of predictors. The RF is efficient at interpolating; however, it does not extrapolate beyond the range of training set outputs, and it performs poorly on extreme values, because it uses the mean value of the training samples in the leaf of the tree. The final prediction from the RF represents an ensemble average of the predictions from each tree in the forest that generalized well on the test data and typically has a lower error on average than any single tree in the forest. The RF regressor used in this analysis is in Python’s scikit-learn package (Pedregosa et al. 2011). We determined the optimal configuration of the RF based on evaluating the results on a subset of the training data with limitations of the size of the forest that could be implemented within WRF. The RF configuration used in this study had 200 trees, 200 maximum leaf nodes, 50 minimum samples per split and per leaf, and an MSE loss function.

4.4 Comparing the Machine Learning Surface Layer Parameter Estimates to MOST

To train the ML models, we use surface layer observations from two sites: the Cabauw mast in the Netherlands and NOAA's Field Research Division site in Idaho. To compare model predictions based on models trained at two sites, we needed to determine a common set of predictors. The common set of predictors and associated observation levels are listed in Table 4.1. While the observation levels are different between two sites, for the purpose of our analysis, we will ignore these differences.

We trained ANNs and RFs for each site, independently. We first applied the resulting ML model to test datasets from the same site from which the training dataset was derived. We then applied the models trained on the dataset from the first site to the test datasets from the second site to evaluate if a model trained in one climate could perform in another climate and, thus, determine if models can be generalized. Finally, we trained the ML models on a training dataset that merged the Idaho and Cabauw training datasets. The Cabauw dataset was split into years 2003 to 2010 for training and years 2011 to 2015 for testing, which resulted in 403,140 10-minute-averaged sets of observations in the training data and 251,805 sets in the testing data. For the Idaho dataset, we used years 2016 to 2017 for training and year 2015 for testing, which included 28,918 10-minute-averaged sets of observations in the training data and 11,770 sets in the testing data. Any instances where any of the variables were missing were removed from the datasets. The mean absolute error (MAE) and the square of the Pearson correlation coefficient (R^2) were computed for the ML model predictions and the MOST estimates with respect to observations of the friction velocity and temperature scale. The MAE and R^2 results for the independent testing datasets are shown in Table 4.2 for the Idaho test dataset and in Table 4.3 for the Cabauw dataset. These results highlight the generally superior performance of both the ANN and the RF model over MOST, with lower MAEs and higher R^2. These results also demonstrate the capability of the ML models trained in one climate to be successfully applied to another climate. Although forecast skill degrades when an ML model trained in one climate is applied to the other, the MAEs are, in general, still lower than MAEs for MOST. An exception is the ANN model for temperature scale trained with data from one site but applied to the other site. This model did not produce results as good as MOST. There are no other significant differences between the performance of the ANN versus RF.

Table 4.1. Observations from Idaho and Cabauw used as predictors in ML models. Height levels at which observations are made are indicated in the second and the third column for Idaho and Cabauw, respectively.

Observation [Units]	Idaho Height Level [m]	Cabauw Height Level [m]
Potential Temp [K]	10	10
Potential Temp [K]	15	20
Potential Temp [K]	45	40
Low-Level Wind Speed [ms^{-1}]	10	10
Low-Level Wind Dir [°]	10	10
Mid-Level Wind Speed [ms^{-1}]	15	20
Mid-Level Wind Dir [°]	15	20
Top-Level Wind Speed [ms^{-1}]	45	40
Top-Level Wind Dir [°]	45	40

Observation [Units]	Idaho Height Level [m]	Cabauw Height Level [m]
RH [%]	2	2
Global Horizontal Irradiance (GHI) [Wm^{-2}]	0	0
Pressure [hPa]	2	2
Solar Zenith Angle [°]	0	0
	Depth Level [cm]	**Depth Level [cm]**
Top-Level Soil Water Content [$m^{-3}m^{-3}$]	5	3
Top-Level Soil Temp [K]	5	3
	Difference Between Levels	
Bulk Richardson Number	10m-2m	10m-2m

The models were also trained on a combined (Idaho and Cabauw merged) training dataset and applied to each test dataset independently. These results indicate that the additional data allow both the ANN and the RF model to learn the representative patterns and perform well. It would be expected that as more sites and data are added, both models would continue to generalize better to additional areas with minimal degradation compared to a site-specific model. Note that we did not compute the moisture scale value for MOST for either dataset due to the lack of multiple moisture levels, which did not allow for a fair comparison of MOST against the RF and ANN.

Table 4.2. MAE and R^2 of the ANN and RF models trained on each dataset and applied to the Idaho test dataset using all common variables as predictors.

Idaho Test Dataset						
	MAE			**R^2**		
	u_*	θ_*	q_*	u_*	θ_*	q_*
MOST	0.110	0.174	---	0.72	0.38	---
ANN Trained on Idaho	0.051	0.085	0.025	0.83	0.79	0.16
ANN Trained on Cabauw	0.071	0.203	0.107	0.85	0.47	0.21
ANN Trained on Both	0.046	0.079	0.021	0.91	0.67	0.49
RF Trained on Idaho	0.047	0.079	0.023	0.91	0.80	0.41
RF Trained on Cabauw	0.094	0.131	0.332	0.88	0.55	0.20
RF Trained on Both	0.052	0.084	0.029	0.89	0.66	0.26

Table 4.3. MAE and R^2 of the ANN and RF models trained on each dataset and applied to the Cabauw test dataset using all common variables as predictors.

Cabauw Test Dataset						
	MAE			**R^2**		
	u_*	θ_*	q_*	u_*	θ_*	q_*
MOST	0.129	0.068	---	0.35	0.27	---
ANN Trained on Idaho	0.031	0.028	0.056	0.86	0.55	0.34
ANN Trained on Cabauw	0.056	0.108	0.118	0.93	0.81	0.70
ANN Trained on Both	0.031	0.030	0.053	0.93	0.64	0.70
RF Trained on Idaho	0.073	0.049	0.112	0.93	0.53	0.44

Cabauw Test Dataset						
	MAE			**R^2**		
	u_*	θ_*	q_*	u_*	θ_*	q_*
RF Trained on Cabauw	0.031	0.030	0.056	0.90	0.79	0.67
RF Trained on Both	0.031	0.032	0.053	0.92	0.63	0.70

The distribution of the ML model predictions compared to the predicted surface flux variables shows how the data-driven results predict the surface flux variables differently than MOST. Figure 4.2 is a 2D histogram (lighter blue color indicates higher density of instances than the darker color) that displays the differences between the observed and predicted temperature scale for Idaho from the RF (left), ANN (center), and MOST (right). Here, we can see that the ANN and the RF generally show similar distributions for the fluxes, although the RF has a more pronounced positive distribution peak for the temperature scale than the ANN. The MOST distribution differs substantially, showing no negative values below 0.5 and a well-defined mode of the distribution near zero value. For the friction velocity predictions (Figure 4.3), the RF, ANN, and MOST produce generally similar distributions. The RF shows a sharper cutoff around 0.05, while MOST gets closer to zero, and the ANN values include a few unphysical negative predictions. It would be expected that the RF has a sharper cutoff given that the hyperparameter configuration required 50 minimal samples per split and per leaf. The moisture scale distribution (Figure 4.4) is similar between the RF and ANN. The RF has most of the predictions centered very close to 0.0, but it did display a distribution of positive predictions out to 0.2. The ANN predictions were centered slightly negative around 0.02, with generally more negative than positive predictions. These results indicate that the ML models may be better at capturing the real distribution of the moisture scale, temperature scale, and friction velocity compared to the results computed from MOST.

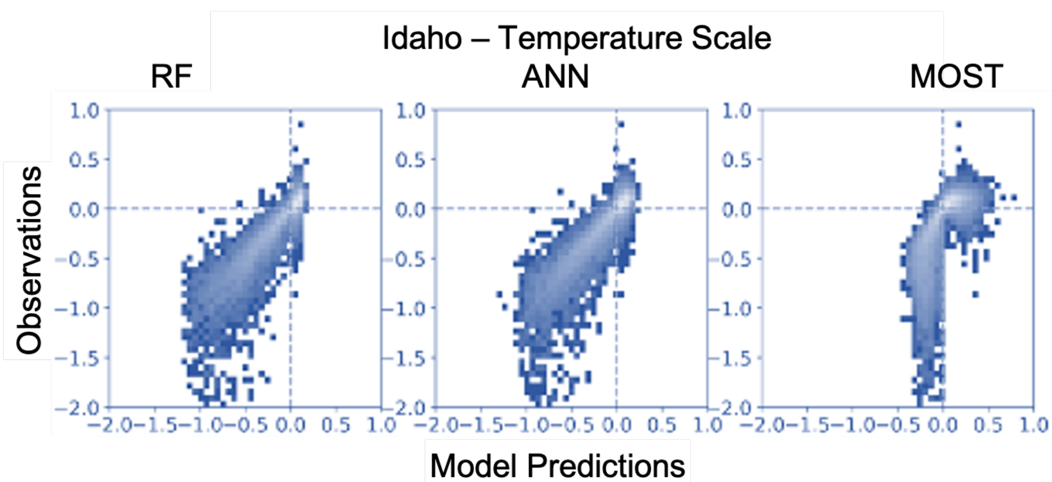

Figure 4.2. 2D histograms of the observed vs. predicted temperature scale for the Idaho dataset from RF (left), ANN (center), and MOST (right). Lighter blue represents more instances, while darker blue represents fewer instances.

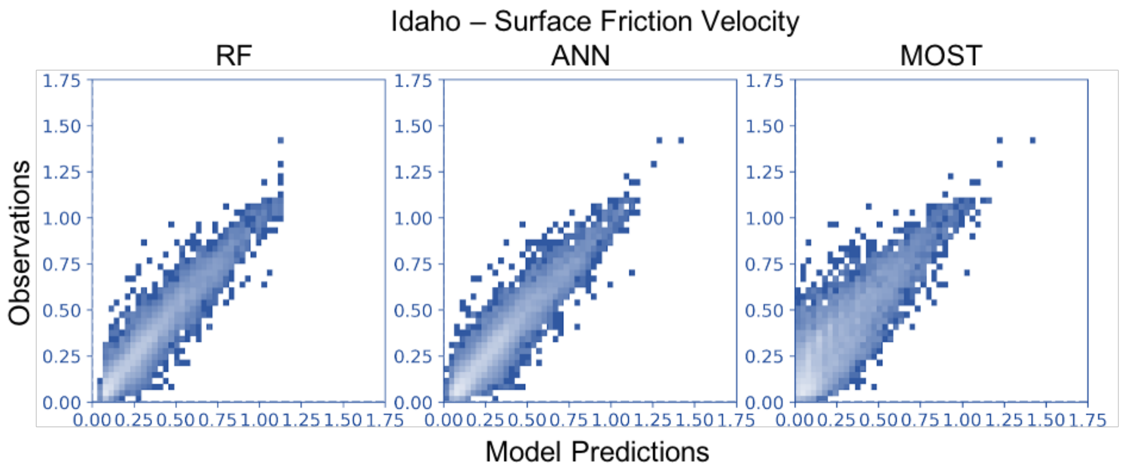

Figure 4.3. 2D histograms of the observed vs. predicted surface friction velocity for the Idaho dataset from RF (left), ANN (center), and MOST (right). Lighter blue represents more instances, while darker blue represents fewer instances.

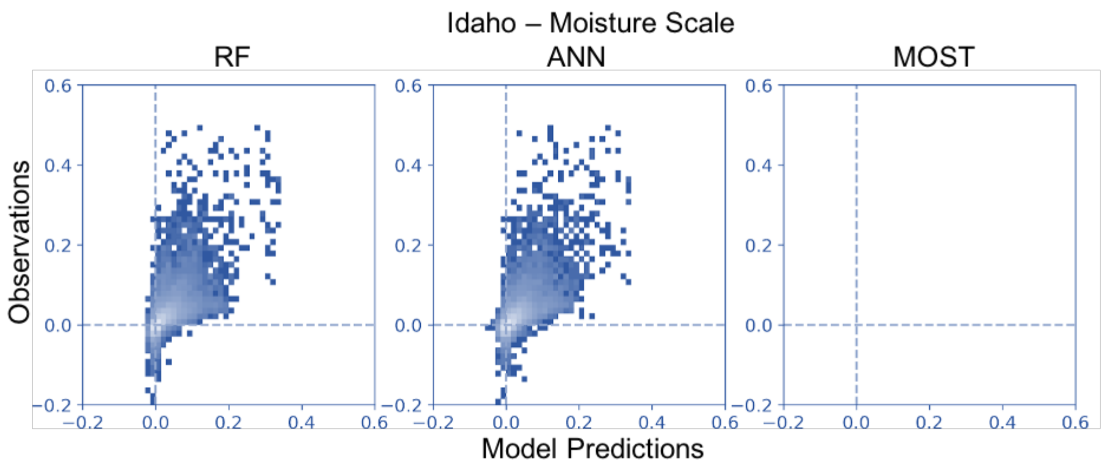

Figure 4.4. 2D histograms of the observed vs. predicted moisture scale for the Idaho dataset from RF (left), ANN (center), and MOST (right). Lighter blue represents more instances, while darker blue represents fewer instances.

4.5 Random Forest Interpretability

ML algorithms and resulting models are often mischaracterized as black boxes; however, ML algorithms include capabilities for interpretation of their results and, thus, provide physical insight that could be used for further development. One of the benefits of the RF ML methodology is its inherent interpretability. Here, we perform and evaluate one ML interpretability technique: predictor importance for the dataset from Subsection 4.4 that uses all common predictors with 10-min average data. The predictor importance plots—Figure 4.5 for the Idaho site and Figure 4.6 for the Cabauw site—show the relative importance of each of the predictors in determining the variance reduction from the decisions in the tree. It is clear from the moisture scale analysis that GHI is the most important variable, followed by the stability as measured by the bulk Richardson number. The next most important predictors capture the temperature and moisture content of the surface, which is logical given that the moisture scale quantifies the moisture flux from the surface of the earth to the surface layer of the atmosphere.

We also note that the wind speed has minimal to no importance for moisture scale, which would be expected, because winds at higher levels would have minimal impact on the flux of moisture. The temperature scale results also make physical sense with a significant dependence on the GHI, followed by the stability, temperature, and relative humidity near the surface. The importance of GHI and stability for the estimation of temperature and moisture scale is related to the fact that these predictors encode the diurnal cycle. Finally, the friction velocity results indicate that the wind speed at the lowest two levels—especially the lowest level—supply the vast majority of the value of the predictors, with minor value coming from the stability and soil temperature.

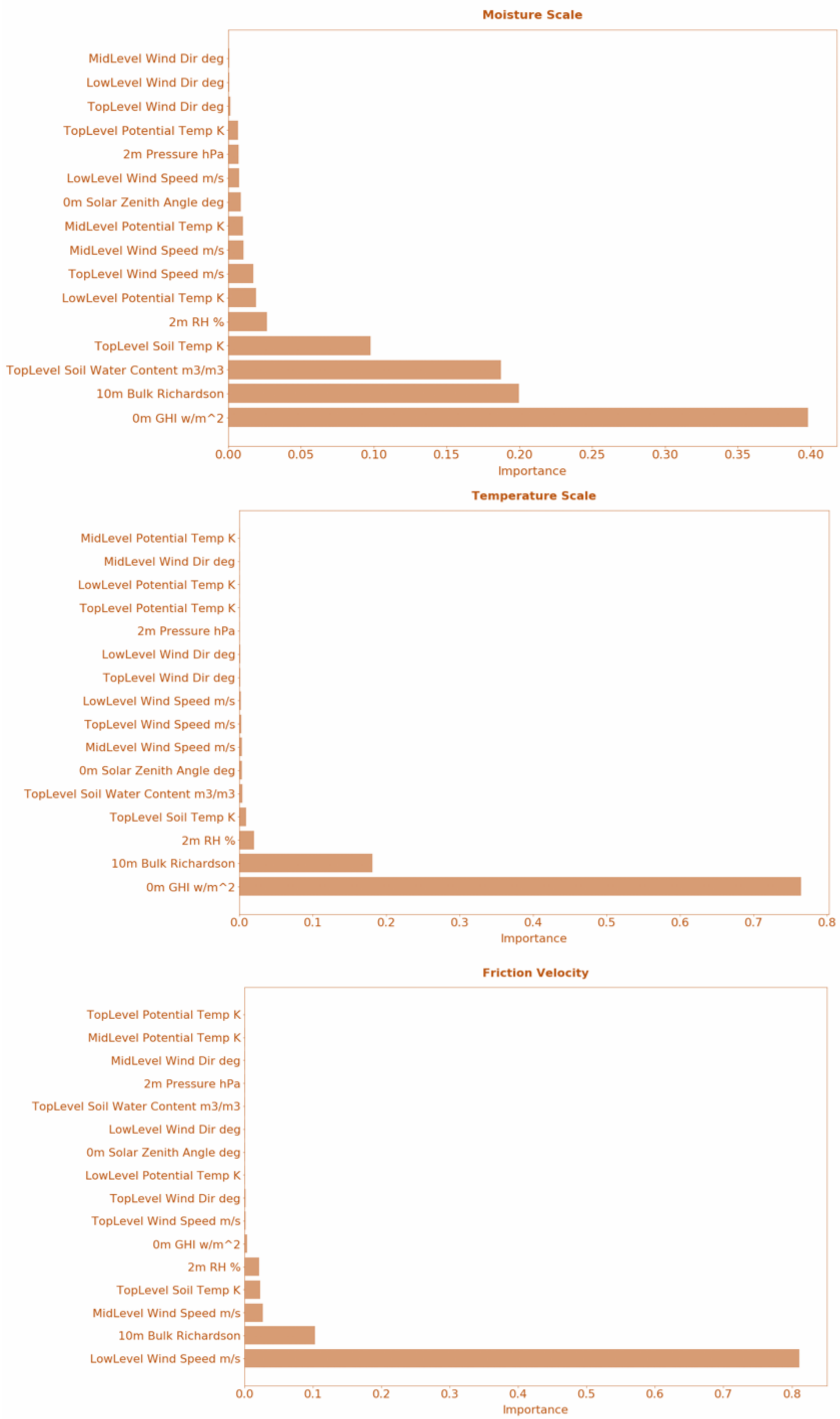

Figure 4.5. Predictor importance rankings for RF with the Idaho dataset using all common variables and the 10-min average fluxes.

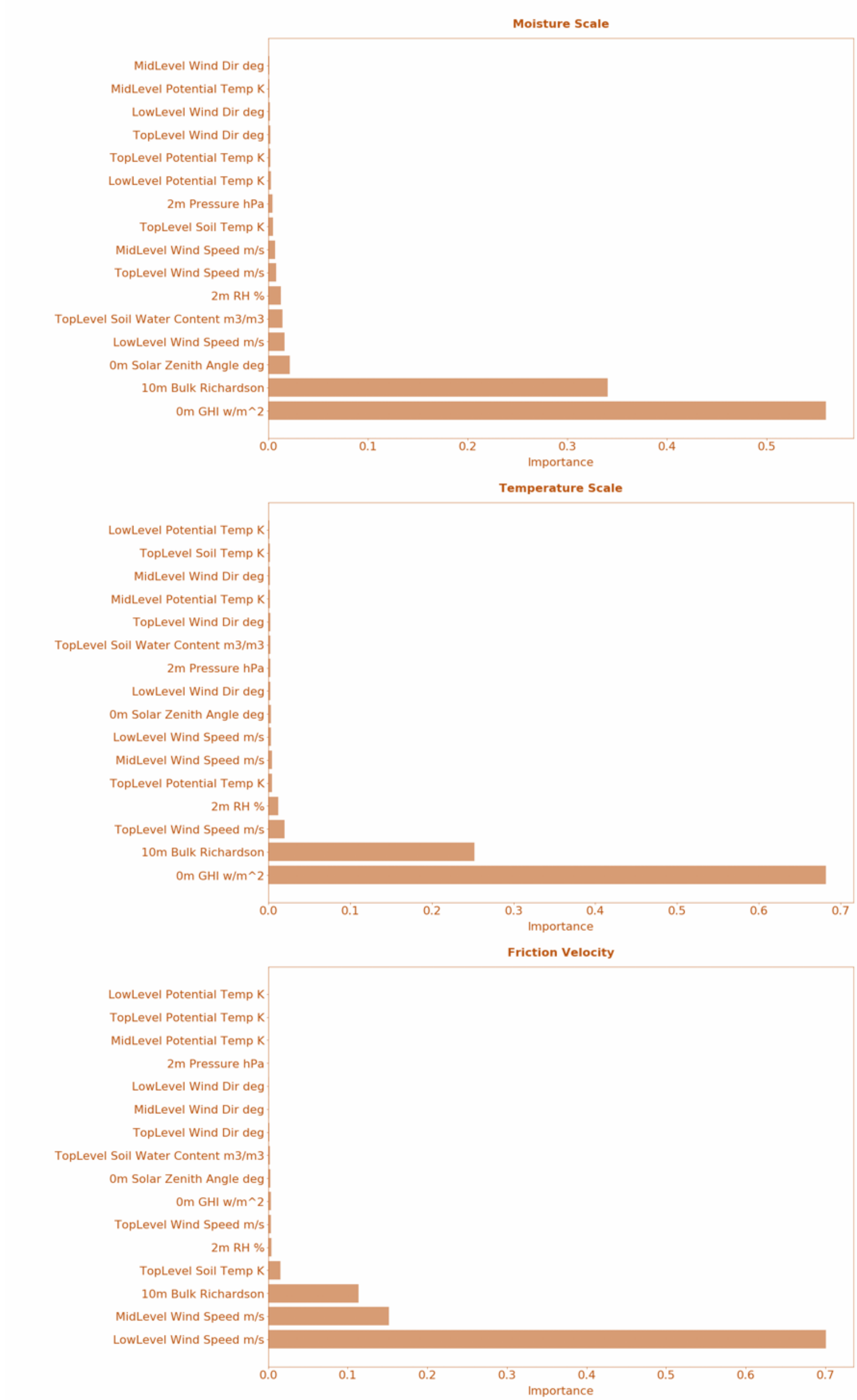

Figure 4.6. Predictor importance rankings for RF with the Cabauw dataset using all common variables and the 10-min average fluxes.

5.0 Inflow Turbulence Generation in Convective, Stable, and Neutral Conditions Over Flat Terrain

Progress was made on the inflow perturbation characterization task during FY 2020; however, the task was not completed as planned, for a variety of reasons, including code development issues, lack of data availability for one of our test cases, and staffing being redirected to other project priorities. As described in the overview, the MMC project team pivoted strongly toward offshore applications during FY 2020 to support programmatic reprioritization. This shift of emphasis, in the absence of additional staffing, necessitated a redirection of staff and resources, which came, in part, from the inflow turbulence generation task. This transfer of staffing optimized overall team productivity in light of delays within the perturbation task, including a requirement for further development of the common source code used by the team to conduct the perturbation intercomparison simulations and to examine the results, as well as an inability of the team to acquire data for one of the case studies selected to examine the performance of the perturbation methods under near-neutral conditions. The progress that was made, and the strategy to complete the task during FY 2021, are described below.

5.1 Source Code Modifications for Idealized ABL Flow

The [MMC WRF model source code](https://github.com/a2e-mmc/WRF) (https://github.com/a2e-mmc/WRF) used by the participants to conduct the simulations was modified to enable further flexibility in setting up and conducting the idealized simulations required to complete the task. Further modifications include implementing two different methods to specify the surface heat flux through the WRF namelist.input file, an option to supply a surface skin temperature heating or cooling rate, and an ability to enable or disable initial condition perturbations (not the same as inflow perturbations).

A user-defined value of the surface sensible heat flux (spec_hfx) in Wm^{-2} can be specified two different ways: either pointwise (spec_ideal=1) or as a constant, domain average value (spec_ideal = 2). These idealized forcing approaches are relayed into the Monin-Obukhov similarity surface layer physics option (sf_sfclay_physics = 1), whose source code is contained within module_sf_sfclayrev.F. Each of the approaches is based upon inversion of the equation for the surface sensible heat flux defined within module_sf_sfclayrev.F.:

$$\text{hfx(I,j)} = \text{flhc(i,j)} *(\text{t\_surf(i,j)} - \text{t\_air(i,1,j)}). \qquad (1)$$

Here, hfx(i,j) is the surface sensible heat flux, flhc(i,j) is the exchange coefficient, t_surf(i,j) is the surface skin temperature, and t_air(i,1,j) is the air temperature at the first model grid cell above the surface, with (i,j) indicating the two horizontal dimensions of each variable and (i,1,j) indicating the first grid cell value above the surface. We note that flhc(i,j) is a function of several other variables (e.g., mol(i,j), ust(i,j), t_air(i,j) and t_surf(i,j)), all of which vary in space and change with each advancement of the model time step.

Our algorithm applies the specified heat flux value spec_hfx indirectly via an assigned value of t_surf(i,j) that is consistent with the spec_hfx value, based on the current values of the other dependent variables, flh(i,j) and t_air(i,1,j). This is accomplished by rearranging equation (1) as:

$$\text{t\_surf(i,j)} = \text{spec\_hfx/flhc(i,j)} + \text{t\_air(i,1,j)}. \qquad (2)$$

Here, the desired value, spec_hfx, replaces the computed value, hfx(i,j). This formulation permits horizontal variability of the applied surface temperature based on the horizontal variability of flhc(i,j) and t_air(i,1,j).

To enable a capability to force simulations using horizontally homogeneous values of the surface temperature, a typical approach in prior idealized LES setups, the above implementation also contains an option (spec_ideal = 2) to first compute domain average values of flhc and t_air, resulting in a constant, horizontally homogeneous value of t_surf. The computation of horizontal averages requires the use of internal WRF message passing subroutines that collect the information from across all processors to compute the global sums (wrf_dm_maxval_real8). This is required in order to compute domain average values of variables when the domain is decomposed across multiple processors. Due to limitations of the standard single-precision accuracy commonly configured when using WRF, the local sums computed on each patch and the patch summation must instead be computed locally using double precision in order to provide the same values over arbitrary domain decompositions (because the sum on each patch varies with patch size). This results in a small increase in memory requirements and run time versus the local approach.

The implementation also enables a user-specified surface temperature tendency (warming or cooling rate) through namelist variable spec_sf_heatrate, in K per minute. That implementation works by computing the domain-averaged value of t_surf the first time the surface temperature tendency option is invoked, after which the tendency is subsequently applied. Due to WRF's above-described use of single-precision accuracy, the tendency must be applied at one-minute (or larger) intervals during execution, because any smaller time increment results in very small values of the tendency (less than 1 K per hour) that fall beneath the threshold for single precision, and hence, they do not affect the temperature evolution.

These above-described capabilities are implemented via a new module that gathers the required information and specifies variables such that the lowest level subroutines, such as phys/module_sf_sfclayrev.F, do not need to be modified at all. This removes the need to also modify multiple argument lists comprising the suite of calls to phys/module_sf_sfclayrev.F, as was required in the previous implementation of some of these procedures during FY 2019.

These new methods are both run-time options that are enabled via entries in the namelist.input file's "dynamics" block. First, the user sets spec_ideal > 0 to use the capabilities. Next, if one desires the surface temperature tendency option, one supplies a nonzero value of spec_sf_heatrate. Otherwise, if spec_sf_heatrate = 0, then the specified value of the surface heat flux, spec_hfx, is applied. Hence, these procedures may be used to specify any value of the surface heat flux, including zero for neutral conditions, and any value of the surface temperature tendency, except zero; however, a zero surface temperature tendency can be practically invoked by using a very small value (e.g, 0.001).

The team also improved a set of Python Jupyter notebook processing scripts developed in FY 2019 to analyze and plot output from the WRF simulations. One of the modifications was to decrease the amount of memory required to read in data prior to analysis by reducing the number of vertical levels selected. This allows the scripts to perform identically across different high-performance computing platforms. An additional modification was to specify spatial limits in the portion of the output domain being processed to avoid incorporating irrelevant data that can skew results. For example, our perturbation analysis setup applies the perturbations only along the x-direction inflow boundary. If the flow is not perfectly aligned in the east-west direction, a portion of the domain along one of the lateral edges will not be influenced by the perturbations.

Incorporating these unperturbed portions of the flow into the histograms of velocity, for example, indicates an enhanced probability of values near zero, which is not due to the perturbation method but to the incorporation of portions of the flow field to which the perturbation were not applied.

One additional feature added to the WRF code is an ability to write instantaneous values of the u, v, and w velocities, as well as temperature, at one user-specified vertical height above the surface for the entire domain. This is implemented via the namelist variable slice_height = x, where x is a height above the surface in meters, to which the output data are interpolated during run time. This provides an ability to examine slices of data at high spatiotemporal resolution without slowing down code execution due to writing full 3D fields or creating large files that are slow to read and or process.

All of the above-mentioned codes and analysis scripts are available on the project GitHub site, with WRF input decks archived at https://github.com/a2e-mmc/WRF-setups/tree/master/sWiFT_20131108_PertMethodsGroup.

5.2 Inflow Perturbation Analysis

One goal for FY 2020 was to examine different inflow perturbation methods over the SWiFT field site under three different stability classes: convective, near-neutral, and stable. This work began in FY 2019, with anticipated completion in FY 2020; however, due in part to reasons discussed above, the work remains ongoing, with planned completion in FY 2021.

The basis of this study is shown in Figure 5.1, which indicates a two-day diurnal cycle occurring November 8–9, 2013, at the SWiFT field site near Lubbock, Texas. Figure 5.1 shows potential temperature, wind speed, TKE, and wind direction at eight of the ten heights across the instrumented tower at the SWiFT facility (the two lowest heights were omitted, because those were nearly indistinguishable with the third lowest height that is shown). The colored shaded bands indicate time periods for which idealized case studies are being constructed, including two near-neutral periods (N1 and N2), two stable periods (S1 and S2), and a convective period (C).

The first case study that the team examined was the convective period (C). The team worked together to define the initial and boundary conditions to force the case study using a series of WRF simulations with varying ranges of geostrophic wind, surface heat fluxes, and surface roughness values that resulted in the best agreement between the simulation and the measured values during a two-hour subset of the period. The best set of forcing parameter values were then distributed back out to the team for forcing the different perturbation methods developed across the participating institutions.

Two different inflow perturbation approaches were examined during the convective case study. The stochastic cell perturbation method (CPM) was applied to potential temperature, horizontal velocity components, vertical velocity components, and both horizontal and vertical velocity components, simultaneously. These perturbations were all applied within online nested WRF simulations; they were applied to the inflow in an LES domain that was nested within a mesoscale domain. An alternative perturbation approach based on the Mann (1998) method was applied to an offline LES using open boundary conditions, with the perturbations also applied at the x-direction inlet to the mesoscale flow specified at the inflow plane. Additional approaches based on the TurbSim stochastic turbulence generator and Gabor kinematic simulation approaches (Quon et al. 2018) were also planned for FY 2020, but they were delayed due to the shift of team resources to execution of the offshore challenge case.

Figure 5.2 shows results using the new WRF code from the MMC GitHub and analysis scripts, along with the setup from FY 2020, for the convective period using no perturbations on the left and the CPM applied to potential temperature on the right. The plots contain several panels that depict different flow information as the flow advects across the domain from left to right, following the mean flow. The top-left panels depict instantaneous cross sections of horizontal wind speed, with the colored vertical lines indicating locations at which various flow quantities are computed along the y-direction. Below those panels are spectra of the horizontal velocity, followed by the vertical velocity, instantaneous cross sections of vertical velocity, followed by skewness and kurtosis. To the right are histograms of the vertical velocity. All results are shown from approximately 100 m above the surface and averaged over four hours of simulation time.

Comparison of the unperturbed (right) versus perturbed (right) flow field indicates that the perturbations significantly accelerate the development of turbulence, with all quantities becoming nearly indistinguishable in time or distance after about the midpoint of the domain, relative to the unperturbed flow parameters, which continue to evolve toward equilibrium values.

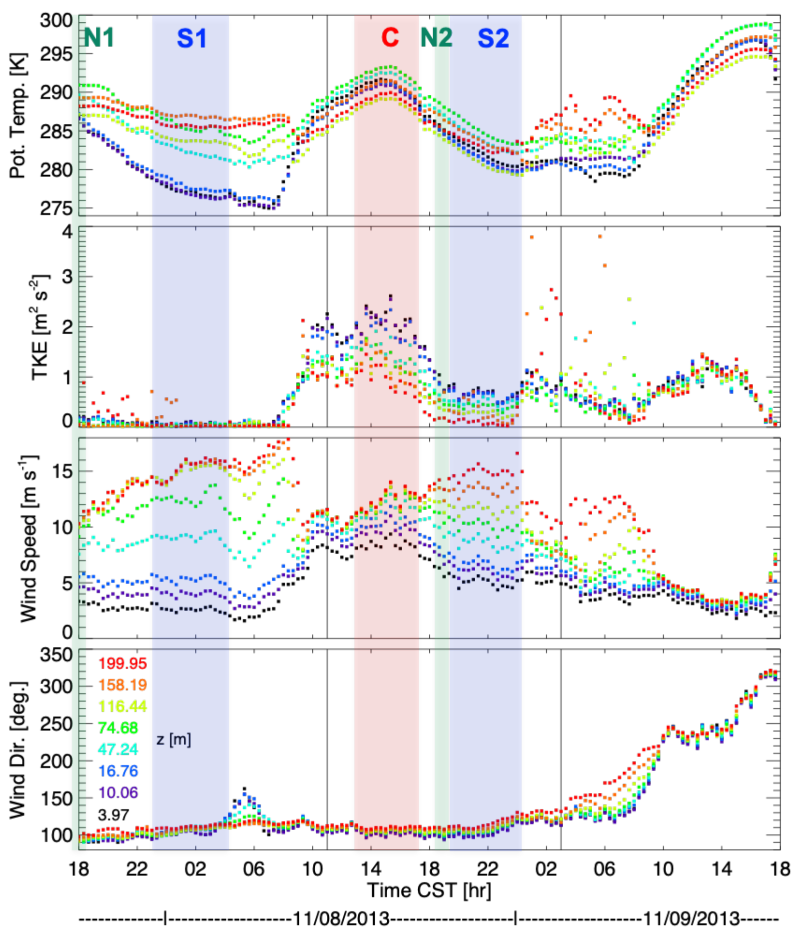

Figure 5.1. Measurements at eight heights on an instrumented tower during a two-day period at the SWiFT site, from which idealized case studies comprising different stability conditions (Neutral N1 and N2; Stable S1 and S2; and convective, C) were constructed to evaluate various inflow perturbation methods.

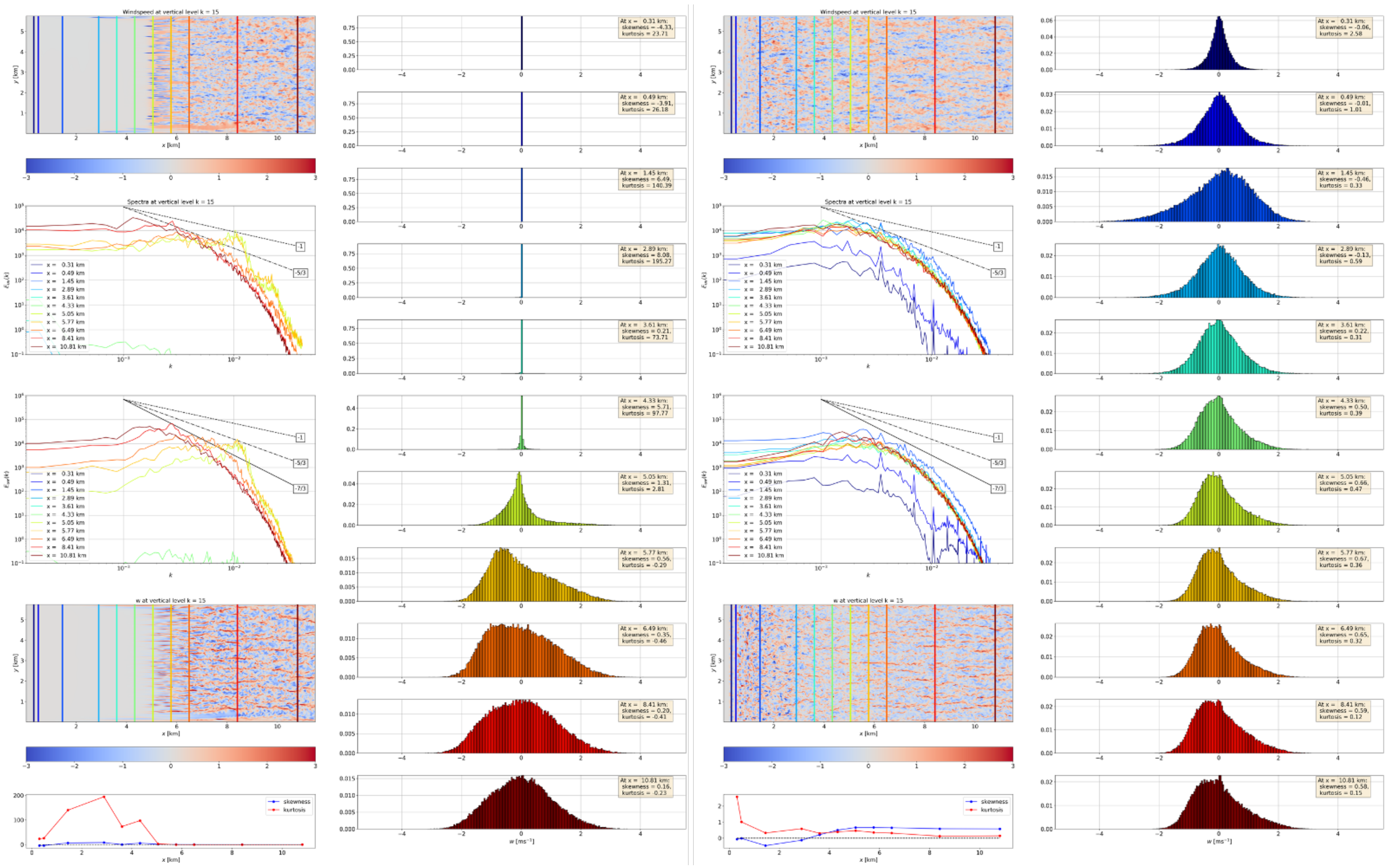

Figure 5.2. Performance metrics from the perturbation simulations during convective conditions. The left set of panels shows data with no perturbations, as a baseline, while those on the right depict the CPM method applied to potential temperature, as described in the text.

Figure 5.3 shows the same analyses from simulations using the CPM applied to the horizontal and vertical velocity components, rather than the temperature, on the left, as well as application of an entirely different approach, based on the Mann (1998) method, on the right. These data show that different perturbation approaches influence the evolution of turbulence differently, although the transients all give way to similar equilibrated behavior approaching the end of the domain. These differences will be further quantified and compared during FY 2021.

The team intended to also examine the above perturbation methods in both near-neutral and stable conditions during the same two-day period from which the convective case study was constructed; however, portions of the observational data from the time period were not archived on the DAP, as was supposed to occur. Further attempts to retrieve the data from the source were complicated by the COVID-19 pandemic, preventing access to the facilities in which the raw data are surmised to exist. This two-day period contains two stable nocturnal boundary layers and several near-neutral conditions during the morning and evening boundary-layer transitions from which case studies could potentially be constructed.

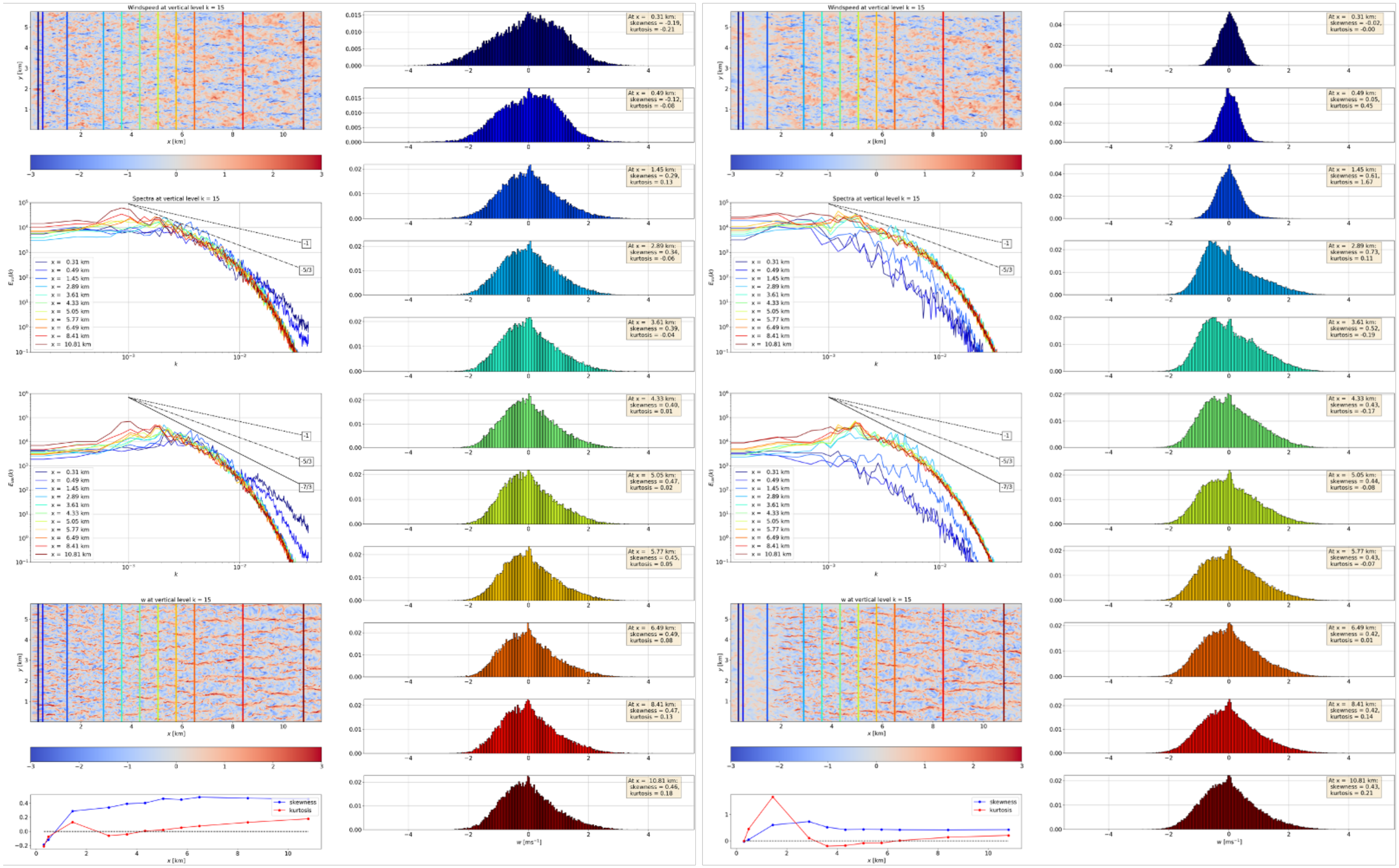

Figure 5.3. Performance metrics from the perturbation simulations during convective conditions, as in Figure 5.2, here with the left set of panels showing data using the CPM method applied to the horizontal and vertical velocities, with those on the right using the Mann method.

Figure 5.4 shows simulation results relative to observations from two potential case studies: the near-neutral period N1 on the left and the stable period S1 on the right. The solid lines show 10-minute average observed values from the tower, while the dashed colored lines show WRF simulation results. The neutral period was simulated for 60 hours to investigate the timescale of damping of the inertial oscillation. While only three observed profiles are shown, the equilibrium WRF simulations match the observations quite well, with the temperature showing the same slope above about 70 m. The different slopes between the simulated and observed profiles below about 70 m are due to the observation period occurring just after the surface began cooling, subsequently cooling a shallow layer of the atmosphere above it. We hypothesize that the observations from the two-hour period prior to the data shown, before the surface began to cool, would provide excellent agreement with the simulated profiles; however, those are among the data that are not available on the DAP. In the event that these data cannot be obtained, alternate time periods will need to be used to construct a near-neutral period for assessment.

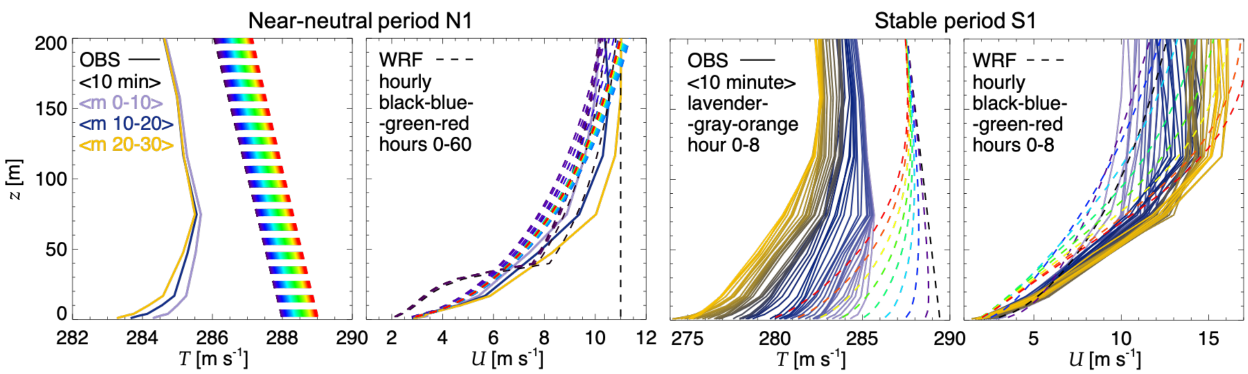

Figure 5.4. Simulated (dashed) and observed (solid) profiles of temperature and wind speed from near-neutral period N1 (left two panels) and stable period S1 (right two panels) showing the potential of these periods to provide additional assessment data of the inflow perturbation methods.

The panels on the right of Figure 5.4 show results comprising a stable case study based on S1. Here, eight hours of observed 10-minute average profiles are shown, indicating stabilization of the temperature profile, as well as acceleration of the winds. The simulated WRF profiles show excellent agreement in the vertical gradients of temperature and wind shear, which are factors that strongly impact the turbulence field. The offset of the simulated relative to the observed temperature is based on the initial condition, and it can be reduced to more closely match the actual observed temperatures. While the wind speed profiles do not capture the very strong observed shear occurring just above the surface, the overall bulk shear from the surface to a height of about 100 m is well captured. While S1 represents a potentially useful stable case study period, the second stable period S2 will also be examined, because it shows higher values of TKE (see Figure 5.1), possibly due to the slower rate of cooling of the surface during the evening transition.

During FY 2021, the team will leverage the work under way to complete this task, further developing the stable case, and either obtaining the missing data for the near-neutral case or selecting a different dataset. The work will culminate in a team publication in a high-impact journal.

6.0 Dealing with Gravity Waves at the Microscale

Atmospheric gravity waves have been found to form within the microscale domain, particularly when the solver is separate from any type of coupling. Typical conditions in which they develop are stable temperature stratification, the presence of complex terrain, or a combination of both. Gravity waves were identified in previous years, and during FY 2020, we investigated them further, assessing the effectiveness of using damping layers to mitigate some of the challenges encountered.

Note that gravity waves are physical phenomena, and their appearance should not be completely removed. We do need to understand, however, how these waves behave in a finite-domain microscale setting. In the previous years, we found that these large-scale waves interact with domain boundaries and are reflected back into the domain. This is especially relevant at the top boundary of the computational domain. These reflections are not physical and should be addressed. In this section, we present some results of the efforts to investigate damping layers to alleviate these issues.

The idea behind damping the undesirable interaction of the gravity waves with domain boundaries is to use either a viscous layer or a Rayleigh damping layer. Although we have implemented both capabilities, viscous damping has shown to require values for viscosity that are not realistic. Rayleigh damping, however, performed better upon initial investigations, and we consider only Rayleigh layers in this work.

The Rayleigh layers function by imposing an additional body force in the momentum equations. The body force is computed as a function of the local velocity and a parameter related to the strength of the damping. Applying such damping in the vertical component of the velocity means that we are imposing a body force that attempts to drive the local vertical velocity to a known value—in this case, zero. In this work, the damping layers are set such that the strength coefficient varies as a cosine within the thickness of the layer region as it approaches a boundary, being maximum at the outer boundary; the maximum damping strength is a user input.

The results so far have been mainly focused on a visual inspection of the flow field to gauge the effectiveness of the damping layer in mitigating the spurious reflections. Preliminary work accomplished in FY 2019 indicated that the position of the layers has a significant effect on the results. In light of this, the design variables considered in this study included the following:

- Position of the layers (top only, inlet and outlet, all four sides)
- Thickness of the layer (3-, 5-, or 7-km thick)
- Relative height of the undamped region for top-located layer
- Strength of the Rayleigh damping
- Bottom surface geometry (simple hill or a real complex terrain case).

6.1 Biglow Canyon Case

To determine how the gravity waves behave in a real complex terrain scenario, we begin by investigating the flow over the Biglow Canyon/WFIP 2 terrain. The case consists of a 30- by 20-km domain (longer in the streamwise direction), with variable height. The Cartesian grid is such that blocks of uniform cell sizes are stacked, resulting in coarser regions toward the upper boundary. The temperature stratification is stable throughout the domain, and wind has a uniform wind speed of 8 m/s aligned with the domain.

Within the domain, the most important boundary is the top because the spurious reflecting waves can modify the flow in a significant way. With that in mind, we first evaluate results based on the test matrix shown in Figure 6.1 using a maximum strength of 0.01 s^{-1}. The figure shows a slice along the 30-km side with the flow going from left to right. The shaded boxes represent the Rayleigh layers. Note that they are set to be above the capping inversion in every case.

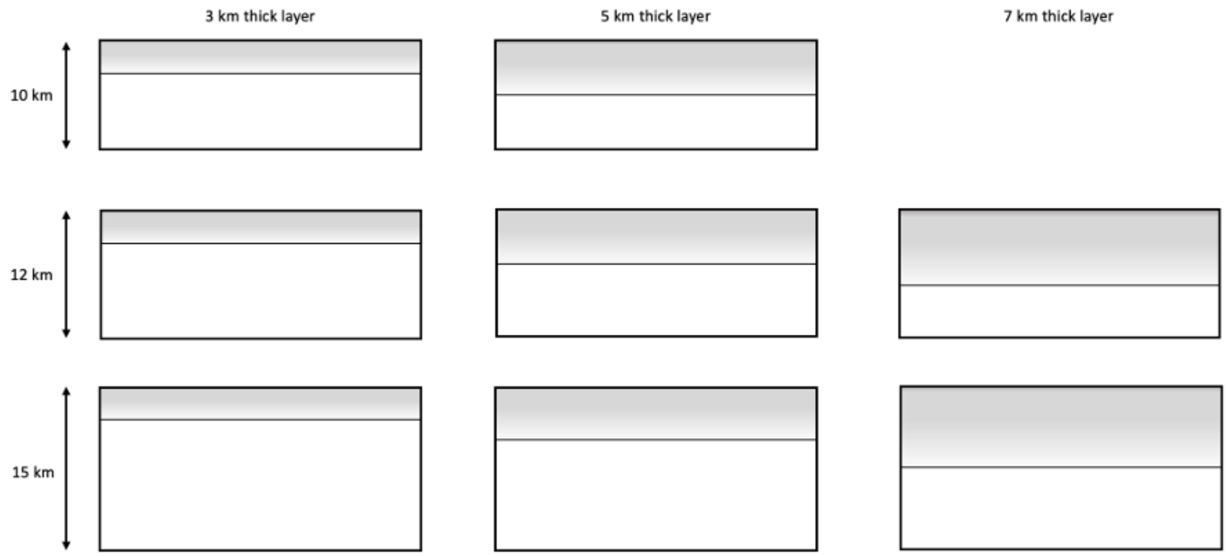

Figure 6.1. Illustration of the initial test matrix for the assessment of the gravity waves dampening over the Biglow Canyon. The shaded layer on the top represents the damping layer imposed, with the gradient representing the cosine distribution of the effective strength of the damping region.

An instantaneous snapshot of the results is shown in Figure 6.2. All eight cases developed gravity waves, and each broke down into strong turbulence levels after 20,000 seconds. From the snapshot shown, it appears that the shorter the undamped region is, the longer it takes for the gravity waves to develop. It is important to note that these are not standing waves but rather complex propagating waves. No indication of a steady-state solution was observed in the 30,000 seconds of simulation time.

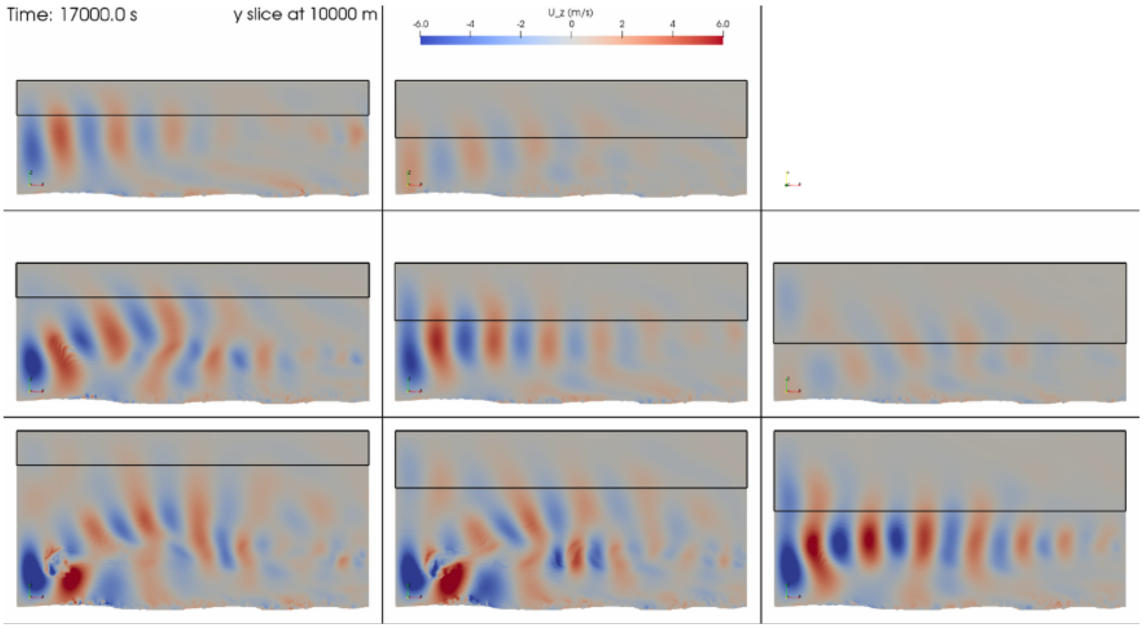

Figure 6.2. Instantaneous snapshot of flow field after 17,000 seconds. The grid is arranged following Figure 6.1. The black box is a visual indication of the location of the layers.

From Figure 6.1 and Figure 6.2, we conclude that a 12-km-high domain seems appropriate to investigate further, because it represents a realistic simulation domain size while being able to accommodate different thicknesses of Rayleigh layers. We also down-selected 3- and 5-km thick layers for further investigation. The 7-km thick layer was excluded, because it represents a significant part of the domain and, thus, a non-negligible added computational cost. The thickness of the layer needs to be adjusted according to the strength of the damping, because a thinner-but-stronger damping layer may provide similar results at lower cost than a thicker-but-weaker one.

Next, we investigate cases that contain damping layers on the sides of the domain in addition to the top boundary (see illustration in Figure 6.3).

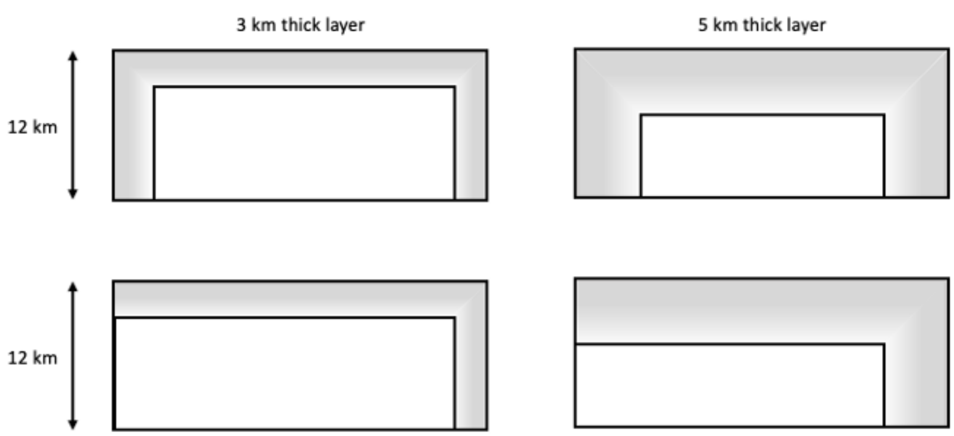

Figure 6.3. Illustration of the test matrix for the scenarios that contain Rayleigh layers on the side boundaries as well as on the top boundary.

Analyzing the results (not shown) of the scenarios illustrated in Figure 6.3, with the same flow direction from left to right, it becomes obvious that a damping present only on the outlet is not effective. For the Biglow Canyon scenario, the gravity waves appear to develop and propagate from the inlet side of the domain; therefore, we focus on the case with layers on all sides and top. Figure 6.4 depicts the resulting flow field of a simulation with the settings that worked best for the realistic Biglow Canyon case. Rayleigh damping layers that are 3-km thick are present on all sides, as well as the top boundary. Gravity waves develop but do not reflect off boundaries or break down into turbulence. The scenario was executed for 30,000 seconds, and the damping layers were effective in suppressing unphysical disturbances from the reflection of the waves. Figure 6.4 displays a top view of the terrain, where the Columbia River Gorge, near the actual Biglow Canyon, can be seen clearly. We note that the 5-km-thick layers showed similar behavior; however, their thickness resulted in a significant part of the domain being dedicated to the damping layer, ultimately resulting in a large computational effort to resolve the flow field of a region that is not useful for analysis.

While the solution is visually acceptable, it is difficult to quantify how effective the damping layers really are and what the actual gravity waves over that region look like; thus, we choose to take a step backward and analyze the witch of Agnesi hill geometry, which is a simple bump for which an analytical solution is available. Its simplicity allows more rapid investigation.

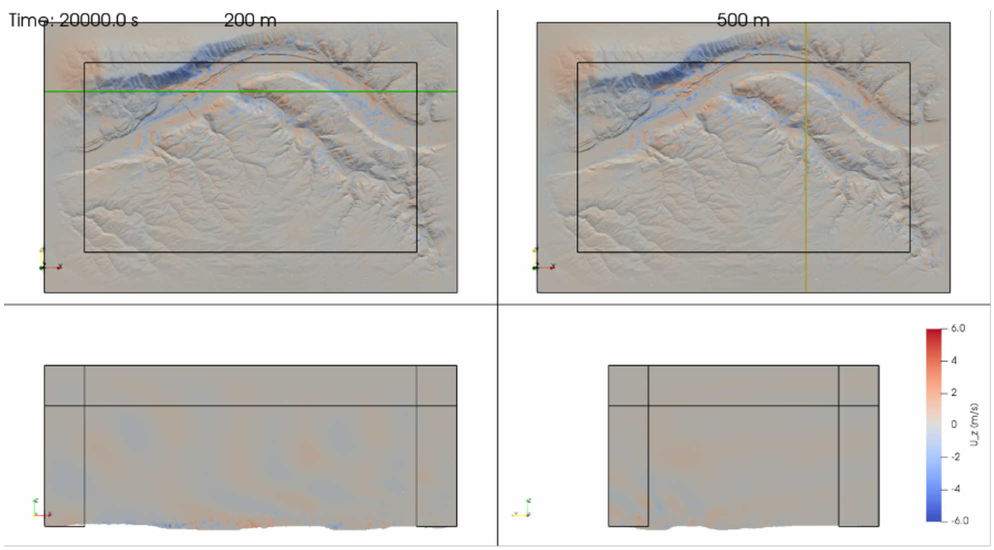

Figure 6.4. Instantaneous flow field present at the Biglow Canyon case with Rayleigh layers on all sides and top (indicated by the black boxes). The upper part of the figure shows a horizontal slice at two different heights, and the bottom part shows the cross section at the location indicated by green/yellow marks.

6.2 Witch of Agnesi Hill

For the witch of Agnesi cases, we maintain the settings largely the same as discussed above, with the exception of the mean wind speed. Now, a uniform velocity of 10 m/s is used. We vary the strength of the damping coefficient, investigating both 0.005 and 0.01 s^{-1}. The lower value has been used in previous studies. Upon experimenting with the strength coefficient, we found that the larger value worked better than the smaller one. The gravity waves observed in this case are stronger than those present in the previous Biglow scenario. The results at different times, as well as the analytical solution for this case, are shown in Figure 6.5. Note that the solution reaches a steady-state solution, as indicated by the last two times shown.

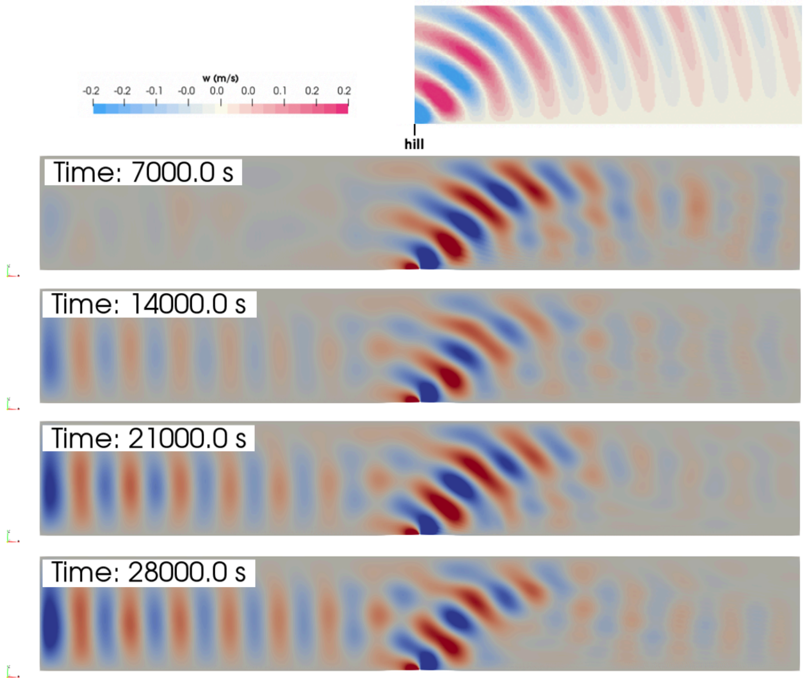

Figure 6.5. Gravity wave development over the witch of Agnesi hill geometry. The bump is in the center of a 100-km-long domain. An analytical solution is shown at the top.

The flow field as presented at the instant 28,000 seconds is reached more quickly if the damping coefficient is lower. In that case, an interaction of reflected waves also occurs. It is suggested that a stronger coefficient may keep the steady-state flow field closer to the analytical solution. The final solution appears to be very sensitive to the strength of the damping coefficient.

With this better understanding of what appears to work, we plan to further investigate and quantify the effectiveness of these Rayleigh layers. A sweep of damping coefficient strength and a quantification of the vertical flux of energy are the next steps to be taken.

6.3 Vertical Filter on the Damping Layers and Moving Forward

In the results presented above, the damping layers present on the side of the domain are active throughout its height (see Figure 6.3). The test cases had a constant-velocity profile, which is not realistic. When coupling by means of any of the several different methods, it is not desirable to dampen the incoming turbulent inflow. To circumvent the issue of inflow turbulence dampening, we impose a filter on the side layers. The filter acts much like one damping layer within another. Simply put, the user can specify the height at which the dampening begins. This approach effectively removes any damping up to a specified height.

We are currently assessing the effectiveness of the damping layer approach with the vertical filter, including making use of the developed MMC coupling strategies, which represents the work of this team.

7.0 Modeling of Atmospheric Conditions During a Wind Turbine Wake Steering Field Campaign

The wake steering field campaign at Peetz Table Wind Energy Center in northeastern Colorado provided an excellent opportunity to apply and evaluate our current MMC capabilities. Our objective, given meteorological mast and lidar measurements of the instantaneous atmospheric state, is to reproduce the corresponding unsteady 3D flow field with fully resolved turbulence from LES. This flow field would then provide a realistic inflow under nonstationary conditions for high- and mid-fidelity simulations.

Under the DOE Wake Dynamics project, a nine-hour study period on December 26, 2019, was selected for in-depth investigation. Down-selection criteria included flow being from the north over mildly varying terrain, conditions being amenable to wake steering, and availability of loads measurements. The periods of interest begin at 12:48 a.m. local time and continue until 9:18 a.m. For the purposes of this study, we focus on the periods before sunrise during which stable atmospheric conditions—corresponding to higher wake persistence—are expected to clearly highlight the impact of wake steering.

7.1 Approach

7.1.1 MMC with Mesoscale Model Forcing

Our approach is to use the microscale profile assimilation (Allaerts et al. 2020) implemented in the SOWFA LES solver. This MMC technique was originally developed and validated for simulation with SOWFA using mesoscale forcing from the WRF model. In this approach, the SOWFA microscale domain is fully enclosed within the WRF domain; therefore, every height level simulated by SOWFA corresponds to a level in the WRF mesoscale solution. As such, initial and boundary conditions are fully defined by WRF.

Initially, we performed an ensemble of WRF simulations for a variety of reanalysis datasets (Global Forecast System, ERA5, and MERRA2), simulation initialization times (8, 14, and 20 hours prior to the periods of interest), and in some cases the PBL scheme (MYNN2.5, MYNN3, and YSU). These resulted in 15 different mesoscale model realizations that generally failed to capture the hub-height wind speed trends observed by the profiling lidar at Peetz (Figure 7.1). The mesoscale skill can also be illustrated by a Taylor diagram (Figure 7.2), which indicates that the wind speed variability is not captured; moreover, the 2-m air temperature trends are not predicted, as indicated by the negative correlation for some mesoscale model realizations. The model deficiencies may be attributed to one or more of the following: 1) a dominant mesoscale phenomenon that is not captured, 2) inadequate grid resolution (3-km spacing), and 3) the impact of terrain (turbines and instruments were located atop an escarpment).

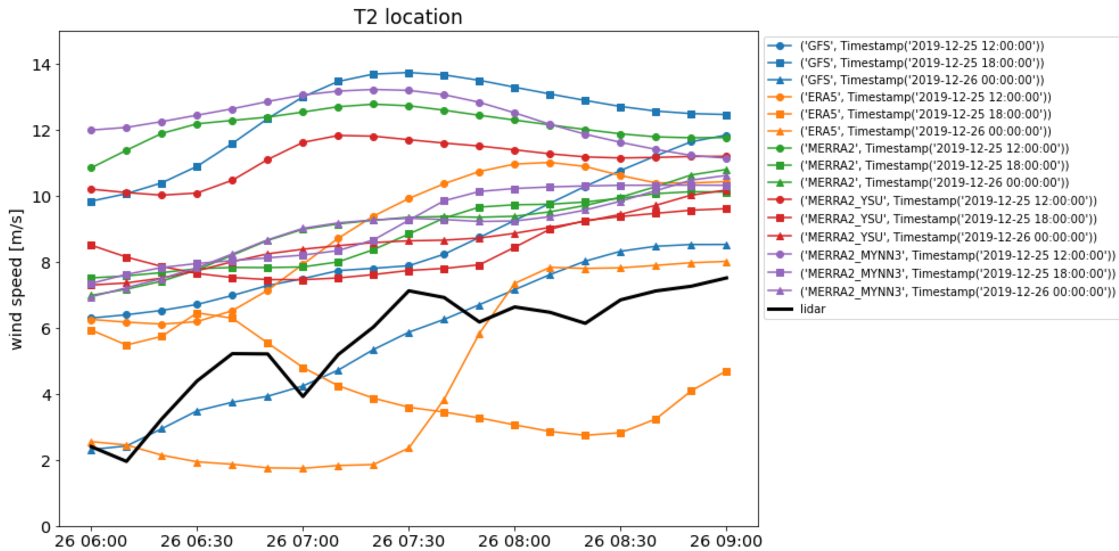

Figure 7.1. Mesoscale hub-height winds predicted by various initial and boundary conditions in comparison with lidar measurement.

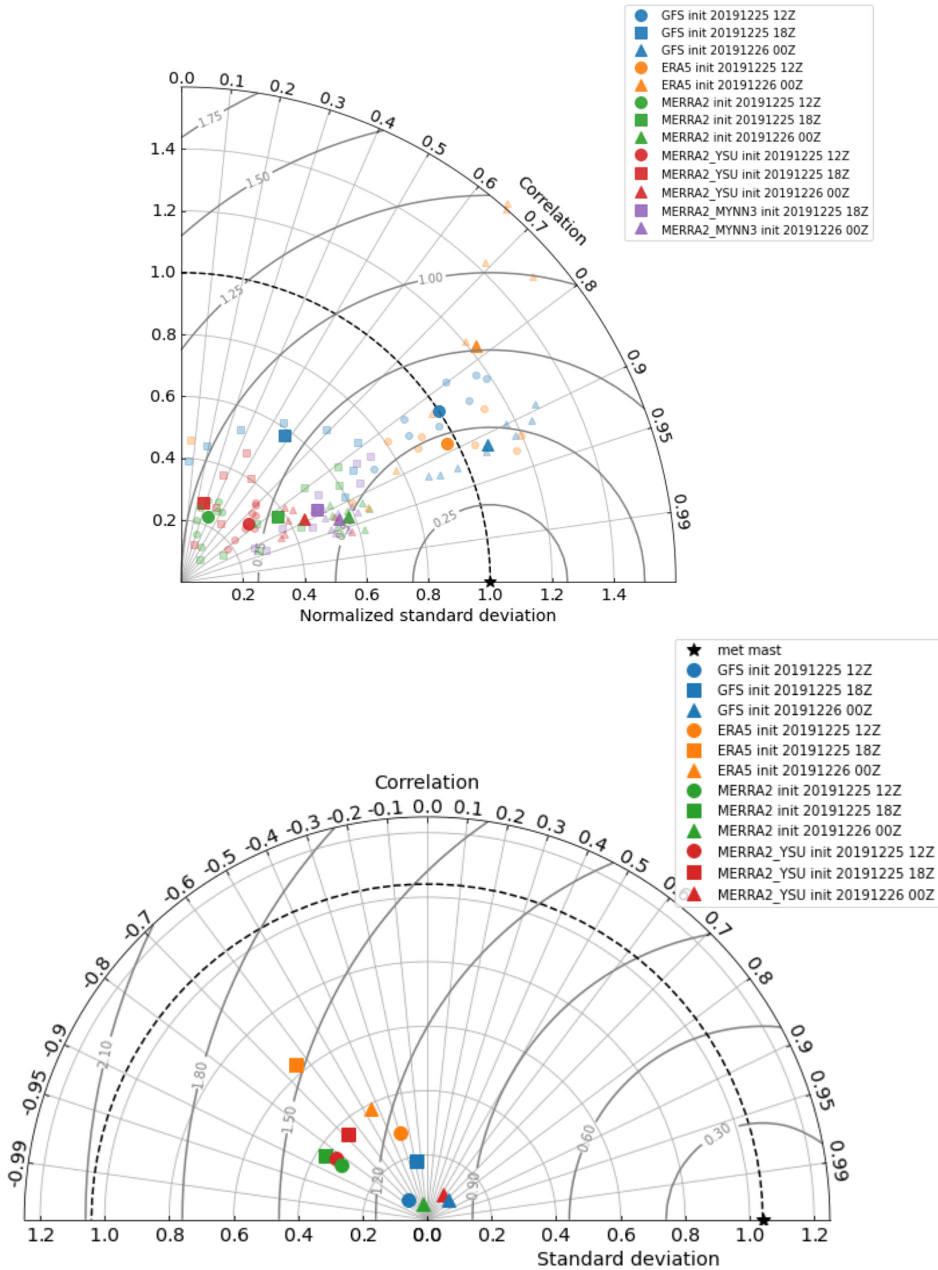

Figure 7.2. Taylor diagrams for hub-height wind speed (top panel) and near-surface (2-m) air temperature (bottom panel).

Evaluating the surface analyses from NOAA's Weather Prediction Center shows the presence of a stationary front at the start of the simulated day (Figure 7.3) and during the period of interest after the following midnight (Figure 7.4). Such a mesoscale weather feature in the vicinity of the region of interest is likely to induce localized velocity and temperature fluctuations due to the interactions between the warm and cold air masses—these will be difficult to capture with WRF at the spatial scales typically modeled (approximately 3 km) to support a coupled microscale simulation.

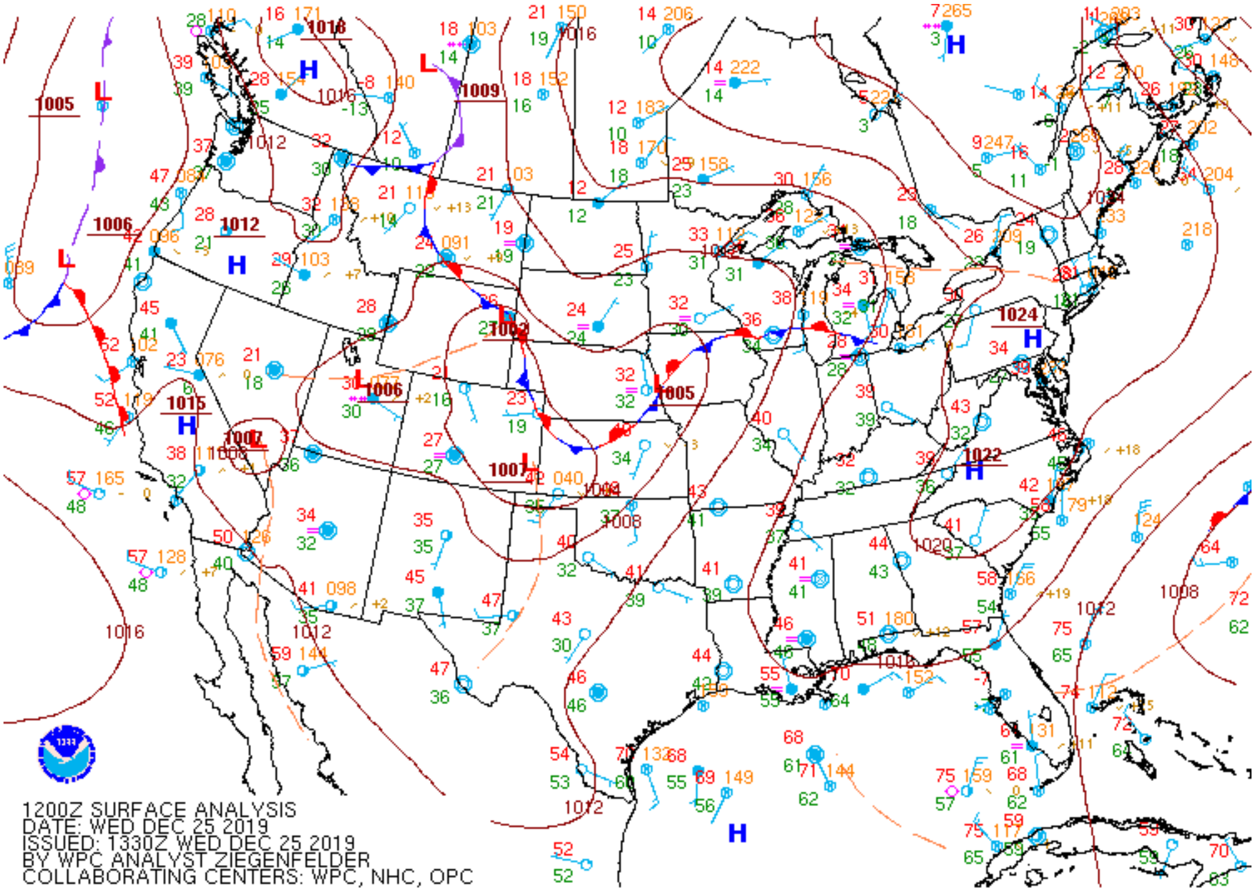

Figure 7.3. NOAA surface analysis at the simulation start (December 25, 2019, 5 a.m. local time).

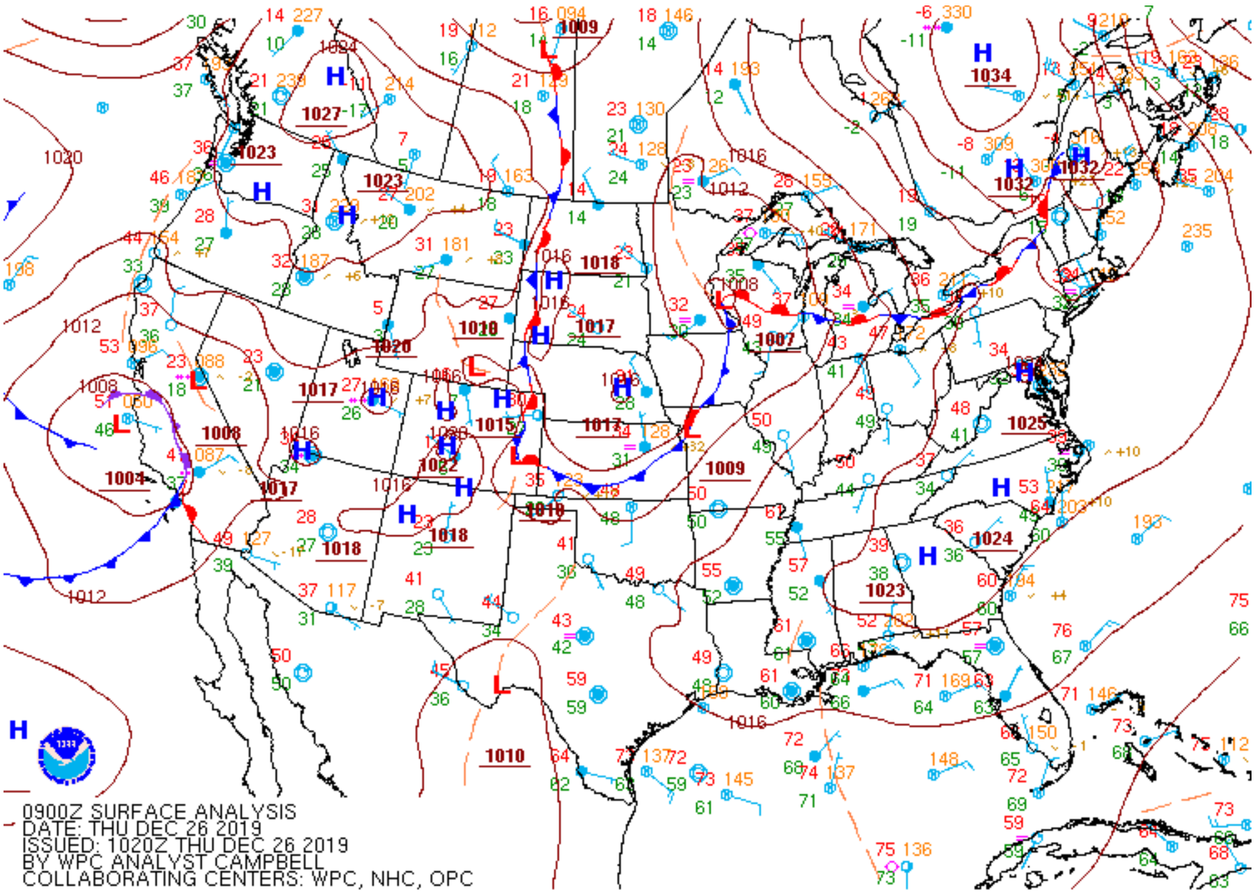

Figure 7.4. NOAA surface analysis during the period of interest (December 26, 2019, 2 a.m. local time).

7.1.2 MMC with Observational Forcing

We instead turn to the measurements provided by a 60-m meteorological mast and a ground-based profiling lidar. These instruments were complementary, with two sonic anemometers and a cup anemometer providing high-frequency point measurements of the wind field near the ground and the lidar providing wind and turbulence information up to 180-m AGL. Due to sampling limitations of the lidar technology, the lidar-measured turbulence intensity had to be corrected by comparison with the cup anemometer velocity spectra.

The SOWFA microscale simulation used doubly periodic lateral boundaries, assuming flat terrain around Peetz Table. The influence of mesoscale weather was included by assimilating known velocity and temperature histories at a single reference height or at all simulated height levels. Assimilating time histories at a single height corresponds to a time-varying body force that is uniform with height. Assimilating time-varying profiles corresponds to time- and height-varying body forces that either directly or indirectly enforce the desired instantaneous profile (Allaerts et al. 2020). In addition to evaluating the different forcing techniques (discussed in Section 7.2.3), we also considered two lower surface boundary conditions: specified heat flux and specified temperature.

The assimilated wind speed and direction profiles were reconstructed from limited field measurements. Missing wind speed data from lidar were infilled using a power-law fit at 10-min intervals. At times, when a reasonable fit was not achieved, cubic spline interpolation was applied in the height dimension. If data were not available, then linear interpolation was performed in time. The wind direction profiles were infilled at each time in a similar manner with splines or linear interpolation. Last, zero-order extrapolation was used to fill in the remaining simulating heights.

7.2 Results

All results have been calculated from planar-averaged quantities.

7.2.1 Sensitivity to Initial Conditions

Exact initial conditions are not known for the beginning of the study period. In order to have measurements of the temperature profile through the depth of the ABL, a radiosonde or radio acoustic sounding system would have to be deployed. Preliminary simulations with coarse resolution (20-m grid spacing) indicated different sensitivities to initial and boundary conditions at different times of day (Figure 7.5). All simulations applied the indirect profile assimilation method of Allaerts et al. 2020. During the daytime, assuming a shallow boundary layer (250-m depth) with a strong versus weak capping inversion at the start of the simulation (with or without a 5-K/100-m layer below a stable layer with 3-K/km lapse rate), in conjunction with specified surface temperature versus heat flux boundary conditions, yields four very different realizations of turbulence. In the evening, however, the differences between the initial and boundary conditions are much less pronounced, and the data assimilation strategy becomes more important.

Subsequent studies used temperature data from a radiosonde launched from Rapid City, South Dakota, shortly before the simulation start time, at 5 a.m. local time. Even though the launch site is more than 300 km away, it is upwind of the test site and provides, in the absence of other data, a reasonable estimate of the capping inversion height and strength. Pressure data from the soundings were used to estimate scale height and, thus, instantaneous pressure profiles from field measurements of surface pressure, which enabled temperature to potential temperature conversion.

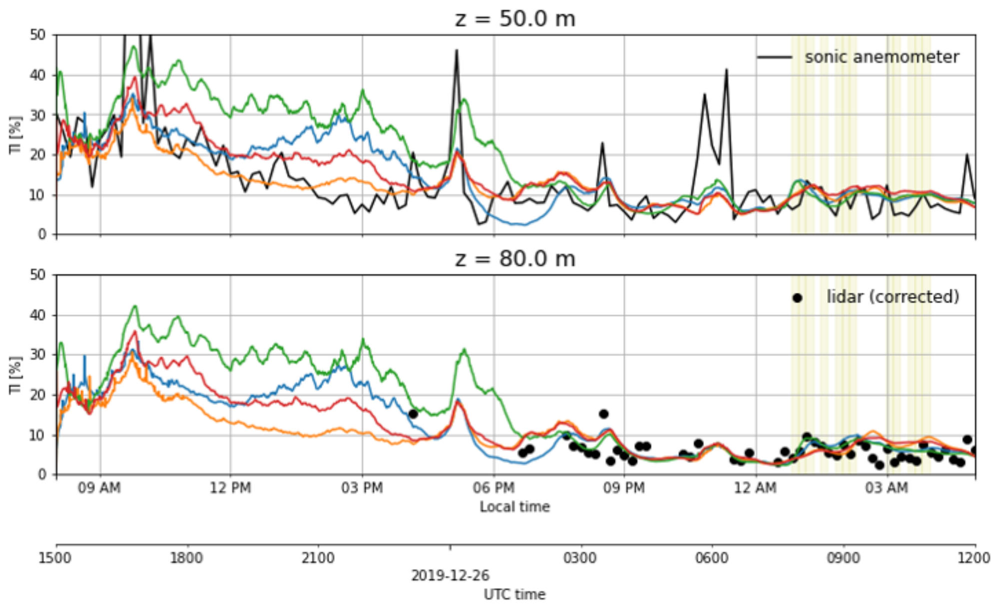

Figure 7.5. Simulated turbulence intensity for initial coarse-resolution simulations compared to two different instruments at different heights; initial/boundary conditions include: specified surface temperature with a strong (blue) or weak (green) inversion and specified heat flux with a strong (orange) or weak (red) inversion.

7.2.2 Temperature Advection

Preliminary simulations of the ABL from early morning through early evening showed that neither the specified heat flux nor specified surface temperature boundary conditions were able to reproduce the observed temperature evolution at 2 m and 59 m AGL (see dashed blue curve in Figure 7.6). This supports the observation of a stationary front in the vicinity of the test site. Considering the magnitude of the difference between the simulation and the observation, the temperature change is likely attributable to large-scale advection induced by frontal dynamics. Additional evidence is the rapid cooling at 3 p.m. local time, which would be unlikely to occur without external forcing.

This temperature advection may be accounted for by applying single-level assimilation, as with the daytime winds. A profile assimilation approach was not taken because the available temperature profile data is even more limited than the wind data. The choice remains to assimilate the temperature at either 2 m or 59 m; the higher height was used to avoid possible adverse interactions with the surface forcing. As seen in Figure 7.6, the temperature history at 59 m is recovered exactly in all cases, independent of the wind assimilation strategy. During the daytime, the applied surface forcing (based on measured kinematic heat flux from the meteorological mast) is compatible with the specified temperature advection, seen in the excellent agreement in the 2-m temperature history between 9 a.m. and 9 p.m. local time.

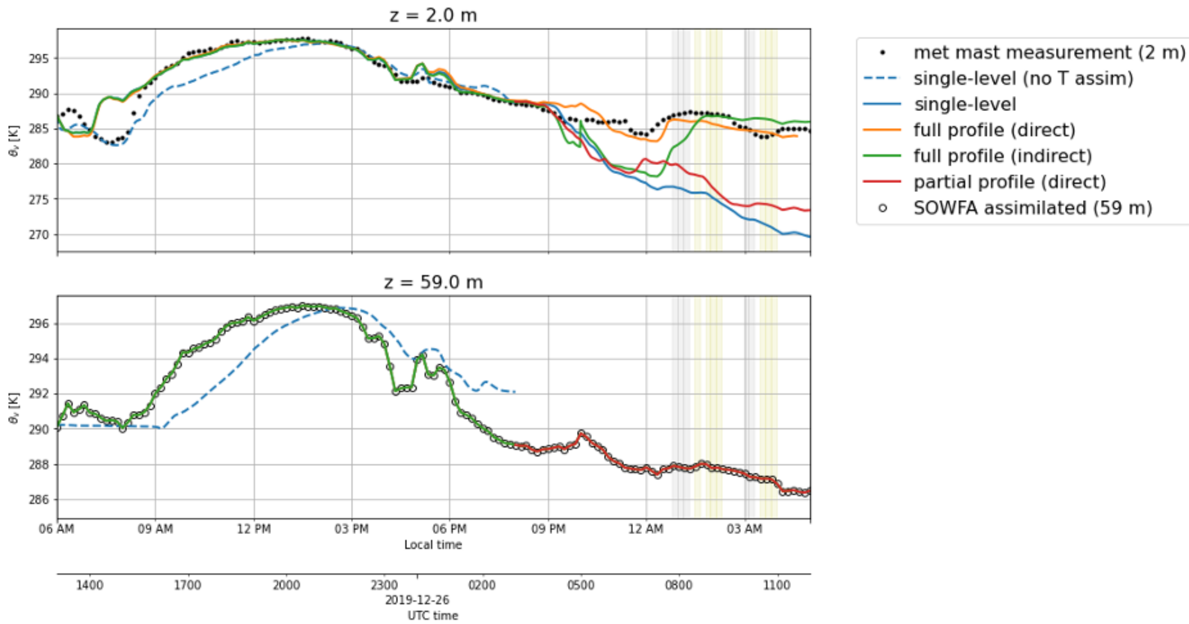

Figure 7.6. Evolution of temperature at two heights above the ground; unless stated otherwise, simulations used single-point temperature assimilation ("assim") at 59-m AGL.

7.2.3 Different Wind Assimilation Techniques

Subsequent simulations used 10-m grid spacing. Four different assimilation approaches were evaluated to calculate the microscale momentum source terms in SOWFA that represent the mesoscale pressure gradient force and large-scale advection:

1. **Single-level**: The time history at a single reference height is used to calculate a time-varying source term that is uniform with height.
2. **Direct profile assimilation**: Time-varying profiles that span the full height of the computational domain are used to calculate time- and height-varying source terms that produce the exact reference profile at each time.
3. **Indirect profile assimilation**: The same approach as direct profile assimilation, except that a polynomial regression is performed at each time to produce a forcing profile that varies smoothly with height.
   - If using WRF as an inflow provider, full profiles—compatible with under-resolved turbulence fields—are available; in this case, cubic polynomials are recommended (Allaerts et al. 2020) to allow for deviation from the reference mesoscale profiles due to the resolution of additional turbulence and to mitigate problems with excessive turbulence generation when applying the direct approach.
   - In this case, the full profiles are not known, and the uncertainties introduced when reconstructing wind time-height profiles from limited data can be exacerbated by a cubic polynomial; to stabilize the solution, a linear regression was used.
   - During the nighttime period, the regression was weighted to favor the portions of the profiles corresponding to actual measurements; however, this creates the possibility of the forcing profile running away at higher levels and merits further investigation.

4. **Partial-profile assimilation**: This approach combines the direct profile assimilation technique with a uniform forcing approach; direct assimilation is applied up to the height of the highest available input data—above this height, the forcing profile is blended to a constant value with height.

Figure 7.7 shows representative wind speed, direction, and temperature profiles at 1 p.m. local time, five hours after the simulation starts. At this time, the ABL is unstable and well mixed. As a result, there is very low wind shear (except near the ground). The direct profile assimilation results are constant with the height above the highest measurement value, with interpolation artifacts visible. The indirect profile assimilation results in smooth profiles but with the possibility of the wind speed and/or direction being unbounded with increasing height; therefore, the single-level assimilation is taken to be the most accurate. This conclusion is also reflected in the time histories of the turbulence quantities, which will be discussed in Section 7.3.

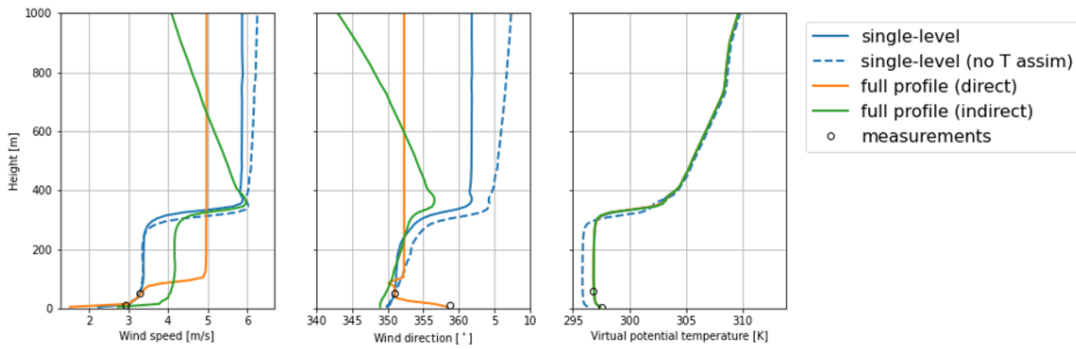

Figure 7.7. Example daytime convective boundary-layer profiles at 1 p.m. local time (seven hours after simulation start) for various assimilation techniques.

Figure 7.8 shows the same quantities as Figure 7.7 but at 1 a.m. local time during the study period under stable conditions. The partial profile assimilation result was restarted from the single-level assimilation case at 9 p.m. local time, prior to a shear instability occurring and the temperature histories differentiating for the different approaches—this will be discussed in the following sections. The indirect method produces wind profiles with inflection points that do not appear to be realistic. In contrast, the partial-profile approach exactly recovers all input measurements near the ground and approaches the uniform forcing result aloft; however, there is no way to validate either the jet-nose profile or the direct profile that assumes a constant wind speed with height.

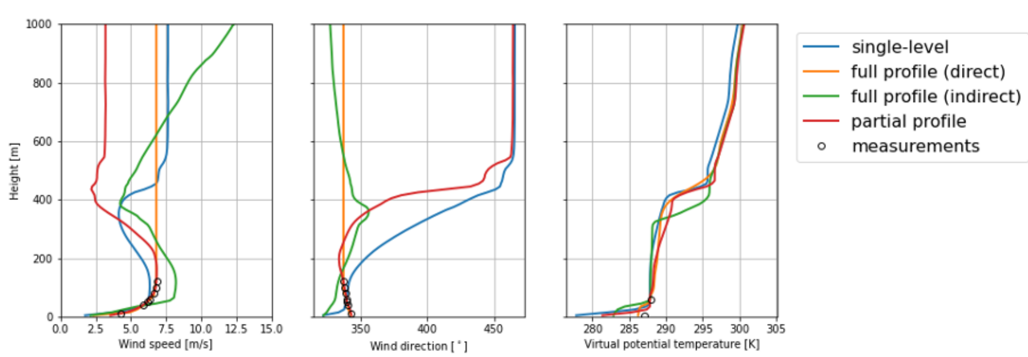

Figure 7.8. Example nighttime stable boundary-layer profiles, at 1 a.m. local time during period of interest, for various assimilation technique.

Relevant mean wind and turbulence quantities of interest are shown in Figure 7.9. The mean assimilated wind quantities closely match the experiment, as provided by the assimilation technique. A known shortcoming of the direct profile assimilation approach has been confirmed: under daytime convective conditions, the direct approach can lead to excessive turbulence generation (as shown by the turbulence intensity and friction velocity plots). Additional features of interest are the turbulence bursts attributed to internal shear instability around 8 p.m. and 11 p.m. local time. Turbulence intermittency is a characteristic of stable boundary layers, may be localized or larger than the integral length scale, and may be caused by a variety of mechanisms (Mahrt 2014).

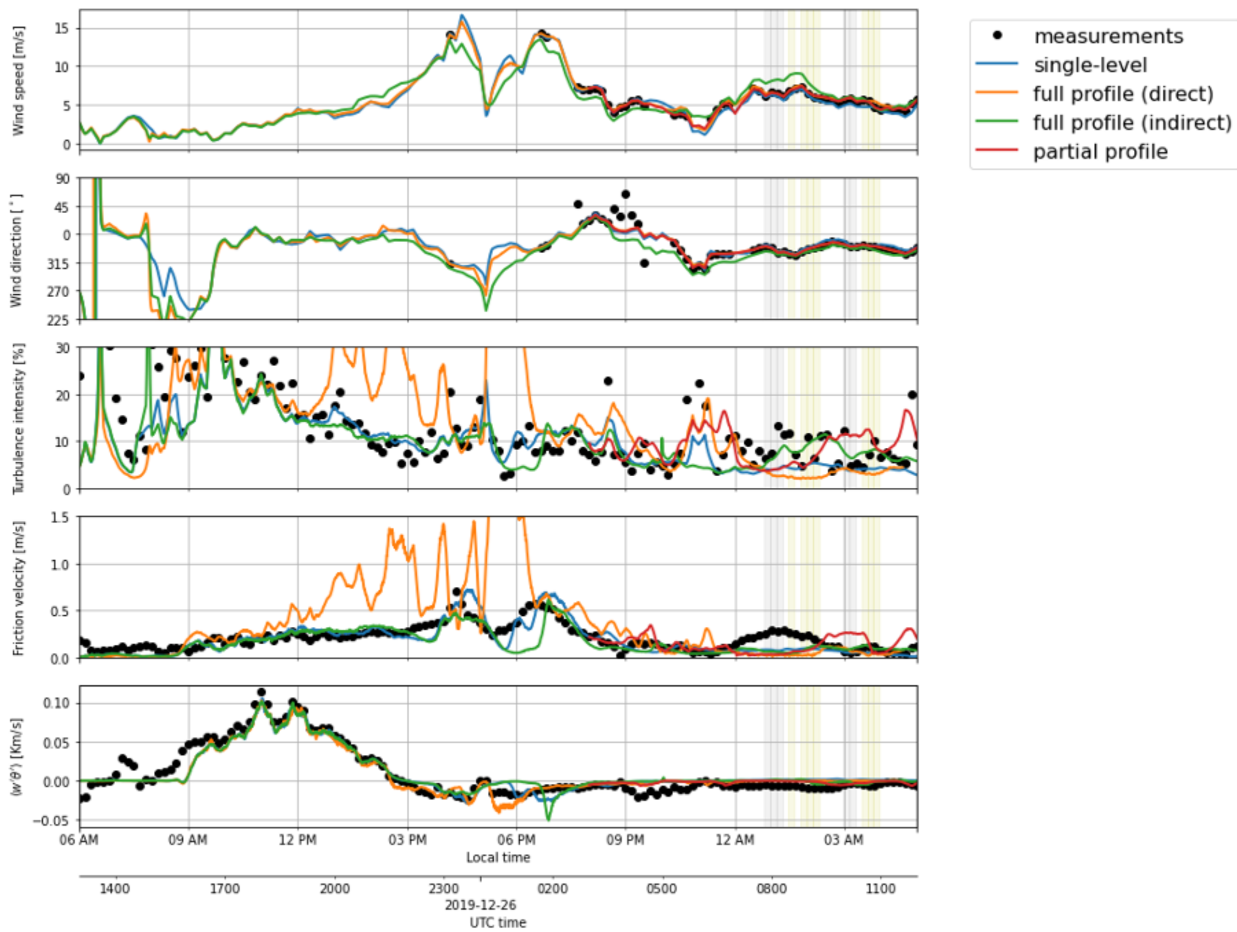

Figure 7.9. Comparison of selected MMC techniques with available measured quantities: hub-height wind speed and direction, turbulence intensity at 50 m, friction velocity at 10 m, and kinematic heat flux at 10 m; note that the partial profile assimilation simulation was restarted from the single-level case at 8 p.m.

7.3 Discussion

We have demonstrated the effectiveness of a number of techniques from our MMC simulation toolbox. From the numerical investigations conducted in FY 2020, we have learned the following about our assimilation capabilities:

- All approaches reliably reproduce the measured hub-height winds for the duration of the simulation.

- The combination of specified surface heating for all periods of the diurnal cycle, combined with temperature assimilation, was an effective approach to incorporating the effects of mesoscale temperature advection.
- A shortcoming of all profile assimilation approaches is that knowledge of the full profile spanning the entire simulation domain is required; an alternative is a new partial profile assimilation technique. The partial approach is a blend between direct assimilation at lower height levels—where field data are available—and the uniform background forcing that would result from a single-level approach.
- Given the uncertainties in the profile-based approaches when using limited observational data, the single-level approach appears appropriate for use under daytime, well-mixed conditions, and it can produce more realistic profiles than a direct or indirect approach.
- The indirect approach appears to be applicable during all periods of a diurnal cycle, but the presence of a shear instability poses a significant challenge due to the extreme sensitivity to wind shear. In this case, reproducing the exact measured profile, especially near the ground, appears to be critical for capturing the observed elevated turbulence.
- The partial approach produces the most realistic results for the shear instability and ensuing nearly neutral ABL, despite some error in both the maximum turbulence intensity following the turbulence burst and the timing of the intermittent turbulence that followed.

The simulations performed here will provide a good foundation for turbine simulations and a load validation study. Current follow-on research focuses on understanding the physical processes that initiate, drive, and result from the shear instability. These have been difficult to capture, with sensitivities to the quality of the forcing data and chosen assimilation strategy. In the time periods before and after the turbulence burst, the measured winds were characterized by near-surface wind direction changes, from veering to backing. Because these variations are observed only near the ground (less than 50 m AGL), this suggests the possibility of a shallow air mass advecting through the region and, in the process, inducing turbulent motions in the resident air mass (inducing and/or sustaining the observed intermittency). In addition, some of the near-surface velocity and temperature fluctuations that have been observed may result from downwind drainage flow, which would require modeling of the actual terrain.

8.0 Uncertainty Quantification of Large-Eddy Simulations in Complex Terrain

A number of factors contribute to the uncertainty of high-fidelity modeling of atmospheric flows for wind energy applications. These factors include uncertainty in the specification of boundary and initial conditions, uncertainty in model parameterizations or closures, and (for mesoscale-to-microscale coupled simulations) uncertainties introduced by the coupling techniques themselves. Assessment of this uncertainty is challenging, in part because many of these sources of uncertainty are structural in nature and less amenable to conventional uncertainty quantification techniques; however, parametric uncertainties, associated with uncertain parameter values within model closures, are also important because both mesoscale models and LES models of microscale turbulence require parameterizations to represent unresolved scales of turbulent motions, surface layer interactions, and other physical processes. Conceptually, at least, these parametric uncertainties are more tractable for analysis, and a number of approaches and tools exist for this purpose.

Ideally, uncertainties propagating from both mesoscale and microscale modeling components should be taken into account when attempting to quantify the overall uncertainty in mesoscale-to-microscale coupled simulations; however, due to the large number of parameters plus the relatively high computational cost of LES, it is more feasible to employ a tiered strategy to assessing the uncertainty of coupled simulations by first identifying the most critical parameters in each of the mesoscale and LES closures before attempting a combined analysis. There has been significant progress made in examining parameter sensitivities within mesoscale simulations. For example, using WRF in a mesoscale configuration to simulate wintertime conditions in the Columbia Basin region, Yang et al. (2017) analyzed the sensitivity of predicted turbine-height wind speeds to 12 parameters of the MYNN PBL scheme and 14 parameters of the MM5 surface-layer scheme. Promisingly, this study found that most of the uncertainty in predicted wind speeds was attributable to just a few of the parameters in each of the boundary- and surface-layer schemes. Berg et al. (2019) confirmed this finding for springtime conditions, while Yang et al. (2019) showed that the sensitivity of WRF's YSU PBL scheme is also largely attributable to just a few parameters.

Here, using nested WRF/WRF-LES simulations, we evaluate the sensitivity of predicted boundary-layer winds and turbulence to parameters of a 1.5-order, TKE-based SGS turbulence closure, plus the surface roughness. We sample a range of parameter values to generate an ensemble of mesoscale-to-microscale coupled model runs using a nested WRF/WRF-LES computational approach. This perturbed parameter ensemble (PPE) of WRF/WRF-LES model runs is then used to determine which LES closure parameters most strongly influence predictions of hub-height winds and turbulence.

8.1 Parameter Identification for an LES Turbulence Closure

Although a few SGS turbulence closures are available in WRF-LES, we opted to study the 1.5-order TKE-based closure that largely follows the model presented by Deardorff (1980), because similar types of closures are implemented in many atmospheric LES models. For clarity of the following discussion, we present some of its key relations below.

The Deardorff TKE-based closure relies on the commonplace assumption that SGS turbulent stresses are proportional to resolved scale strains, in analogy to viscous stresses, but with molecular viscosity replaced by an eddy viscosity. In particular, eddy viscosity, K_m, is determined (at each LES grid point) from the SGS TKE, $e=\overline{u_i'u_i'}$ and an eddy-length scale in the form $K_m = c_k e^{1/2} l$. The eddy-length scale, l, equals the grid-based filter scale, Δ, when (grid-scale) stratification is neutral or unstable and is reduced under stable stratification according to $l= c_n e^{1/2} N^{-1/2}$, where N is the Brunt- Väisälä frequency. The ratio $l\Delta^{-1}$ is used in the closure as a measure of the local level of flow stability.

The SGS TKE itself is determined by solving a prognostic equation that includes terms for resolved and SGS transport, production of TKE by resolved shear, production/destruction of TKE through buoyancy, and viscous dissipation of e, denoted by ϵ. The closure for dissipation is $\epsilon = c_\epsilon e^{3/2} l^{-1}$, and the coefficient c_ϵ is modified in response to local stability according to $c_\epsilon = (c_{\epsilon N} - c_{\epsilon S}) l\Delta^{-1} + c_{\epsilon S}$, where subscripts N and S refer to neutral and stable stratification, respectively. The coefficient $c_{\epsilon S}$ is difficult to directly constrain through physical arguments; however, the coefficients of the closure can be related to a critical Richardson number Ri_c (de Roode et al. 2017), and then $c_{\epsilon S}$ can be determined, as illustrated in Figure 8.1(a).

This closure is also used to model turbulent fluxes of heat, moisture, and other scalar quantities via invocation of a turbulent Prandtl number, Pr_t. An eddy diffusivity can be formed by dividing the eddy viscosity by the turbulent Prandtl number, then subgrid-scale scalar fluxes can be modeled using a gradient diffusion hypothesis. From theoretical considerations, Pr_t is expected to increase from 1/3 to 1 as thermal stratification increases, but the functional form of its variation is an open question. In the Deardorff TKE-based closure, $Pr_t = [1 + 2(l\Delta^{-1})]^{-1}$ and no additional parameters are introduced; thus, uncertainty owing to the modeling of scalar fluxes may be masked. To remedy this, we introduced an additional parameter, n_{Pr}, and we modified the turbulent Prandtl number expression to be $Pr_t = [1 + 2(l\Delta^{-1})^{n_{Pr}}]^{-1}$. Figure 8.1(b) shows how this parameter affects the variation of Pr_t with changing local stability.

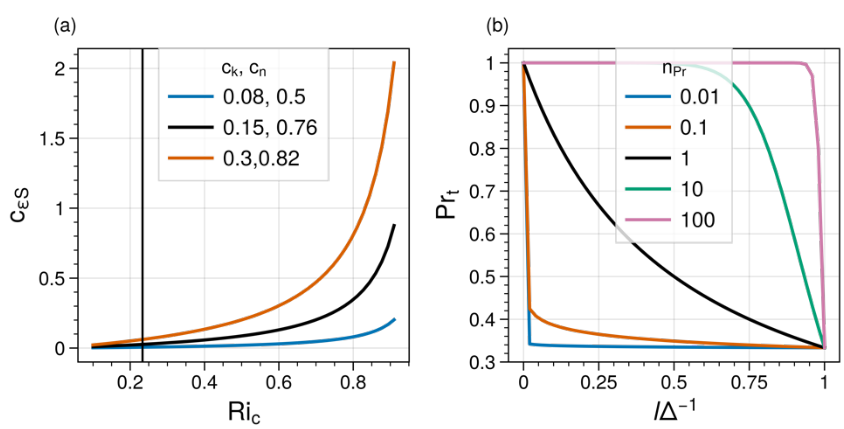

Figure 8.1. Relationships between perturbed parameters and turbulence closure inputs. (a) Relation between the stable stratification regime dissipation coefficient and the SGS critical Richardson number Ri_c. (b) Variation of the turbulent Prandtl number, Pr_t, with the exponential factor n_{Pr}.

The SGS TKE scheme interacts with the surface layer scheme in several ways but most directly through setting the near-surface value of e; therefore, we also consider the effect of varying the surface roughness. This is accomplished by enhancing the default roughness length by a multiplicative factor z_f ranging between 1 and 2, following Yang et al. (2017). We frame our analysis in terms of the logarithm of z_f to be more consistent with how this factor is used within the surface scheme.

Modifications to the WRF source code were required to explicitly define and expose all parameters (except c_k) as options in the namelist input file. This code is available at https://github.com/cmkaul/WRF/tree/les_uq and is a fork of the A2e MMC version of WRF. The parameters tested, their uncertainty ranges, and their default values in WRF are summarized in Table 8.1.

Table 8.1. Parameters varied in the uncertainty analysis. Symbols are defined in the text. The UQ range is the range of values input to the Latin hypercube sampling algorithm. The WRF default is the default version used in WRF v 4.1.2. Note that in the standard WRF release, only c_k is available as a namelist option. The other parameters are not explicitly defined but rather implicitly fixed within the code base.

Parameter	UQ Range	WRF Default
c_k	0.08—0.3	0.15
c_n	0.5—0.82	0.76
$c_{\varepsilon N}$	0.8—1.5	0.93
Ri_c	0.1—1	0.23
n_{Pr}	0.01—100	1
z_f	1—2	1

8.2 Case Selection and Setup

We simulate periods on July 22, 2016, and August 21, 2016, during the WFIP 2 in the Columbia Basin region of Washington and Oregon (Shaw et al. 2019). Both of these days were annotated in the WFIP 2 event log as being associated with marine push events. They feature strong westerly winds (see Figure 8.2) and large surface heat fluxes (Figure 8.4). The August 21 case has also been simulated and compared to lidar observations using a POD technique by MMC project team members, as described in the FY 2019 project report (Haupt et al. 2019c). The event log and observational data may be obtained from the A2e DAP site.

The simulations use three levels of nested domains. The outermost domain has a horizontal grid spacing of 1.35 km and uses a typical suite of physical parameterizations appropriate to mesoscale resolutions. Initial and boundary conditions of this domain are generated from the Global Forecast System reanalysis. We also evaluated the National Centers for Environmental Prediction North American Regional Reanalysis for this purpose but did not find consistent improvement in the agreement between observed and simulated wind speeds. The mesoscale domains are initialized at 12:00 UTC for both case periods and integrated forward for six hours before launching two nested domains. These domains have horizontal grid spacings of 150 m and 50 m, respectively, and both are treated as LES. Then all three domains are run for four or more additional hours. Specifically, the time window 20:20–22:20 UTC is used for detailed analysis of the July 22 case, while the window 20:00–22:00 UTC is used for the August 21 case. These intervals were selected to obtain periods when the simulated wind speeds were relatively uniform, while also allowing spin-up of the nested domains.

The simulation domains are positioned so that all three encompass two measurement locations from the WFIP 2 campaign. Sonic anemometer measurements of wind and temperature at 50-m and 80-m levels were collected at Physics Site-12 (PS-12), while additional observations were obtained at the Wasco, Oregon, airport a few kilometers away. The analysis presented here focuses on comparisons with the PS-12 data.

8.3 Simulation Results

We generated an ensemble of 64 nested WRF/WRF-LES simulations for each case period. These dozens of simulations are needed to adequately sample across the uncertainty ranges of the six parameters identified for our analysis, even when the sample values are selected through an efficient technique. Here, we employ a Latin hypercube sampling algorithm (Stein 1987; Helton and Davis 2003).

All ensemble runs use an identical configuration of the outermost mesoscale domain, and each uses the same set of LES parameter values in the 150-m and 50-m domains; thus, uncertainty quantification analysis can be performed using output from either domain. For brevity, we will refer to the sets of simulations for each case period and at each resolution in the form PPE-date-resolution; for example, PPE-22July-50m indicates the ensemble of results on the finest, 50-m resolution nest for the July 22, 2016, case period.

Time series of the 10-minute average wind speed U_{10min} and corresponding wind direction at the PS-12 location are shown in Figure 8.2. We show results of averaging over the members of the PPE, as well as the full ranges of the ensemble members. Simulated wind speeds on the mesoscale nests are biased low relative to the observed wind speeds for both case periods, as is the mean wind speed of the PPE at 150-m resolution. Additionally, the mean of the 50-m resolution PPE shows better agreement with observations, and the ensemble ranges of both PPEs overlap with the observations during most of the case study periods. The range of wind speed predictions among members of the PPE (either resolution) can be as large as several m s^{-1} and increases rapidly after the LES runs are initiated at 18:00 UTC each day. Sudden troughs in the PPE-21Aug-50m wind speed range are related to the presence of longitudinally extensive coherent structures in the flow, which can also be diagnosed from observations by examining streamwise and cross-stream turbulence timescales. Certain parameter values tend to enhance those structures so that shifts in their position produce a large signal in the velocity time series at a fixed location. Such structures are not significant for July 22.

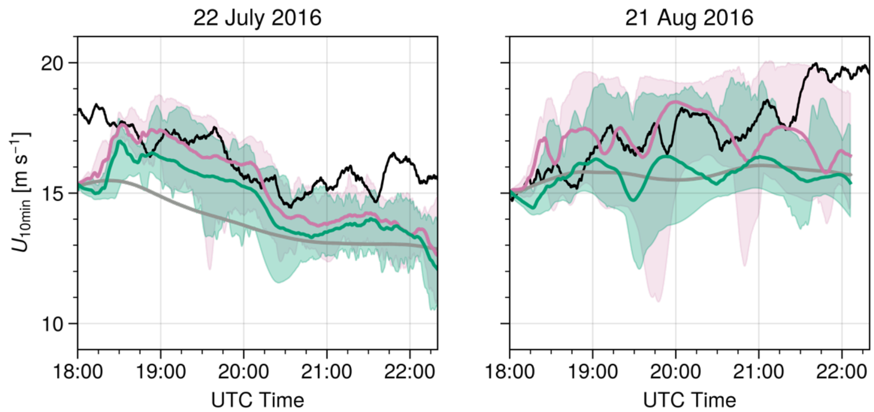

Figure 8.2. Ten-minute averaged wind speeds at 80-m vertical level from the PS-12 location, as observed and simulated. Measurements are shown in black. Gray lines show predictions on the mesoscale domain. The rose (green) solid line is the mean of the PPE at 50-m (150-m) resolution, and the rose (green) shading is the range of the PPE.

Wind direction predictions (Figure 8.3) are in general agreement with observations. The means over the PPEs are rather insensitive to the LES horizontal resolution for both case periods. The ensemble ranges are smaller on August 21 and likely can also be related to the coherent structures of the flow on that day. On July 22, the magnitude and structure of the turbulent fluctuations showed weaker directional dependence, leading to a greater spread.

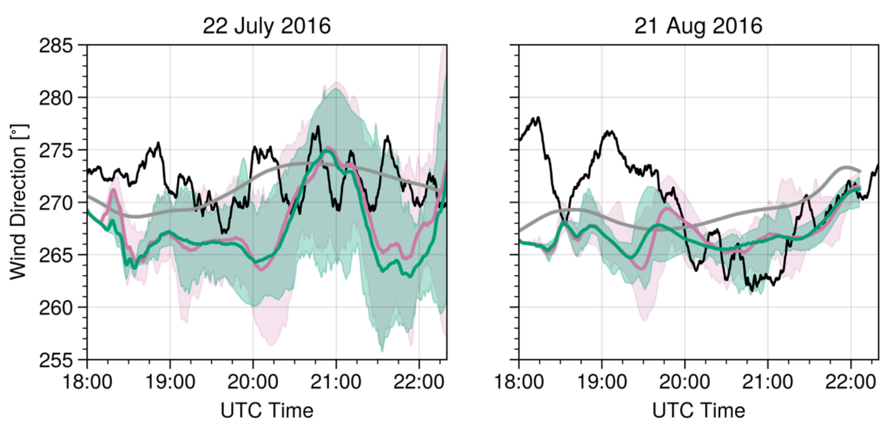

Figure 8.3. Direction of the 10-minute averaged winds at 80-m vertical level from the PS-12 location. Line styles and colors as in Figure 8.2.

Surface sensible heat flux H exceeds 300 W m^{-2} throughout the periods simulated by LES (Figure 8.4). The relative range of U_{10min} at a height of 80 m among the ensemble members is three to six times greater than the relative range of H, which suggests that the spread in wind speed is attributable to factors besides the spread in surface heat fluxes (note also that the intra-ensemble range of surface latent heat fluxes is commensurate or weaker than the spread in H).

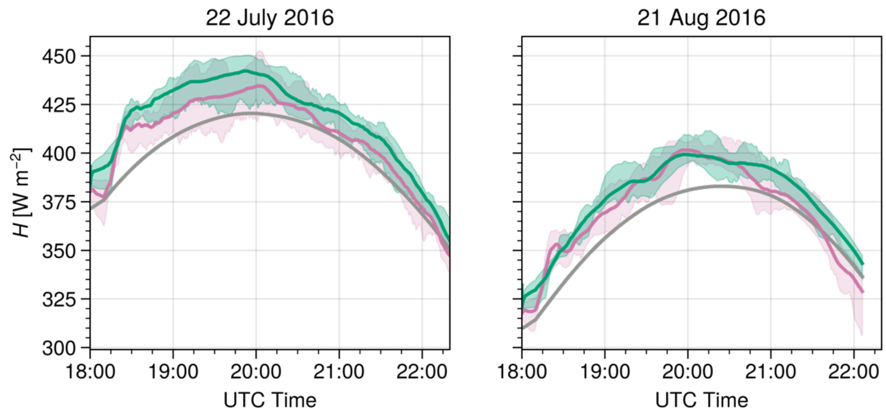

Figure 8.4. Surface sensible heat flux at PS-12. Colors as in Figure 8.2. Note that surface flux measurements are not available at PS-12.

In addition to mean wind speed and direction, simulations were evaluated on how well they captured the intensity and structure of turbulence at hub height and how well they represented the vertical structure of the wind profile (e.g., its shear). These quantities were computed at several heights (50 m, 80 m, 120 m, 190 m) to allow overlap with the available measurements at PS-12 (50 m, 80 m) and to permit analysis of higher levels (120 m, 190 m), which are more relevant to recent and future generations of taller land-based turbines.

Here, we will focus on results at 80-m height for three quantities: the TKE associated with timescales less than 10 minutes, the integral timescale of the turbulence, and the mean wind shear between 50 m and 80 m. First, we discuss a visual assessment of the sensitivity, presented in Figure 8.5 through Figure 8.7. In these figures, the prediction of each member of PPE-22July-50m is represented as a point for each of the two sites versus the value of one of the perturbed parameters. Qualitatively similar conclusions can be reached by examining the August 21 results.

Figure 8.5 shows the total TKE of the horizontal winds associated with timescales less than 10 min, $E_{<10min}$. For reference, the value obtained from observations at PS-12 is 1.14 m^2 s^{-2}. Only for the eddy viscosity parameter c_k is a trend in values apparent, with $E_{<10min}$ declining as c_k increases, until at high values the flow is essentially nonturbulent. Figure 8.6 shows the integral timescale associated with the horizontal winds. The observed value at PS-12 is 90 s. Again, only for c_k can a trend be identified by visual inspection, with timescales tending to increase with c_k. Figure 8.7 shows the average horizontal wind shear between 50 m and 80 m. The observed value at PS-12 is 0.0125 s^{-1}. Once again, c_k dominates the sensitivity, and shear generally increases with increasing eddy viscosity (albeit with some complexities in the relationship at the Wasco site).

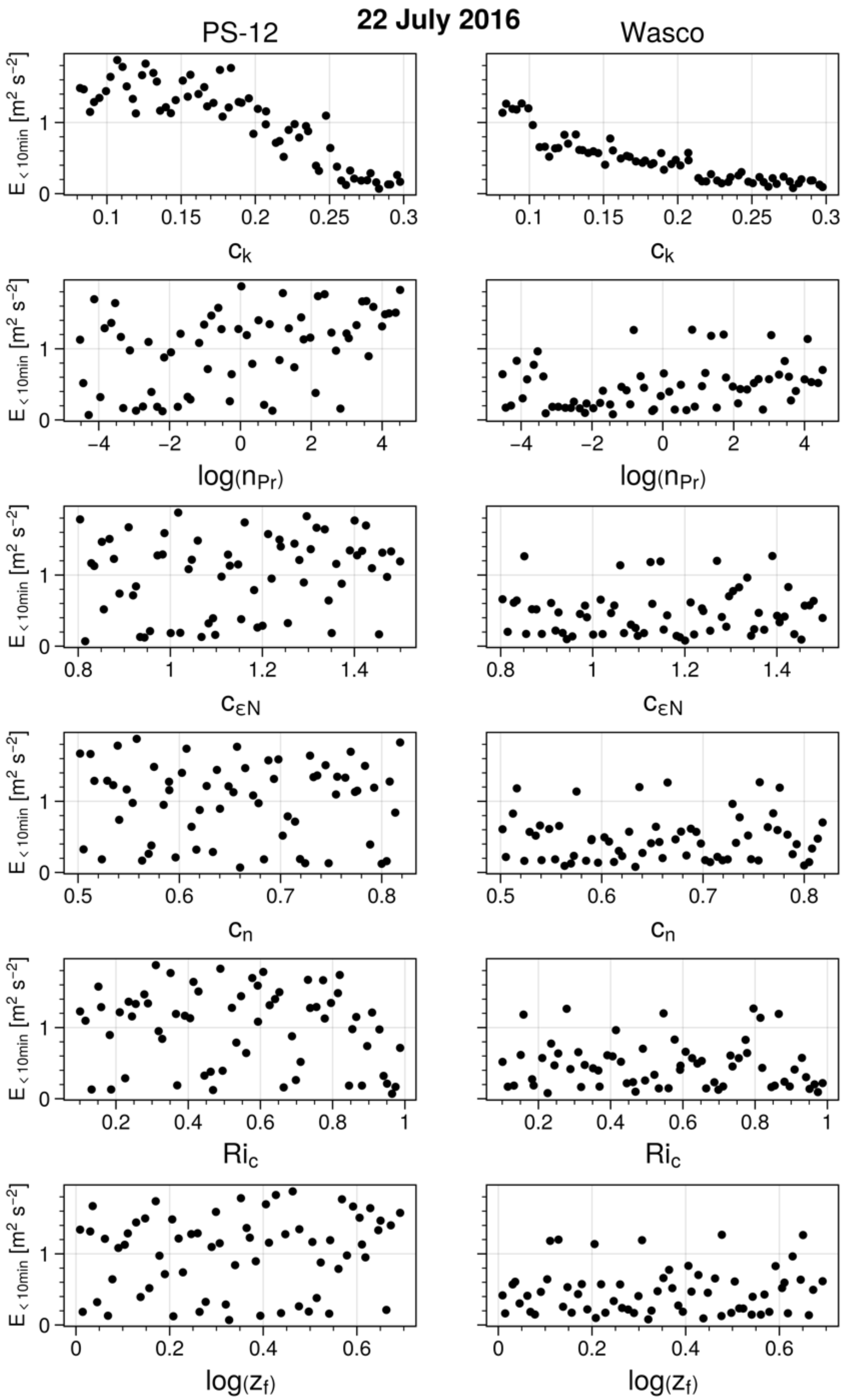

Figure 8.5. Relationship between perturbed parameters and the sub-10-minute TKE of the horizontal winds at 80-m height. Results are shown for the finest (50-m) resolution.

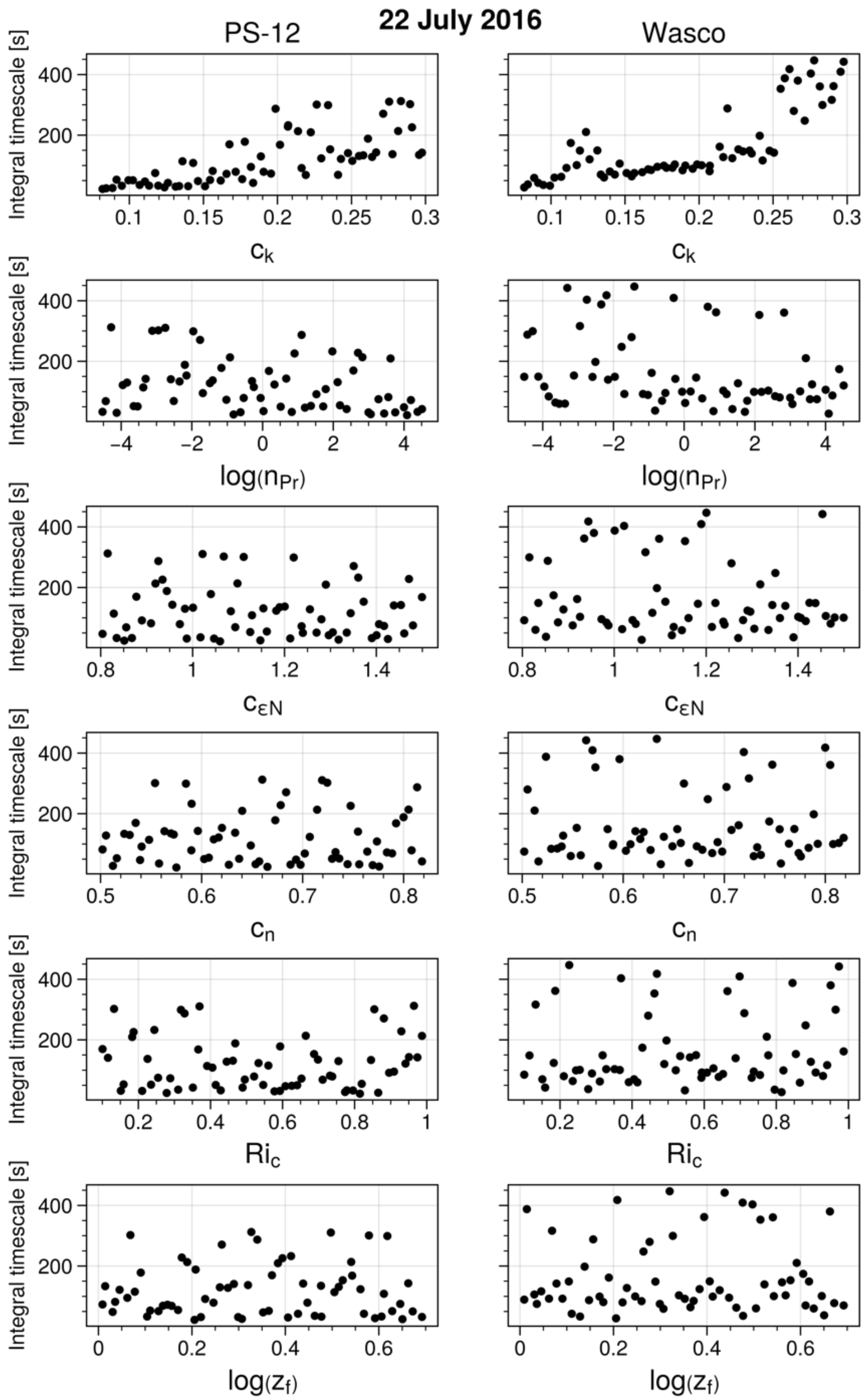

Figure 8.6. Relationship between perturbed parameters and the integral timescale of the horizontal winds at 80-m height. Results are shown for the finest (50-m) resolution.

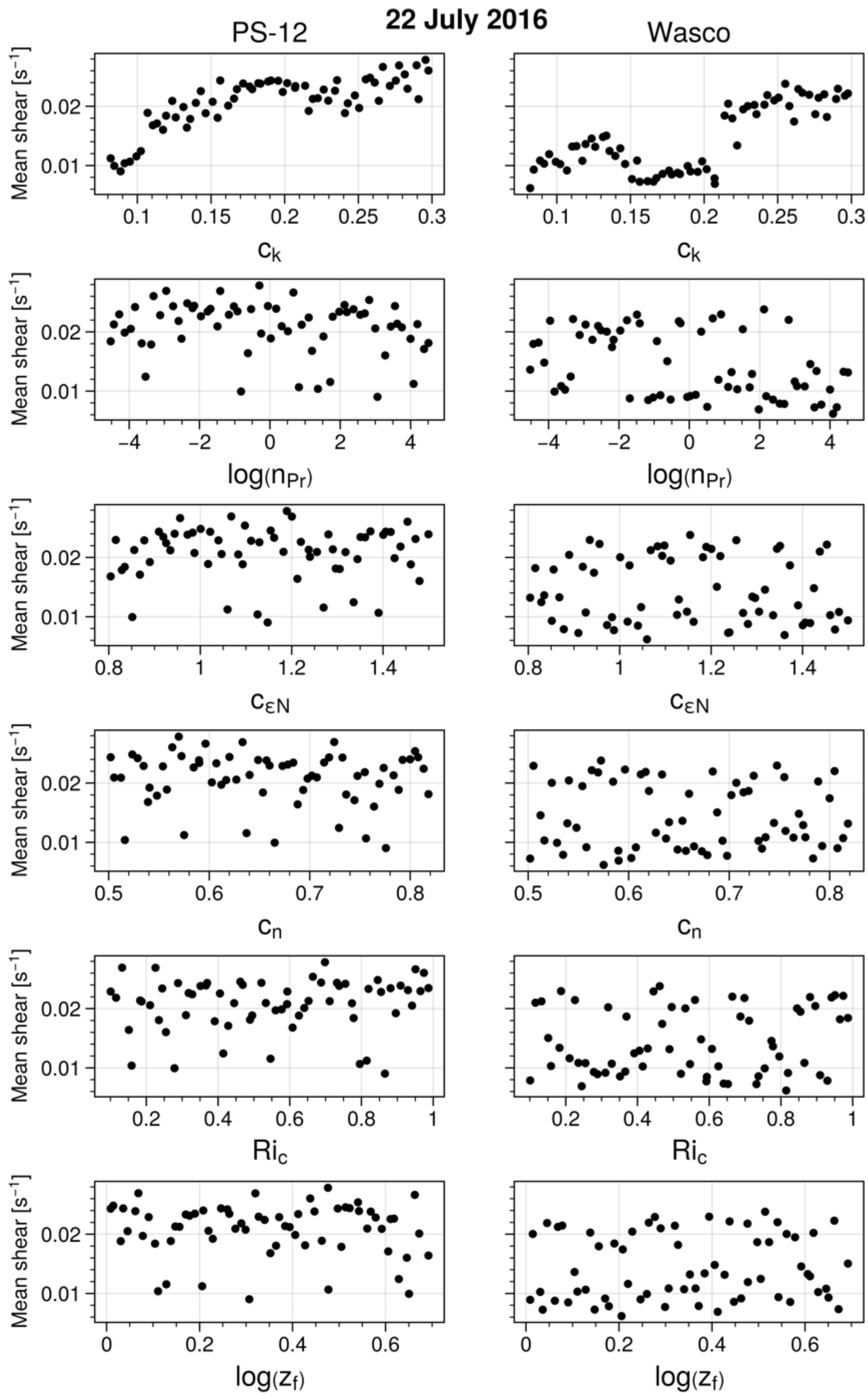

Figure 8.7. Relationship between perturbed parameters and mean horizontal wind shear between 50-m and 80-m heights. Results are shown for the finest (50-m) resolution.

Because the strong dependence on c_k could impede analysis of more subtle relationships with other parameters, and because simulation predictions were clearly degraded at high values of that parameter, we undertook to create a subsample of ensemble members. Rather than directly select specific members for inclusion in the subsample, we ranked the results of the finest resolution (50-m) simulations on the basis of the sum of the relative errors in their predictions of the three quantities shown in Figure 8.5 through Figure 8.7, considering both the July and August case periods, and we selected the simulations ranked first through thirty-second. Although there is no explicit dependence on c_k in this procedure, it has the effect of roughly halving the range of c_k, because all members of the subsample have $c_k < 0.2$.

To further develop and quantify the parameter sensitivity findings presented on a qualitative basis in this section, we undertook a feature importance (FI) analysis using ML tools, as described in the following section. This analysis was performed using both the original ensemble of 64 perturbed parameter combinations and the 32-member subsample with reduced range of c_k.

8.4 Parameter Importance Ranking

ML tools can be used to create models of how the LES results respond to input parameters, referred to as features. Various model types can be used, offering different strengths and weaknesses. Here, we focus on regression with RFs. A description of the method can be found in Genuer et al. (2010), and the implementation in the R environment is discussed by Liaw and Wiener (2002). An advantage of the RF approach is its suitability for identifying parameters that affect the model output nonlinearly.

Briefly, our methodology begins with the construction of a set of data with vectors of explanatory variables, or features, X_i, and vectors of responses, Y_i. Here, the X_i are defined to include the values of the closure parameters $(c_k,\ c_n, c_{\epsilon N},\ Ri_c, n_{Pr}, and\ z_f)$, as well as nonparametric features: the day or date (July 22 or August 21), site (PS-12 or Wasco), resolution (50 m or 150 m), and height level. In our study, the Y_i are various quantities computed from the WRF-LES simulation data.

The method proceeds by growing regression trees using a subset of the data referred to as the training data. The other data are reserved as testing data to allow the accuracy of the RF model to be assessed. Once the RF model has been constructed, techniques can be applied to assess the importance of a feature. RF FI is an impurity-based measure of importance that looks at the relative depth at which different features are used as decision nodes in the trees composing the RF. Two main weaknesses of FI are, first, that it is based entirely on the training data and does not depend on the testing data; and second, that it can overestimate the importance of many-valued features. The RF FI technique can be complemented by an alternative, more general (i.e., nonspecific to RF models) procedure called permutation importance (PI) ranking (Genuer et al. 2010). In the PI technique, feature values are, by turn, randomly permuted, and the change in the model score is computed. The greater the decrease in the model's score, the more important the permuted parameter is deemed to be. We present results using FI (Figure 8.8), but we also performed PI analysis as a check. In all the figures in this section, the upper panel shows results using the full 64 combinations of parameter value samples, while the lower panel shows results with the subset of 32 parameter combinations (identified as described in Section 8.3).

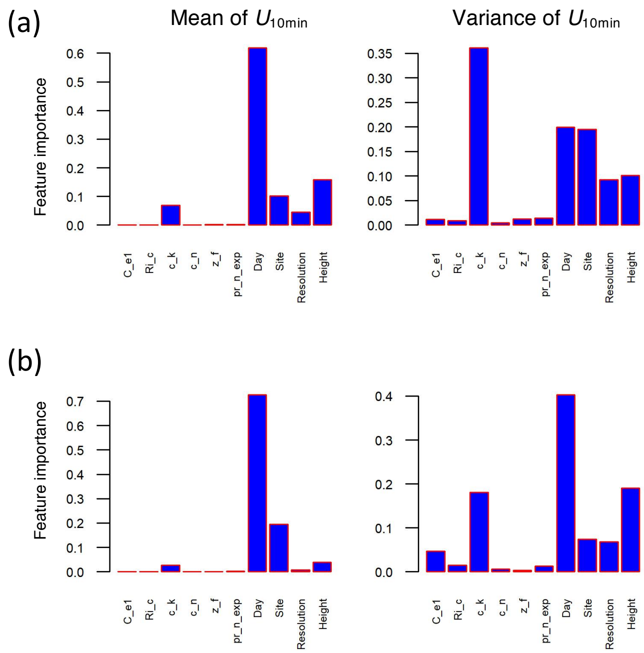

Figure 8.8. Feature importance for moments of the 10-minute averaged horizontal winds considering (a) the full 64-member ensemble and (b) the reduced 32-member ensemble.

Figure 8.8 depicts FI for prediction of the mean and variance of the 10-minute averaged wind speed over the analysis windows specified in Section 3.2. Predictions of the means is (unsurprisingly) dominated by the case day. In the full set of data, the importance of c_k is similar to that of the site or height, while its importance is diminished in the subsample, and the importance of the site is relatively increased. Turning to the variance of U_{10min}, c_k has the greatest FI rating among all features in the full sample, followed by the nonparametric features, and c_k remains important in the subsample (but less so than the day and about equally important as height). Interestingly, resolution is always among the least important of the nonparametric features.

Influence on the shape of the energy spectra is examined in Figure 8.9. To isolate shape, we normalized each PPE member's spectrum by its total energy (i.e., the quantity plotted in Figure 8.5), then looked how that total energy was divided among ranges of frequencies (or inverse timescales). The eddy viscosity coefficient stands out as the dominant parameter for both the full and reduced samples and remains an important feature overall even in the reduced sample. We also observe a high importance of resolution, especially for determining the relative energy content at higher frequencies (shorter timescales).

Finally, FI prediction for mean and variance of wind shear (change of wind speed with height) and wind veer (change of wind direction with height) are plotted in Figure 8.10. These quantities were computed between 50 m and 80 m, between 50 m and 120 m, and between 120 m and 190 m (the latter two combinations being reflective of hub heights and blade lengths of a large land-based turbine). Mean veer is strongly site-dependent in both the full and subsamples, while c_k is the dominant parameter and has roughly equal importance to the remaining nonparametric features. In contrast, mean shear is most dependent on height. Again, as for the veer, c_k is the dominant parameter and has roughly equal importance to the remaining nonparametric features. For variances of shear and veer, attribution of importance is more complex, but it is generally dominated by the nonparametric features and c_k.

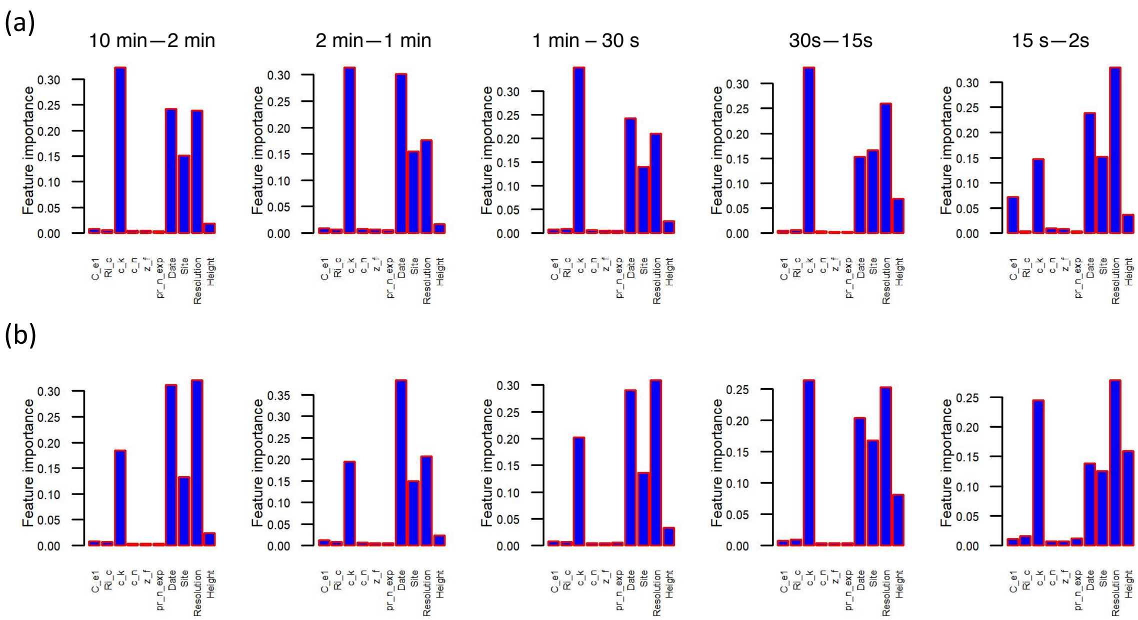

Figure 8.9. Feature importance for the relative contributions of different timescale ranges to the TKE of the horizontal winds for (a) the full 64-member ensemble and (b) the reduced 32-member ensemble.

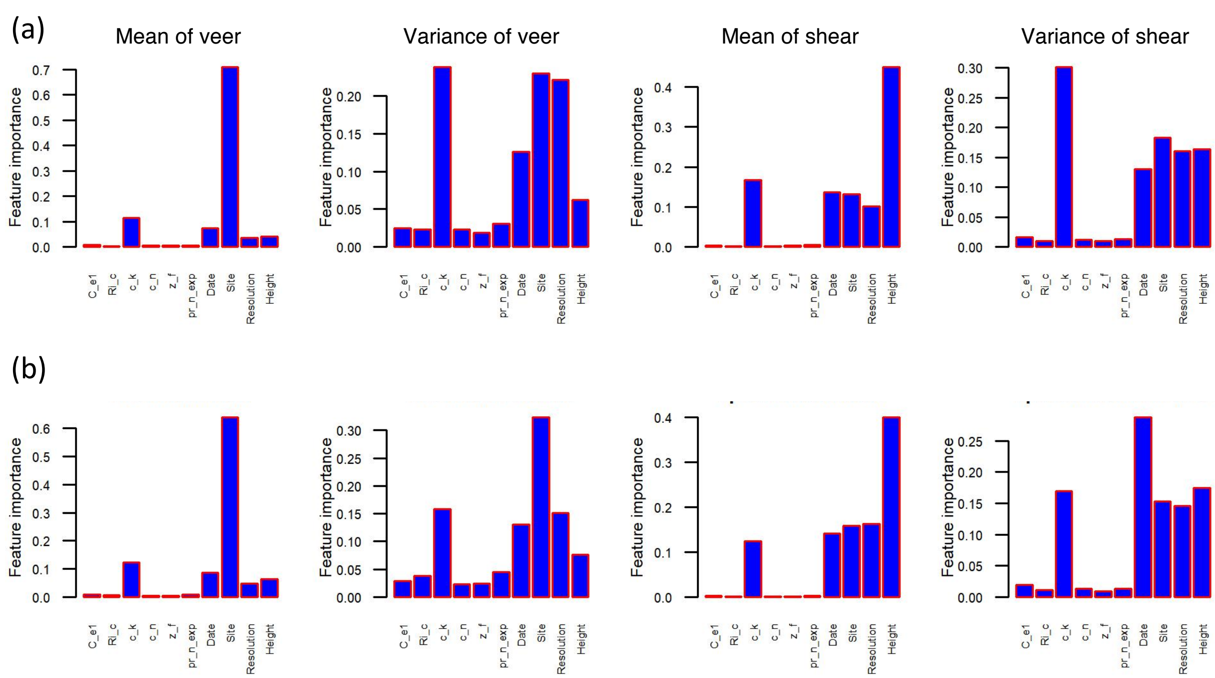

Figure 8.10. Feature importance for moments of the vertical derivatives of the horizontal wind direction (veer) and speed (shear) for (a) the full 64-member ensemble and (b) the reduced 32-member ensemble.

8.5 Summary and Next Steps

We created a database of 128 nested WRF/WRF-LES simulations, comprising 64 combinations of perturbed parameters related to the LES subgrid-scale turbulence closure evaluated over two case periods during the WFIP 2 campaign. Due to the large-scale weather pattern in the region on these two days associated with marine push events, both cases exhibit high westerly winds and strong surface fluxes; however, spatial organization of turbulence and other detailed features differed between the two days. From the simulation data, we computed a number of quantities relevant to wind energy associated with wind speed, direction, turbulence characteristics, and vertical variations.

Both qualitative analysis of the results and quantitative assessments of FI using ML techniques highlighted that, among all the tested parameters, c_k stands out in importance. Even when the original 64-parameter combinations were subset to 32 (roughly having the range of c_k), it remains more influential than any other parameter. Our findings also indicate WRF's default value of this parameter, 0.15, is larger than ideal for these cases, and a value around 0.1 (commonly recommended for LES) yields better results.

Lest it be concluded that the usefulness of LES is impeded by this sensitivity to the eddy viscosity, we note that our results indicate the range of values likely to work well is actually fairly narrow, and even for these highly nonidealized simulations, they are consistent with recommendations in the literature for idealized LES. This suggests a useful suite of sensitivity tests can actually be conducted with a limited number of simulations. Furthermore, nonparametric features (especially date and site) are also typically very important, indicating there is a high value to accounting for mesoscale variability and details of terrain by performing realistic, mesoscale-to-microscale coupled simulations.

Finally, we remark that further work is needed to examine how these parameter sensitivities and FI rankings change under a wider array of case studies, especially considering conditions of stable stratification such as might be encountered nocturnally over land or offshore. By undertaking the present study, however, we have developed a framework of approaches and techniques that can enable such new efforts.

9.0 Synthesis and Summary

9.1 Summary Overview

Understanding and providing modeling capabilities of the atmospheric forcing of the flow into and around a wind farm is critical to optimizing use of this important energy resource. To that end, the MMC project has been performing research to provide that knowledge and modeling capacity. The team has worked together over a 5-year period to study details of the science needed by industry, both in the near term and looking forward to the challenges and opportunities that will emerge as wind power penetration grows.

During FY 2020, the MMC team has continued to collaborate to advance the science and application of coupling mesoscale models to microscale models for the purpose of better simulating wind plants. The team has made major advances in FY 2020, advancing our land-based modeling techniques in terms of enhancing the 3D PBL parameterization, evaluating LES with lidar, evolving a new ML approach to modeling the surface layer, continuing to evaluate best methods to generate turbulence at the microscale, studying how to best damp gravity wave growth in microscale simulations, modeling a realistic case at the Peetz Table Wind Energy Center in Colorado in collaboration with the Wake Dynamics team, and quantifying the parametric uncertainty of microscale modeling for highly sheared convective flow in complex terrain. Each of these is summarized briefly below. In addition, the team worked with our industry advisory panel to plan and execute the Atmospheric Challenges for the Wind Energy Industry Workshop, which is reported on separately. Furthermore, the team tested the application of our MMC techniques to an offshore challenge case that will also be reported on separately.

9.2 Advancing the Three-Dimensional Planetary Boundary-Layer Parameterization

Our MMC team has extended the new 3D PBL parameterization to include the complete level 2.5 model based on the developments of Mellor and Yamada (1982). The most notable enhancement to the parameterization in FY 2020 includes implementation of the full 3D prognostic equation for TKE. We anticipate that this advancement will improve simulations in the “gray zone” (horizontal grid spacings from about 100 m to 1000 m), also known as the *terra incognita*. In order to test the capability of the new parameterization, we configure an idealized mountain-valley case of a growing convective boundary layer. This case is selected because, during periods of solar insolation in mountain-valley terrain, the variation in elevation induces a thermally driven valley circulation and, thus, heterogeneous conditions. We expect to see differences between the 1D and 3D PBL solutions. Indeed, while the valley circulation is depicted in both the 1D and 3D PBL simulations, the 1D PBL solution produces motions consistent with so-called modeled convectively induced secondary circulations, which arise in gray zone simulations when the 3D turbulent mixing is not handled correctly. These results are preliminary and will, therefore, be extended by conducting high-resolution LES and examining turbulence statistics. Moreover, a manuscript synthesizing these results, in addition to results from other idealized configurations (i.e., sea breeze case and convective cell/roll convection case), is currently in preparation.

9.3 Characterization of Turbulence Scale from Scanning Lidar

Scanning lidar data collected during the WFIP 2 campaign from 2015 to 2017, near the Columbia Gorge, Oregon, were used to evaluate the turbulent energy and flow structures near the surface under different atmospheric conditions. We employed both spectral and POD methods to evaluate the kinetic energy present in the turbulent flow and flow structures under varying surface flux conditions using ensembles of radial wind velocity measured by scanning Doppler lidar. Both methods predict similar variation of turbulent energy in the higher mode/wave number space for different cases. The spatial POD mode using ensemble data reveals shapes and sizes of coherent structures that depend on the forcing conditions. The shapes become streakier and more slender for negative heat flux conditions, as compared to cases with positive heat flux. These variations of flow structures significantly impact the energy distribution throughout the boundary layer and to the man-made structures near the surface, such as wind turbines.

9.4 Machine Learning Approach to Modeling the Surface Layer

Surface fluxes of momentum, sensible heat, and moisture in virtually all numerical models for simulation of high-Reynolds ABL flows are estimated using MOST (Monin and Obukhov 1954). While MOST is based on the assumption of horizontal homogeneity and stationarity, it is commonly applied even when these conditions are violated. This often results in large differences between predicted and observed fluxes. Application of an ML approach using high-quality, long-term observations represents a possibility to develop a more general surface layer model. We have, therefore, developed two ML models for surface layer parameterization based on ANN and RF algorithms trained and tested using surface layer observations at two locations: the Cabauw mast in the Netherlands and the NOAA Air Resources Laboratory's Field Research Division site in Idaho. ML estimates of surface friction velocity, temperature scale, and moisture scale are compared to MOST estimates. ML models were trained on both datasets, as well as their combination. Both ML models outperformed MOST in terms of MAE and R^2 metrics, even when they were trained on one dataset and tested on the other. The only exception is for the ANN temperature scale model trained on the Cabauw dataset and tested on the Idaho dataset. While models tested on a different dataset from the one they were trained on performed worse than when tested on the same dataset they were trained on, they still outperformed MOST. The models trained on the combined dataset performed better than those trained on one dataset and tested on another. Our analysis demonstrates the potential for ML models to replace MOST. The next steps will include implementation and evaluation of the ML models in the WRF model.

9.5 Turbulence Generation Methods Over Simple Terrain

Further progress was made on the task to evaluate various inflow turbulence perturbation methods, developed to accelerate the formation of turbulence in turbulence-resolving LES domains forced with mesoscale inflow. Work completed this year involved improving the common code bases used to simulate and assess the flows, which are now available on the public MMC GitHub, as well as to execute and analyze simulations of several perturbation techniques during a case study representing canonical convective conditions. The goal this year was to extend the evaluation to near-neutral and stable conditions, as well; however, this work was delayed, in part, due to an inability to retrieve some of the data required to specify one of the case studies and, in part, to redirection of efforts of key members of the perturbation team to setting up and executing a new offshore challenge case. Despite the setbacks, the team has developed a stable case study, provided the source code to execute the case study via an imposed surface cooling rate, and also has a path forward to develop a near-neutral case study. The team will complete the perturbation analysis in all three stability classes during FY 2021.

9.6 Gravity Wave Issues and Resolutions

Further investigation of the use of Rayleigh damping layers to suppress spurious reflection of gravity waves on the boundaries of the domain were conducted during FY 2020. Visual inspections of the flow field indicate that they were effective, but solutions were sensitive to their placement, thickness, and strength. It was observed that an effective approach is to use 3-km-thick Rayleigh damping layers on all side boundaries of the domain in addition to the top boundary. The appropriate strength is problem-dependent and seems to be related to the wind speed magnitude. These initial investigations were conducted using damping layers that extended all the way to the bottom boundary. The use of such damping layers is inappropriate for MMC practices, because turbulent flow entering the domain is also damped. Future effort will include imposing a vertical filter on the damping layers present on the side of the domain and assessing its effectiveness in more realistic cases that make use of the MMC team's strategies. Preliminary testing indicates that the filter is effective in damping the undesired fluctuations, while not disturbing turbulent inflow entering the domain.

9.7 Modeling for Wind Turbines—Peetz Table Case Study

The Wake Steering field campaign at Peetz Table Wind Energy Center in northeastern Colorado provided an excellent opportunity to demonstrate our MMC capabilities. Given meteorological mast and profiling lidar measurements of the instantaneous atmospheric state, we were able to successfully reproduce the corresponding nonstationary turbulence with LES. This was accomplished by assimilating the hub-height wind history during the daytime and assimilating the time-height wind profiles reconstructed up to the maximum lidar range of 180 m AGL. In addition, temperature assimilation at 59-m AGL was necessary to reproduce the observed near-surface temperature evolution—this is likely driven by the dynamics of a stationary front. A 23-hour period was simulated, starting from 5 a.m. local time, with a period of interest after midnight on the following day. Simulated nighttime turbulence levels agree reasonably well with measurements and capture the effect of an observed shear instability.

9.8 Uncertainty Quantification of Large-Eddy Simulations in Complex Terrain

Uncertainty quantification methodologies were used to understand parametric sensitivities of realistic LES of highly sheared, convective flows in complex terrain, which were performed via nesting from mesoscale WRF to WRF-LES. Sensitivities to parameters of a 1.5-order, TKE-based subgrid-scale turbulence closure, and to the surface roughness were assessed by performing 128 simulations to populate a set of perturbed parameter ensembles. The prediction of a number of quantities relevant to wind energy applications—such as hub-height winds, turbulence, and shear—were found to be overwhelmingly sensitive to a single parameter (the eddy viscosity coefficient) of the turbulence closure. RF representations of the simulation output were also constructed and used to quantitatively assess parameter sensitivity using FI and PI methods. This analysis confirmed the importance of the eddy viscosity coefficient and also allowed examination of sensitivities to factors such as the case study identity, measurement location and vertical level, and simulation resolution.

9.9 Effectiveness of Cross-Laboratory Collaboration

The success of the research highly depends on our collaborative efforts across labs and across topics. This team currently comprises four DOE laboratories plus NCAR. The team has learned to communicate well and to help each other when we identify challenges. This process is convergent, in the sense that it brings together researchers with different but complementary academic and research backgrounds to study very complex, societally relevant problems. Through the deeply synergistic working relationships that have developed over multiple years of teaming, the team has honed our ability to effectively aid each other as we progress the science needed to provide the knowledge and understanding to expand wind energy deployment.

9.10 Plans for the Future

The land-based portion of the MMC team's research will be wrapping up over the coming two years. During FY 2021, the team plans to complete comparative studies of the different perturbation technologies and coupling methodologies, providing recommendations for best practices. The team will continue to advance the land-based application of the 3D PBL model and ML-based surface parameterization. We will also define cases of shallow convective boundary layers in the U.S. Great Plains, as well as studies on low-level jets, an important but inadequately understood phenomenon that greatly impacts energy harvesting in that wind-rich region of the country. In addition, the MMC team will harden and document our codes so that they can be made widely available to industry, along with providing a series of recommendations for best practices under different conditions. In parallel, the same team will test our methods in the offshore environment under the Offshore Wind Atmospheric Coupling project. We look forward to maturing and disseminating this body of work so that it can help to fulfill the vision of efficiently and abundantly harvesting the clean, renewable wind resource.

10.0 References

Allaerts, D., C. Draxl, E. Quon, and M. Churchfield, 2020: Large-Eddy Simulation of a Diurnal Cycle Driven by Assimilation of Mesoscale Time-Height Profiles, *Boundary-Layer Meteorology*, **176**, 329–348. doi: 10.1007/s10546-020-00538-5.

Anderson, E., et al., 1999: LAPACK Users' Guide. 3d ed., Society for Industrial and Applied Mathematics, Philadelphia, PA.

Berg, L. K., Y. Liu, B. Yang, et al*.,* 2019*:* Sensitivity of Turbine-Height Wind Speeds to Parameters in The Planetary Boundary-Layer Parametrization Used in the Weather Research and Forecasting Model: Extension to Wintertime Conditions. *Boundary-Layer Meteorol.,* **170**, 507–518. doi:10.1007/s10546-018-0406-y.

Blackadar, A. K., 1962: The Vertical Distribution of Wind and Turbulent Exchange in a Neutral Atmosphere, *J. Geophys. Res.*, **67 (8)**, 3095–3102. doi:10.1029/JZ067i008p03095.

Breiman, L., 2001: Random Forests, *Machine Learning* 45:1, 5–32. doi:10.1023/A:1010933404324.

Businger, J. A., J. C. Wyngaard, Y. Izumi, and E. F. Bradley, 1971: Flux-Profile Relationships in the Atmospheric Surface Layer. *J. Atmos. Sci*., **28**, 181–189.

Ching, J., R. Rotunno, M. LeMone, A. Martilli, B. Kosović, P. A. Jimenez, and J. Dudhia, 2014: Convectively Induced Secondary Circulations in Fine-Grid Mesoscale Numerical Weather Prediction Models. *Mon. Wea. Rev.*, **142**, 3284–3302. doi: 10.1175/MWR-D-13-00318.1.

Deardorff, J. W., 1980: Stratocumulus-Capped Mixed Layers Derived from a Three-Dimensional Model. *Bound. Layer Meteor.*, **18,** 495–527.

de Roode, S. R., H. J. J. Jonker, B. J. H. van de Wiel, V. Vertregt, and V. Perrin, 2017: A Diagnosis of Excessive Mixing in Smagorinsky Subfilter-Scale Turbulent Kinetic Energy Models. *J. Atmos. Sci.,* **74**, 1495–1511.

Draxl, C., D. Allaerts, E. Quon, and M. Churchfield, 2020: Coupling Mesoscale Momentum and Temperature Budget Components to Large-Eddy Simulations for Wind Energy Applications, *Boundary-Layer Meteorology*, submitted.

Dyer, A. J., and B. B. Hicks, 1970: Flux-Gradient Relationships in the Constant Flux Layer. *Quart. J. R. Met. Soc.*, **96**, 715–721.

Eghdami, M., A. P. Barros, P. A. Jimenez, T. W. Juliano, and B. Kosović, 2020: Prediction of Second-Order Turbulent Properties of the Surface Boundary Layer for Three-Dimensional Flow Based on Mellor and Yamada Model. *In press*.

Genuer, R., J.-M. Poggi, and C. Tuleau-Malot, 2010: Variable Selection Using Random Forests. *Pattern Recognition Letters,* **31**, 2225–2236.

Haupt, S. E., L. Berg, M. Churchfield, B. Kosović W. Shaw, and J. Mirocha, 2019a: Mesoscale to Microscale Coupling for Wind Energy Applications: Addressing the Challenges, *Journal of*

Physics Conference Series (2020) 012076 **1452**, NAWEA/WindTech Conference, Amherst, MA, October 15, 2019. doi:10.1088/1742-6596/1452/1/012076.

Haupt, S. E., B. Kosovic, W. Shaw, L. Berg, M. Churchfield, J. Cline, C. Draxl, B. Ennis, E. Koo, R. Kotamarthi, L. Mazzaro, J. Mirocha, P. Moriarty, D. Munoz-Esparza, E. Quon, R. K. Rai, M. Robinson, and G. Sever, 2019b: On Bridging a Modeling Scale Gap: Mesoscale to Microscale Coupling for Wind Energy, *Bulletin of the American Meteorological Society,* Dec. 2019, 2533–2549. doi: 10.1175/BAMS-D-18-0033.1.

Haupt, S. E., D. Allaerts, L. Berg, M. Churchfield, A. DeCastro, C., Draxyl, D. J. Gagne, P. Hawbecker, P. Jimenez, A. Jonko, T. Juliano, C. Kaul, B. Kosovic, RT. C. McCandless, J. Mirocha, D. Munoz-Esparza, E. Quon, R. Rai, J. Sauer, and W. Shaw, 2019c: FY19 Report of the Atmosphere to Electrons Mesoscale to Microscale Coupling Project: Pacific Northwest Laboratory Report PNNL-28259, 127 pp.

Haupt, S. E., D. Allaerts, L. Berg, M. Churchfield, A. DeCastro, C., Draxyl, E. Koo, B. Kosovic, R. Kotamarthi, B. Kravitz, L. Mazzaro, J. Mirocha, E. Quon, R. Rai, J. Sauer, G. Sever, and W. Shaw, 2019d: FY18 Report of the Atmosphere to Electrons Mesoscale to Microscale Coupling Project: Pacific Northwest Laboratory Report PNNL-28259, 124 pp.

Haupt, S. E., A. Anderson, R. Kotamarthi, J. J. Churchfield, Y. Feng, C. Draxl, J. D. Mirocha, E. Quon, E. Koo, W. Shaw, R. Linn, L. Berg, B. Kosovic, R. Rai, B. Brown, and B. L. Ennis, 2017: Second Year Report of the Atmosphere to Electrons Mesoscale to Microscale Coupling Project: Nonstationary Modeling Techniques and Assessment, Pacific Northwest Laboratory Report PNNL-26267, 156 pp.

Haupt, S. E., A. Anderson, L. Berg, B. Brown, M. J. Churchfield, C. Draxl, B. L. Ennis, Y. Fang, B. Kosović, Rs. Kotamarthi, R. Linn, J. D. Mirocha, P. Moriarty, D. Munoz-Esparaza, R. Rai, and W. J. Shaw, 2015: First Year Report of the A2e Mesoscale to Microscale Coupling Project, Pacific Northwest Laboratory Report PNNL-25108, 124 pp.

Helton, J. C., and F. J. Davis., 2003: Latin Hypercube Sampling and the Propagation Of Uncertainty in Analyses Of Complex Systems, *Reliability Engineering & System Safety* **81**.1, 23–69.

Holmes, P., J. L. Lumley, G. Berkooz, and C. W. Rowley, 2012: *Turbulence, Coherent Structures, Dynamical Systems and Symmetry*. Cambridge University Press.

Juliano, T. W., B. Kosović, P. A. Jimenez, A. Martilli, M. Eghdami, and S. E. Haupt, 2020: A New Three-Dimensional Planetary Boundary-Layer Parameterization for “Gray Zone” Simulations. *In press*.

Kosović, B., P. Jimenez, T.W. Juliano, A. Martilli, M. Eghdami, A.P. Barros, and S.E. Haupt, 2019: Three-Dimensional Planetary Boundary-layer Parameterization for High-Resolution Mesoscale Simulations, *J. Physics Conference Series* (2020) **1452** 012080, NAWEA/WindTech Conference, Amherst, MA. doi:10.1088/1742-6596/1452/1/012080.

Liaw, A., and M. Wiener, 2002: Classification and Regression by Random Forest, *R News,* **2/3**, 18–22.

Mahrt, L., 2014: Stably Stratified Atmospheric Boundary Layers. *Annual Review of Fluid Mechanics*, **46**, 23–45. doi: 10.1146/annurev-fluid-010313-141354.

Mann, J., 1998: Wind Field Simulation. *Probabilistic Engineering Mechanics*, **13**(4), 269–282. doi: 10.1016/S0266-8920(97)00036-2.

Mazzaro, L. J., E. Koo, D. Munoz-Esparza, J. K. Lundquist, and R. R. Linn, 2019: Random Force Perturbations: A New Extension of the Cell Perturbation Method for Turbulence Generation in Multiscale Atmospheric Boundary-layer Simulations. *Journal of Advances in Modeling Earth Systems*, **11**, 2311–2329. doi: 10.1029/ 2019MS001608.

Mazzaro, L. J., D. Muñoz-Esparza, J. K. Lundquist, and R. R. Linn, 2017: Nested Mesoscale-to-LES Modeling of the Atmospheric Boundary Layer in the Presence of Under-Resolved Convective Structures, *Journal of Advances in Modeling Earth Systems*, **9**, 1795–1810. doi: 10.1002/2017MS000912.

Mellor, G. L, 1973: Analytic Prediction of the Properties of Stratified Planetary Surface Layers, *Journal of the Atmospheric Sciences*, **30**, 1061–1069. doi: 10.1175/1520-0469(1973)030<1061:APOTPO>2.0.CO;2.

Mellor, G. L., and T. Yamada, 1982: Development of a Turbulence Closure Model for Geophysical Fluid Problems. *Reviews of Geophysics* **20**, 851–875. doi: 10.1029/RG020i004p00851.

Mellor, G. L., and T. Yamada, 1974: A Hierarchy of Turbulence Closure Models for Planetary Boundary Layers. *Journal of the Atmospheric Sciences*. **31**, 1791–1806. doi: 10.1175/1520-0469(1974)031<1791:AHOTCM>2.0.CO;2.

Mirocha, J. D., M. J. Churchfield, D. Munoz-Esparaza, R. Rai, Y. Feng, B. Kosovic, S. E. Haupt, B. Brown, B. L. Ennis, C. Draxl, J. S. Rodrigo, W. J. Shaw, L. K. Berg, P. Moriarty, R. Linn, R. V. Kotamarthi, R. Balakrishnan, J. Cline, M. Robinson, and S. Ananthan, 2018: Large-Eddy Simulation Sensitivities to Variations of Configuration and Forcing Parameters in Canonical Boundary Layer Flows for Wind Energy Applications, *Wind Energy Science,* **3***,* 589–613. doi: 10.5194/wes-3-589-2018.

Monin, A. S., and A. M. Obukhov, 1954: Basic Laws of Turbulent Mixing in The Surface Layer of the Atmosphere." original *Transactions Akademia Nauk SSSR Geophiziki Institute* **24**, 163-187, 1954. Based on a translation from the original Russian by John Miller for Geophysics Research Directorate, AF Cambridge Research Centre, Cambridge, Massachusetts.

Muñoz-Esparza, D., J. K. Lundquist, J. A. Sauer, B. Kosović, and R. R. Linn, 2017: Coupled Mesoscale-LES Modeling of a Diurnal Cycle During The CWEX-13 Field Campaign: From Weather to Boundary-Layer Eddies, *Journal of Advances in Modeling Earth Systems*, **9,** 1572–1594. doi:10.1002/2017MS000960.

Muñoz-Esparza, D., and B. Kosović, 2018: Generation of Inflow Turbulence in Large-Eddy Simulations of Nonneutral Atmospheric Boundary Layers with the Cell Perturbation Method. *Monthly Weather Review*, **146**(6), 1889–1909.

Muñoz-Esparza, D., Sharman, R., Sauer, J., and Kosović, B., 2018: Toward Low-Level Turbulence Forecasting at Eddy-Resolving Scales. *Geophysical Research Letters*, **45**(16), 8655–8664.

Obukhov, A.M., 1948: Turbulence in the Temperature-Heterogeneous Atmosphere. *Transactions of the Institute of Theoretical Geophysic*s, **1**, 95–115.

Pedregosa et al., 2011: Scikit-learn: Machine Learning in Python, *Journal of Machine Learning Research,* **12**, pp. 2825–2830.

Quon, E. W., A. S. Ghate, and S. K. Lele, 2018: Enrichment Methods for Inflow Turbulence Generation in the Atmospheric Boundary Layer. *Journal of Physics: Conference Series*, **1037**, 072054. doi: 10.1088/1742-6596/1037/7/072054.

Rai, R. K., L. K. Berg, B. Kosovic, S. E. Haupt, J. D. Mirocha, B. Ennis, and C. Draxl, 2019: Evaluation of the Impact of Horizontal Grid Spacing in Terra Incognita on Coupled Mesoscale-microscale Simulations using the WRF Framework, *Monthly Weather Review*, **147**, 1007–1027. doi: 10.1175/MWR-D-18-0282.1.

Rai, R. K., L. K. Berg, B. Kosović, J. D. Mirocha, M. S. Pekour, and W. J. Shaw, 2017: Comparison of Measured and Numerically Simulated Turbulence Statistics in a Convective Boundary Layer Over Complex Terrain, *Boundary-Layer Meteorology*,**163**, 69–89.

Rai, R. K., Berg, L. K., Kosović, B., Mirocha, J. D., Pekour, M. S., and Shaw, W. J., 2016: Comparison of Measured and Numerically Simulated Turbulence Statistics in a Convective Boundary Layer Over Complex Terrain. *Boundary-Layer Meteorology*, **163**, 69–98.

Reed, D. R., and R. J. Marks, 1999. Neural Smithing: Supervised Learning in Feedforward Artificial Neural Networks. Reed, D. R., Marks, R. J., Eds. MIT Press, pp. 358. Cambridge, MA USA.

Rodrigo, J. S., M. Churchfield, and B. Kosovic, 2016: Atmospheric Boundary Layer Modeling Based on Mesoscale Tendencies and Data Assimilation at Microscale, *Wind Energy Science*. doi: 10.5194/wes-2016-26.

Rosenblatt, F., 1958: The Perceptron: A Probabilistic Model for Information Storage and Organization in the Brain. *Psychological Review,* **65**, 386–408.

Schmidli, J., and R. Rotunno, 2010: Mechanisms of Along-Valley Winds and Heat Exchange over Mountainous Terrain. *Journal of the Atmospheric Sciences*, **67**, 3033–3047. doi: 10.1175/2010JAS3473.1.

Schmidli, J., 2013: Daytime Heat Transfer Processes over Mountainous Terrain. *Journal of the Atmospheric Sciences*, **70**, 4041–4066. doi: 10.1175/JAS-D-13-083.1.

Shaw, W. J., Berg, L. K., Cline, J., Draxl, C., Djalalova, I., Grimit, E. P., Lundquist, J. K., Marquis, M., McCaa, J., Olson, J. B., and Sivaraman, C., 2019: The Second Wind Forecast Improvement Project (WFIP 2): General Overview. *Bulletin of the American Meteorological Society,* **100**, 1687–1699.

Skamarock, W. C., et al., 2019: A Description of the Advanced Research WRF Version 4. NCAR Tech. Note NCAR/TN-556+STR.

Smagorinsky, J., 1963: General Circulation Experiments with the Primitive Equations: I. The Basic Experiment. *Monthly Weather Review*, **91**, 99–164. doi: 10.1175/1520-0493(1963)091<0099:GCEWTP>2.3.CO;2.

Stein, M., 1987: Large Sample Properties of Simulations using Latin Hypercube Sampling. *Technometrics* **29.2**, 143–151.

Svensson, G., A. A. M. Holtslag, V. Kumar, T. Mauritsen, G. J. Steeneveld, W. M. Angevine, E. Bazile, A. Beljaars, E. I. F. de Bruijn, A. Cheng, L. Conangla, J. Cuxart, M. Ek, M. J. Falk, F. Freedman, H. Kitagawa, V. E. Larson, A. Lock, J. Mailhot, V. Masson, S. Park, J. Pleim S. Söderberg, W. Weng, and M. Zampieri, 2011: Evaluation of the Diurnal Cycle in the Atmospheric Boundary Layer Over Land as Represented by a Variety of Single-Column Models: The Second GABLS Experiment. *Boundary-Layer Meteorology* **140**, 177–206.

Wagner, J. S., A. Gohm, and M. W. Rotach, 2014: The Impact of Horizontal Model Grid Resolution on the Boundary Layer Structure Over an Idealized Valley. *Monthly Weather Review*, **142**, 3446–3465. doi: 10.1175/MWR-D-14-00002.1.

Wyngaard, J. C., 2004: Toward Numerical Modeling in the "*Terra Incognita.*" *Journal of the Atmospheric Sciences*, **61**, 1816–1826. doi: 10.1175/1520-0469(2004)061<1816:TNMITT>2.0.CO;2.

Yang, B., Y. Qian, L. K. Berg, P.-L. Ma, S. Wharton, V. Bulaevskaya, H. Yan, Z. Hou, and W. Shaw 2017: Sensitivity of Turbine-Height Wind Speeds to Parameters in Planetary Boundary-Layer and Surface-Layer Schemes in the Weather Research and Forecasting Model. *Boundary-Layer Meteorology*, **162**, 117–142. doi: 10.1007/s10546-016-0185-2.

Yang, B., L. K. Berg, Y. Qian, C. Wang, Z. Hou, Y. Liu, H. H. Shin, S. Hong, and M. Pekour 2019: Parametric and Structural Sensitivities of Turbine-Height Wind Speeds in the Boundary-Layer Parameterizations in the Weather Research and Forecasting Model. *Journal of Geophysical Research: Atmospheres*, **124**, 5951–5969. doi: 10.1029/2018JD029691.

Appendix A – List of Project Publications

Journal Papers:

Allaerts, D., C. Draxl, E. Quon, and M. Churchfield, 2020: Large-Eddy Simulation of a Diurnal Cycle Driven by Assimilation of Mesoscale Time-Height Profiles, *Boundary-Layer Meteorology*, **176**, 329–348. doi: 10.1007/s10546-020-00538-5.

Abstract: Mesoscale-to-microscale coupling aims to address the limited scope of traditional large-eddy simulations by driving the microscale flow with information concerning large-scale weather patterns provided by mesoscale models. This paper presents a new offline mesoscale-to-microscale coupling technique for horizontally homogeneous microscale flow conditions in which adequate mesoscale internal source terms are computed based on mesoscale time-height profiles of mean flow quantities. The advantage of such an approach is that it does not rely on mesoscale budget components, which are not outputted by default by most mesoscale solvers, and that it could also be used to drive microscale simulations with observational data. The performance of the proposed profile assimilation technique is assessed based on the simulation of a quiescent diurnal cycle over the Scaled Wind Farm Technology Facility site in West Texas. Results indicate that simple data assimilation techniques lead to unphysically high levels of shear and turbulence caused by the algorithm's inability to cope with inaccuracies in the mesoscale time-height profiles. Modifying the algorithm to account for vertical coherence in the mesoscale internal source terms allows the microscale solver to take over and correct the provided mesoscale time-height profiles, leading to improved predictions of turbulence statistics in line with meteorological tower observations and simulation results obtained with standard internal forcing coupling techniques.

Arthur, R. S., J. D. Mirocha, and K. A. Lundquist, 2018: Using a Canopy Model Framework to Improve Large-Eddy Simulations of the Atmospheric Boundary Layer in the Weather Research and Forecasting Model, *Monthly Weather Review,* **147**(1), 31–52. doi: 10.1175/MWR-D-18-0204.1.

Abstract: A canopy model framework is implemented in the Weather Research and Forecasting model to improve the accuracy of large-eddy simulation (LES) of the atmospheric boundary layer (ABL). The model includes two options that depend on the scale of surface roughness elements. A resolved canopy model, typically used to model flow through vegetation canopies, is employed when roughness elements are resolved by the vertical LES grid. In the case of unresolved roughness, a modified "pseudo-canopy model" is developed to distribute drag over a shallow layer above the surface. Both canopy model options are validated against idealized test cases in neutral stability conditions and are shown to improve surface layer velocity profiles relative to simulations employing Monin-Obukhov similarity theory (MOST), which is commonly used as a surface boundary condition in ABL models. Use of the canopy model framework also leads to increased levels of resolved turbulence kinetic energy and turbulent stresses. Because LES of the ABL has a well-known difficulty recovering the expected logarithmic velocity profile (log-law) in the surface layer, particular focus is placed on using the pseudo-canopy model to alleviate this issue over a range of model configurations. Tests with varying surface roughness values, LES closures, and grid aspect ratios confirm that the pseudo-canopy model generally improves log-law agreement relative to simulations that employ a standard MOST boundary condition. The canopy model framework thus represents a low-cost, easy-to-implement method for improving LES of the ABL.

Draxl, C., D. Allaerts, E. Quon, and M. Churchfield, 2020: "Coupling Mesoscale Momentum and Temperature Budget Components to Large-Eddy Simulations for Wind Energy Applications," *Boundary-Layer Meteorology*, accepted.

Abstract: Wind plants are exposed to a variety of weather phenomena on many scales—from synoptic to mesoscale to microscale conditions. Mesoscale phenomena are described by mesoscale numerical weather prediction models and drive large horizontal variations on the microscale. Microscale turbulence and flow structures can be predicted by large-eddy simulation (LES) models and are important because their variability impacts the operating environment of wind plants. To simulate wind flow through a wind plant across a wide range of atmospheric conditions that drive wind plant performance, microscale models have to be coupled with mesoscale models, because microscale models lack atmospheric physical processes to represent local forcing.

Here, we couple mesoscale model output to a LES solver by applying mesoscale momentum and temperature budget components from the Weather Research and Forecasting model to the governing equations of Simulator fOr Wind Farm Applications (SOWFA). We test whether averaging the budget components impacts the LES simulations with regard to quantities of interest to wind energy. Results show that averaging reduces the spatiotemporal variability of the mesoscale momentum budget components; however, when coupled with LES, the mesoscale bias (in comparison with observations in wind speed, wind direction, and potential temperature) is not corrected by the LES simulation. On the contrary, LES can correct for shear and veer. In both cases, however, averaging the budget components showed no significant impact on mean flow quantities in the microscale and is not necessary when coupling mesoscale budget components to LES.

Haupt, S.E., B. Kosović, W. Shaw, L. Berg, M. Churchfield, J. Cline, C. Draxl, B. Ennis, E. Koo, R. Kotamarthi, L. Mazzaro, J. Mirocha, P. Moriarty, D. Muñoz-Esparza, E. Quon, R.K. Rai, M. Robinson, G. Sever, 2019: On Bridging a Modeling Scale Gap: Mesoscale to Microscale Coupling for Wind Energy, *Bulletin of the American Meteorological Society,* **100**(12), 2533–2550. doi: 10.1175/BAMS-D-18-0033.1.

Abstract: Accurately representing flow across the mesoscale to microscale is a persistent roadblock for completing realistic microscale simulations. The science challenges that must be addressed to coupling at these scales include: 1) What is necessary to capture the variability of the mesoscale flow, and how do we avoid generating spurious rolls within the *terra incognita* between the scales? 2) Which methods effectively couple the mesoscale to the microscale and capture the correct nonstationary features at the microscale? 3) What are the best methods to initialize turbulence at the microscale? 4) What is the best way to handle the surface layer parameterizations consistently at the mesoscale and the microscale? 5) How do we assess the impact of improvements in each of these aspects and quantify the uncertainty in the simulations?

The U.S. Department of Energy Mesoscale-to-Microscale-Coupling project seeks to develop, verify, and validate physical models and modeling techniques that bridge the most important atmospheric scales determining wind plant performance and reliability, which impacts many meteorological applications. The approach begins with choosing case days that are interesting for wind energy for which there are observational data for validation. The team has focused on modeling nonstationary conditions for both flat and complex terrain. This paper describes the

approaches taken to answer the science challenges, culminating in recommendations for best approaches for coupled modeling.

Mirocha, J.D., M.J. Churchfield, D. Munoz-Esparaza, R. Rai, Y. Feng, B. Kosović, S.E. Haupt, B. Brown, B.L. Ennis, C. Draxl, J.S. Rodrigo, W.J. Shaw, L.K. Berg, P. Moriarty, R. Linn, R.V. Kotamarthi, R. Balakrishnan, J. Cline, M. Robinson, and S. Ananthan, 2017: Large-Eddy Simulation Sensitivities to Variations of Configuration and Forcing Parameters in Canonical Boundary-Layer Flows for Wind Energy Applications, *Wind Energy Science,* **3**, 589–613. doi: 10.5194/wes-3-589-2018.

Abstract: The sensitivities of idealized large-eddy simulations (LES) to variations of model configuration and forcing parameters on quantities of interest to wind power applications are examined. Simulated wind speed, turbulent fluxes, spectra, and cospectra are assessed in relation to variations of two physical factors—geostrophic wind speed and surface roughness length—and several model configuration choices, including mesh size and grid aspect ratio, turbulence model, and numerical discretization schemes, in three different code bases. Two case studies representing nearly steady neutral and convective atmospheric boundary-layer (ABL) flow conditions over flat terrain, occurring at the Sandia Scaled Wind Farm Technology test facility, were used to force and assess idealized LES using periodic lateral boundary conditions. Comparison with fast-response velocity measurements at five heights within the lowest 50 m indicates that most model configurations performed similarly overall, with differences between observed and predicted wind speed generally smaller than measurement variability. Simulations of convective conditions produced turbulence quantities and spectra that matched the observations well, while those of neutral simulations produced good predictions of stress, but smaller than observed magnitudes of turbulence kinetic energy, likely due to tower wakes influencing the measurements during the neutral case. While sensitivities to model configuration choices and variability in forcing can be considerable, idealized LES are shown to reliably reproduce quantities of interest to wind energy applications within the lower ABL during quasi-ideal, nearly steady neutral and convective conditions.

Rai, R. K., Berg, L. K., Kosović, B., Haupt, S. E., Mirocha, J. D., Ennis, B. L., & Draxl, C., 2019: Evaluation of the Impact of Horizontal Grid Spacing in *Terra Incognita* on Coupled Mesoscale–Microscale Simulations Using the WRF Framework. *Monthly Weather Review*, **147**(3), 1007–1027. doi: 10.1175/MWR-D-18-0282.1.

Abstract: Coupled mesoscale-microscale simulations are required to provide time-varying weather-dependent inflow and forcing for large-eddy simulations under general flow conditions. Such coupling necessarily spans a wide range of spatial scales (i.e., ~10 m to ~10 km). Herein, we use simulations that involve multiple nested domains with horizontal grid spacings in the *terra incognita* (i.e., $\lesssim 1$ km) that may affect simulated conditions in both the outer and inner domains. We examine the impact on simulated wind speed and turbulence associated with forcing provided by a terrain with grid spacing in the *terra incognita*. We perform a suite of simulations that use combinations of varying horizontal grid spacings and turbulence parameterization/modeling using the Weather Research and Forecasting (WRF) model using a combination of planetary boundary layer (PBL) and large-eddy simulation subgrid-scale (LES-SGS) models. The results are analyzed in terms of spectral energy, turbulence kinetic energy, and proper orthogonal decomposition (POD) energy. The results show that the output from the microscale domain depends on the type of turbulence model (e.g., PBL or LES-SGS model) used for a given horizontal grid spacing but is independent of the horizontal grid spacing and

turbulence modeling of the parent domain. Simulation using a single domain produced less POD energy in the first few modes compared to a coupled simulation (one-way nesting) for similar horizontal grid spacing, which highlights that coupled simulations are required to accurately pass the mesoscale features into the microscale domain.

Rai, R.K., L.K. Berg, M. Pekour, W.J. Shaw, B. Kosović, J.D. Mirocha, B.L.Ennis, 2017: Spatio-Temporal Variability of Turbulence Kinetic Energy Budgets in the Convective Boundary Layer Over Both Simple and Complex Terrain. *Journal of Applied Meteorology and Climatology*, **56**(12), 3285–3302. doi: 10.1175/JAMC-D-17-0124.1.

Abstract: The assumption of subgrid-scale (SGS) horizontal homogeneity within a model grid cell, which forms the basis of SGS turbulence closures used by mesoscale models, becomes increasingly tenuous as grid spacing is reduced to a few kilometers or less, such as in many emerging high-resolution applications. Herein, we use the turbulence kinetic energy (TKE) budget equation to study the spatiotemporal variability in two types of terrain—complex (Columbia Basin Wind Energy Study [CBWES] site, northeastern Oregon) and flat (Scaled Wind Farm Technology [SWiFT] site, West Texas)—using the Weather Research and Forecasting (WRF) model. In each case, six-nested domains (three domains each for mesoscale and large-eddy simulation [LES]) are used to downscale the horizontal grid spacing from ~10 km to ~10 m using the WRF model framework. The model output was used to calculate the values of the TKE budget terms in vertical and horizontal planes as well as the averages of grid cells contained in the four quadrants (a quarter area) of the LES domain. The budget terms calculated along the planes and the mean profile of budget terms show larger spatial variability at CBWES site than at the SWiFT site. The contribution of the horizontal derivative of the shear production term to the total shear production was found to be ≈45% and ≈15% at the CBWES and SWiFT sites, respectively, indicating that the horizontal derivatives applied in the budget equation should not be ignored in mesoscale model parameterizations, especially for cases with complex terrain with < 10-km scale.

Rai, R.K., L.K. Berg, B. Kosović, J.D. Mirocha, M.S. Pekour, and W.J. Shaw, 2016: Comparison of Measured and Numerically Simulated Turbulence Statistics in a Convective Boundary Layer Over Complex Terrain. *Boundary-Layer Meteorology*, **163**, 69–98. doi: 10.1007/s10546-016-0217-y.

Abstract: The Weather Research and Forecasting (WRF) model can be used to simulate atmospheric processes ranging from quasi-global to tens of meters in scale. Here, we employ large-eddy simulations (LES) using the WRF model, with the LES domain nested within a mesoscale WRF model domain with grid spacing decreasing from 12.15 km (mesoscale) to 0.03 km (LES). We simulate real-world conditions in the convective planetary boundary layer over an area of complex terrain. The WRF-LES model results are evaluated against observations collected during the U.S. Department of Energy-supported Columbia Basin Wind Energy Study. Comparison of the first- and second-order moments, turbulence spectrum, and probability density function of wind speed shows good agreement between the simulations and observations. One key result is to demonstrate that a systematic methodology needs to be applied to select the grid spacing and refinement ratio used between domains to avoid having a grid resolution that falls in the grey zone and to minimize artefacts in the WRF-LES model solutions. Furthermore, the WRF-LES model variables show large variability in space and time caused by the complex topography in the LES domain. Analyses of WRF-LES model results

show that the flow structures, such as roll vortices and convective cells, vary depending on both the location and time of day as well as the distance from the inflow boundaries.

Simon, J. S., B. Zhou, J. D. Mirocha and F. K. Chow, 2019: Explicit Filtering and Reconstruction to Reduce Grid Dependence in Convective Boundary Layer Simulations Using WRF-LES, *Monthly Weather Review*, **147**(5), 1805–1821. doi: 10.1175/MWR-D-18-0205.1.

Abstract: As model grid resolutions move from the mesoscale to the microscale, turbulent structures represented in atmospheric boundary-layer simulations change dramatically. At intermediate resolutions, the so-called gray zone, turbulent motions are not resolved accurately, posing a challenge to numerical simulations. The representation of turbulence is also highly sensitive to the choice of closure model. Here, we examine explicit filtering and reconstruction in the gray zone as a technique to better represent atmospheric turbulence. The convective boundary layer is simulated using the Weather Research and Forecasting model with horizontal resolutions ranging from 25 m to 1 km. Four large-eddy simulation turbulence models are considered: the Smagorinsky model, the TKE-1.5 model, and two versions of the dynamic reconstruction model (DRM). The models are evaluated by their ability to produce consistent mean potential temperature profiles, heat and momentum fluxes, velocity fields, and turbulent kinetic energy spectra as the grids become coarser. The DRM, a mixed model that uses an explicit filtering and reconstruction technique to account for resolvable subfilter-scale stresses, performs very well at resolutions of 500 m and 1 km without any special tuning, whereas the Smagorinsky and TKE-1.5 models produce heavily grid-dependent results.

Conference Papers: (presenter in **Bold**)

Allaerts, D., C. Draxl, and M. Churchfield, 2018: “Large-Eddy Simulations of a Diurnal Cycle Driven by Mesoscale and Observational Profile Assimilation, American Physical Society Division of Fluid Dynamics Meeting,” Nov. 18-20, Atlanta, Georgia.

Allaerts, **D.,** C. Draxl, E. Quon, and M. Churchfield, “Evaluation of Internal Forcing Techniques for Mesoscale-to-Microscale Coupling,” 2019 Wind Energy Science Conference, June 16-20, Cork, Ireland.

Arthur, R.S., J.D. Mirocha, N. Marjanovic, B. D. Hirth, J. L. Schroeder, and **F. K. Chow**, 2019: Multi-Scale Simulations of Wind Farm Performance with Complex Terrain and Weather Events, NAWEA/WINDTECH, Amherst, MA, October 14–16.

Churchfield, **M.,** D. Allaerts, P. Hawbecker, and E. Quon, “Treatment of Gravity Waves in Wind Energy Atmospheric Large-Eddy Simulation,” June 16-20, 2019, Cork, Ireland.

Cline, J.W., **W. J. Shaw** and S.E. Haupt, 2018: Meteorology Research in DOE’s Atmosphere to Electrons (A2e) Program, Ninth Conference on Weather, Climate, and the New Energy Economy, AMS Annual Meeting, January 8.

Cline, J., S.E. Haupt, and W. Shaw, 2017: Meteorology Research in DOE’s Atmosphere to Electrons (A2e) Program, WindTech International Conference on Future Technologies in Wind Energy, Boulder, Co, October 24.

Connolly, A., W. H. M. Wendels, L. van Veen, L., J. M. T. Neher, B. Geurts, J. D, Mirocha, and F. K. Chow, 2020: Development of Fine Scale Structures in Large Eddy Simulations Over Complex Terrain, 19th Conference on Mountain Meteorology Virtual Meeting, 15 July.

Draxl, C., M. Churchfield, J. S. Rodrigo, 2017: Coupling the Mesoscale to the Microscale Using Momentum Budget Components, North American Wind Energy Symposium, Ames, USA, September 2017.

Draxl, C., M. Churchfield, J. S. Rodrigo, 2017: Coupling the Mesoscale to the Microscale Using Momentum Budget Components, AMS Annual Meeting, Seattle, USA, January.

Haupt, S.E., B. Kosović, L. Berg, W. Shaw, J. Mirocha, M. Churchfield, 2020: Mesoscale to Microscale Coupling for Wind Energy, 11th Conference on Weather, Climate, & the New Energy Economy, AMS Annual Meeting, Boston, MA, Jan. 14.

Haupt, S.E., L. Berg, M. Churchfield, B. Kosović, W. Shaw, J. Mirocha, 2019: Mesoscale to Microscale Coupling for Wind Energy Applications: Addressing the Challenges, *J. Physics Conference Series* (2020) 012076 **1452**, NAWEA/WindTech Conference, Amherst, MA, October 15, 2019. doi: 10.1088/1742-6596/1452/1/012076.

Haupt, S.E., 2019: Advances in Mesoscale to Microscale Coupling for Wind Energy Applications, 6th International Conference on Energy and Meteorology, Lyngby, Denmark, June 25.

Haupt, S.E., 2019: Mesoscale to Microscale Coupling for Wind Energy Applications, Energy Systems Integration Group Meteorology & Market Design for Grid Services Workshop, Denver, CO, June 5.

Haupt, S.E., B, Kosović, W. Shaw, L. Berg, R. Rai, J. Mirocha, M. Churchfield, C. Draxl, M. Robinson, 2018: Recent Advances in Mesoscale to Microscale Coupling, AMS Conference on Boundary Layers and Turbulence, Oklahoma City, OK, June 14.

Haupt, S.E., 2018: Progress in Mesoscale to Microscale Coupling: Modeling Nonstationary Conditions in Flat and Complex Terrain, International Conference on Energy & Meteorology, Shanghai, China, May 22, 40 min. lecture.

Haupt, S.E., 2018: Meteorology, Climate, and the Electric Sector – Forecasting for an Integrated Energy System, ESIG Forecasting Workshop, St. Paul, MN, June 19 (Invited Panel talk).

Haupt, S.E., L. Berg, M. Churchfield, J. Cline, J. Mirocha, B. Kosović, C. Draxl, R. Rai, R. Kostmarthi, M. Robinson, W. Shaw, 2017: The US DOE A2e Mesoscale to Microscale Coupling Project: Nonstationary Modeling Techniques and Assessment, International Conference on Energy and Meteorology, Bari, Italy, June 28.

Haupt, S.E., **J. Cline**, W. Shaw, L. Berg, M. Churchfield, J. Mirocha, B. Kosović, C. Draxl, R. Rai, R. Kotamarthi, 2017: The US DOE A2e Mesoscale to Microscale Coupling Project: Nonstationary Modeling Techniques and Assessment, European Geophysical Union, Vienna, Austria, April 26.

Haupt, S.E., W. Shaw, B. Kosović, 2016: The DOE A2e Mesoscale to Microscale Coupling Project, AMS Symposium on Boundary Layers and Turbulence, Salt Lake City, UT, June 20.

Haupt, S.E., 2016: Meteorology Models Enabling Wind Energy, Wyoming Renewable Energy Summit, Laramie, WY, June 13. Invited Keynote.

Haupt, S.E., W. Shaw, and B. Kosović, 2015: Meso-to-Microscale Coupling Project, WindTech Workshop, London, Ontario, Canada, October 19.

Hawbecker, P., and M. Churchfield, 2019: Mesoscale to Microscale Coupling for a Wind Ramp Case over Complex Terrain, 99th American Meteorological Society Annual Meeting, Phoenix, AZ. January 8.

Juliano, T.W., P. Jimenez, D. Muñoz-Esparza, B. Kosović, and S.E. Haupt, 2020: Wind Energy Forecasting Using a Three-Dimensional Planetary Boundary Layer Parameterization. 100th American Meteorological Society Annual Meeting, Jan. 14.

Kosović, B., T.C. McCandless, D.J. Gagne, T. Brumett, and S.E. Haupt, 2020: Machine Learning Models for Replacing Monin Obukhov Similarity Theroy Based Surface Layer Parameterization, 100th American Meteorological Society Annual Meeting, Jan. 14.

Kosović, B., P. Jimenez, **T. W. Juliano**, A. Martilli, M. Eghdami, A.P. Barros, and S.E. Haupt, 2019: Three-Dimensional Planetary Boundary Layer Parameterization for High-Resolution Mesoscale Simulations, *Journal of Physics Conference Series* (2020) **1452** 012080, NAWEA/WindTech Conference, Amherst, MA. doi: 10.1088/1742-6596/1452/1/012080.

Kosović, B., J. D. Mirocha, M. J. Churchfield, D. Muñoz-Esparza, R.K. Rai, Y. Feng, S.E. Haupt, B. Brown, B.L. Ennis, C. Draxl, J..Sanz Rodrigo, W. J. Shaw, L.K. Berg, P. Moriarty, R. Linn, R. V. Kotamarthi, 2017: Assessment of Large-eddy Simulations of the Atmospheric Boundary Layer for Wind Energy Applications, WindTech International Conference on Future Technologies in Wind Energy, Boulder, Co, October 25.

Kaul, C. M., S. Ananthan, M. J. Churchfield, J. D. Mirocha, L. K. Berg, R. Rai, 2019: Large-Eddy Simulations of Idealized Atmospheric Boundary Layers Using Nalu-Wind, NAWEA/WINDTECH, Amherst, MA, October 14–16.

Mirocha, J. D., S. E. Haupt, et al., 2019: Toward the Integration of Atmosphere and Wind Plant Physics and Simulation Techniques: An Overview of the DOE's Mesoscale-Microscale Coupling Project, Meteorology and Climate - Modeling for Air Quality Conference, UC Davis, Davis, CA, Sept. 11.

Mirocha, J. D. and S. E. Haupt, 2018: The U.S. DOE Mesoscale to Microscale Coupling Project: Extending Boundary Layer Flow Simulation to Complex Environments, Ninth Conference on Weather, Climate, and the New Energy Economy, AMS Annual Meeting, January 8.

Mirocha, J. D., R. K. Rai, M. J. Churchfield, Y. Feng, C. Draxl, J. Sanz Rodrigo, B. L. Ennis, B. Kosović , and S. E. Haupt, 2017: An Investigation of Online and Offline Mesoscale-Microscale Coupling Techniques During Unsteady Meteorological Conditions, WindTech International Conference on Future Technologies in Wind Energy, Boulder, Co, October 25.

Quon, E. W., A. S. Ghate, and S. K. Lele, 2018: Enrichment Methods for Inflow Turbulence Generation in the Atmospheric Boundary Layer. *Journal of Physics: Conference Series*, **1037**, 072054. doi: 10.1088/1742-6596/1037/7/072054.

Rai, R. K., L. K. Berg, B. Kosović, J.D. Mirocha, S.E. Haupt, B. L. Ennis, and C. Draxl, 2017: Evaluation of the Impact on Terra Incognita for Mesoscale and Microscale WRF Simulations, WindTech International Conference on Future Technologies in Wind Energy, Boulder, Co, October 25.

Rai, R. K., L. K. Berg, B. Kosović, J. D. Mirocha, M. Pekour, B. Ennis, and W. J. Shaw, 2017: Examination of the Spatio-temporal Variability of the Terms of the Turbulent Kinetic Energy Budget Over a Complex Terrain in the Convective Boundary Layer: A Tool for Parameterization Development, American Meteorological Society Meeting, Seattle, WA, January 24.

Rai, R., L. K. Berg, B. Kravitz, B. Kosović, J. D. Mirocha, B. Ennis, and S. E. Haupt, 2019: Improving Simulation of Turbulence in WRF-LES of Stable Condition Using Velocity Fluctuations, Tenth Conference on Weather, Climate, and the New Energy Economy, AMS Annual Meeting, Phoenix, AZ, Jan. 8.

Rai, R., L. K. Berg, C. Kaul, J. Mirocha, A. Choukulkar, W. A. Brewer, Y. Pichugina, R. Banta, 2019: Characterization of Turbulence Under Different Stability Conditions Using Lidar Scanning Data Near The WFIP 2 Physics Site, NAWEA/WINDTECH, Amherst, MA, October 14–16.

Sever, G., R.V. Kotamarthi, Y. Feng, 2017: A Turbulence Library for Asynchronous Coupling of Meso And Microscale Models, WindTech - International Conference on Future Technologies in Wind Energy, Boulder, CO, October 25.

Wise, A. J. M. T. Neher, R. S. Arthur, J. D. Mirocha, F. K. Chow, and J. K. Lundquist, 2020: Multi-Scale Modeling of a Wind Turbine Wake Over Complex Terrain in Different Atmospheric Stability Regimes, 19th Conference on Mountain Meteorology Virtual Meeting, 15 July.

Appendix B – Contributions of Individual Laboratories

Lawrence Livermore National Laboratory (LLNL): LLNL staff contributed to several components of the MMC project, including development of team source codes and analysis scripts, further examination of inflow perturbation methods, and execution of sensitivity studies of multiscale WRF simulations applied to a new offshore challenge case. The new source codes, which expand the ability to force WRF model simulations in idealized setups applicable to canonical boundary-layer flows, are available on the MMC GitHub for team and public use. The inflow perturbation analysis study completed the setup of a convective case—and developed potential stable and near-neutral cases, as well—with the intention of completing the analysis in all three stability classes during FY 2021 (see Section 8 for details). The LLNL team also worked with collaborators to execute a multiscale WRF simulation of a wind ramp passing through an operating wind plant, using actuator disk model for the turbines and inflow perturbations and published that work in *Atmosphere*. LLNL also contributed to the examination of multiscale WRF setups over complex terrain at the Perdigao field site, including simulation of stability and terrain impacts on flow and turbine wake characteristics, as well as efficacy of inflow perturbations relative to terrain resolution to instigate turbulence. The work was presented at the American Meteorological Society Mountain Meteorology conference, and journal manuscripts are under development, with planned submission in FY 2021. LLNL also contributed to the planning and execution of the industry workshop, which occurred in early FY 2021, as well as project reporting and integrated annual operating plan development. Finally, LLNL participated in planning future MMC project applications in both land-based and offshore settings, including the development of a coupled air-sea interaction framework for WRF-LES, investigation of low-level jet impacts in both offshore and land-based settings, and the use of ML to facilitate microscale turbulence generation and downscaling.

Los Alamos National Laboratory (LANL): During FY 2020, LANL continued to support the effort to assess various inflow perturbation methods used to accelerate turbulence development on turbulence-resolving microscale simulation domains forced by mesoscale inflow, as described in Section 5. As part of this effort, LANL team members Alex Jonko and Mukesh Kumar contributed WRF simulations using the momentum flavor of the cell perturbation method based on case study datasets for unstable atmospheric conditions provided by LLNL. This work will be continued in FY 2021 with the examination of turbulence generation under stable and neutral atmospheric conditions.

NCAR: NCAR continued to serve in a leadership role for the MMC project, which includes leading biweekly team telecons, representing the team at A2e meetings, presenting MMC research to DOE Office of Energy Efficiency and Renewable Energy Wind Energy Technologies Office leadership (March 3, 2020), and facilitating and publicizing the work. Dr. Haupt served as project principal investigator and contributed to the A2e uber principal investigator meetings as well as to overall project leadership, including work planning and tracking. NCAR hosted team workshops in Boulder in October 2019 and virtual workshops in April and December 2020. NCAR also led the planning and execution of an industry workshop that culminated in the Atmospheric Challenges for the Wind Energy Industry, held in October 2020, and reported on separately. That planning effort included leading monthly discussions with the industry advisory panel. Dr. Haupt was also responsible for summaries in quarterly reports and leading production of this FY 2020 annual report. The NCAR team members presented papers on MMC work at the North American Wind Energy Academy/WindTech conference in Amherst, Massachusetts, in October 2019, and at the Eleventh Conference on Weather, Climate, and the New Energy Economy held as part of the American Meteorological Society Annual Meeting in Boston, Massachusetts, in January 2020. Several other planned conference presentations were canceled or delayed due to the COVID-19 pandemic.

NCAR led the assessment planning and implementation. In FY 2020, that process was formalized (in collaboration with the National Renewable Energy Laboratory and the other laboratories) and new standardized processes were initiated. NCAR led the mesoscale modeling portion of the project in FY 2020, obtaining data from the FINO towers and doing first mesoscale simulations, including modifying the WRF model. NCAR also advanced the 3D PBL scheme that was initiated in the Wind Forecast Improvement Project 2. NCAR also began incorporating new ML models for the surface layer as part of the MMC project in FY 2020. NCAR is providing leadership in transitioning the MMC project to two separate projects: 1) continuation toward closeout of the land-based MMC project and 2) the Offshore Wind Atmospheric Coupling project.

National Renewable Energy Laboratory (NREL): NREL researchers contributed to the MMC project in various ways. Matt Churchfield serves as the NREL lab-level principal investigator of the project, and he coordinates the microscale efforts of the FINO1/Alpha Ventus offshore coupling comparisons. Dries Allaerts, a former NREL-postdoc, now a faculty member at TU-Delft, continues to coordinate the microscale efforts of the SWiFT diurnal cycle land-based coupling comparison. Eliot Quon is involved in the inflow perturbation study effort, bringing experience with synthetic turbulence generation methods, such as the Mann or Veers methods. Caroline Draxl and Regis Thedin have contributed greatly to the effort to use a stand-alone microscale solver to simulate mesoscale-forced flow over complex terrain in the Wind Forecast Improvement Project 2/Biglow Canyon region. Caroline Draxl, Regis Thedin, and Eliot Quon have further explored the concept of internal coupling and applied it to the land-based SWiFT diurnal cycle case (resulting in a *Boundary-Layer Meteorology* publication), the offshore FINO1/Alpha Ventus case, and the land-based Peetz Table Wind Energy Center, in conjunction with the A2e Wake Dynamics project. Regis Thedin has advanced our methods for gravity wave treatment in stand-alone microscale solvers. Eliot Quon has led an effort to use mesoscale-influenced microscale LES data to examine simulated wind turbine loads and how those compare to simulated loads that result from the use of International Electrotechnical Commission-standard turbulence models.

In addition to this science work, the NREL team actively took part in the in-person and virtual team workshops, the Atmospheric Challenges for the Wind Energy Industry Workshop, and the planning for work in FY 2021 and beyond, which includes the new Offshore Wind Atmospheric Coupling project starting in FY 2021. NREL also contributed to both the FY 2019 and FY 2020 year-end reports, and NREL's communications team performs the first round of editing on these documents. The NREL team published an article in *Boundary-Layer Meteorology* and worked toward having a second article published in FY 2021 in the same journal.

Pacific Northwest National Laboratory (PNNL): Staff at PNNL contributed to many facets of the MMC project focused on land-based wind applications, including the development and testing of coupling methods, the development and testing of perturbation methods, the development and application of a lidar simulator and the evaluation of turbulent flow structure using lidar data (see Section 3 of this report), and the uncertainty quantification of microscale simulations in complex terrain (see Section 8 of this report). PNNL team members were also engaged in work to expand the MMC project purview to modeling for offshore wind energy, including engaging with PNNL wave modeling experts to generate wave state data for coupling to atmospheric simulations and participating in offshore environment microscale modeling intercomparisons. This work will be continued under the new Offshore Wind Atmospheric Coupling project in FY 2021.

In FY 2020, the team presented MMC research at the North American Wind Energy Academy/WindTech conference in Amherst, Massachusetts, in October 2019, and at the Eleventh Conference on Weather, Climate, and the New Energy Economy held as part of the American Meteorological Society Annual Meeting in Boston, Massachusetts, in January 2020. The team also worked toward preparing peer-reviewed publications for submission in FY 2021.

Additionally, as the lead DOE national laboratory of the project, PNNL coordinated submission of the project's FY 2019 annual report as the FY 2020 Q1 joint deliverable, helped to coordinate quarterly reporting, and led efforts to develop FY 2021 annual operating plans.

Pacific Northwest National Laboratory

902 Battelle Boulevard
P.O. Box 999
Richland, WA 99354
1-888-375-PNNL (7665)

www.pnnl.gov